NATURAL STIMULI FOR MICE: ENVIRONMENT STATISTICS AND BEHAVIORAL RESPONSES

MAGDALENA KAUTZKY

Graduate School of
Systemic Neurosciences
LMU Munich

Dissertation der Graduate School of Systemic Neurosciences der Ludwig-Maximilians-Universität München

March 2023

Magdalena Kautzky: *Natural stimuli for mice: environment statistics and behavioral responses*

1st Supervisor: Prof. Dr. Laura Busse
Division of Neurobiology
Faculty of Biology
Ludwig-Maximilians-Universität München

2nd Supervisor: Prof. Dr. Thomas Euler
Werner Reichardt Centre for Integrative Neuroscience (CIN)
Institute for Ophthalmic Research
Eberhard Karls University of Tübingen

1st reviewer: Prof. Dr. Laura Busse
2nd reviewer: Dr. Jens Kremkow
Date of Submission: December 5, 2022
Date of defense: February 28, 2023

ABSTRACT

A mouse's natural visual environment is dynamic, complex and poses several challenges for the animal. To ensure survival in the specific habitat of a mouse, their visual system has evolved to efficiently represent relevant features of the surroundings. The mouse exhibits several prominent adaptations of it's visual system. A wide field of view of around 180° per eye makes it possible to monitor the visual scene, including over head space (Seabrook et al., 2017). Additionally, the two opsin types, present in the mouse's retina, are distributed non-uniformly. The M-opsin, which is green sensitive, is predominately represented in the dorsal retina and the S-opsin, being UV sensitive, contributes to a strong UV-sensitive ventral retina (Baden et al., 2013).
In the first part of my thesis, we investigated these adaptions in context of the mouse's visual habitat. We constructed a UV- and green-sensitive camera and recorded 'mouse view' movies in potential mouse habitats (Qiu et al., 2021). Statistical analysis of those scenes revealed an overall dark contrast bias and richer chromatic contrast in the visual field above the horizon. In addition, the convolutional autoencoder model trained with sections of naturalistic movies of the upper, but not lower, visual field learned color-opponent filters. Further, we could show, that during twilight conditions, contrast is much higher in the UV channel than in the green channel, probably supporting detection of predators against the sky.
Mice actively interact with their environment, for example by moving theirs eyes, which changes how the visual scene is perceived. In the second part of this thesis, we want to shed light on how mice move their eyes to navigate their visual world (Meyer et al., 2020, discussed in Kautzky and Busse, 2020). Meyer et al. (2020) could show that eye movements in freely moving mice are tightly coupled to head movements. They found two distinct patterns of eye-head motion. The first one serves to shift the gaze within the horizontal plane. It closely resembles an evolutionary conserved pattern of fast gaze shifts and stabilization phases in between, called 'saccade and fixate pattern'. To stabilize the image on the retina during head movements, the second eye motion pattern functions to compensate head movements

relative to the ground.
Towards the goal of deepening our understanding of eye movements in mice, the third part of the thesis focuses on eye motion of head fixed mice viewing naturalistic movies. We presented movies in an ecologically relevant manner in a hemispheric dome setup to cover their visual field and in appropriate chromatic channels, UV and green (Kautzky et al., 2022). Visual stimuli were projected onto the surface of the dome via a spherical mirror, which introduces spatial distortions (Bourke, 2005). Thus, we developed a calibration routine, which is fast and precise, without assumptions about the specific geometry of optical parts in the light path. Viewing naturalistic movies, mice did not saccade to specific features in the visual scene. Comparing pupil position during natural scene stimulation and uniform screen control, we found a systematic shift towards more nasal and ventral regions (Kautzky et al., 2022). This suggests, that mice adjust their eye position based on visual input, probably to improve processing of visual information of the region of visual space in front of them.
Together, we have developed methods for acquisition and replay of naturalistic stimuli for mice, which consider several specializations of the early visual system of the mouse. And we showed that mice systematically change their eye position in context with naturalistic stimulation.

CONTENTS

1

INTRODUCTION

1.1 ORGANIZATION OF THE EARLY VISUAL SYSTEM OF MICE

Sensory systems of different species evolutionary developed to serve increasing chances for survival and procreation in the specific niche this species occupies. In the visual system the information that light of the surroundings carries is processed by a multitude of neuronal structures in the mammalian brain, and even within mammals the early visual system exhibits a large amount of different specializations. In this thesis, I will focus on mice and their natural visual scene. To lay a foundation for better understanding of the mouse's specialized visual system, I will describe more generally the early visual system of mammals, pointing out certain interesting facts about the mouse early visual pathways.
First, I will first define an important underlying concept for visual processing - the "receptive field" (RF). It is present in all processing stages of visual information, from photoreceptor to higher areas of visual cortex. Each neuron is activated by light from only a restricted region in the visual field around an animal, the RF. Properties of the information contained in this region, like direction of movement, orientation or contrast, can further define the RF of a neuron.

1.1.1 *The retina*

Visual information of the environment around us is projected as a two-dimensional, upside-down image through the optic apparatus of the eye, the cornea and lens, onto the retina. The vertebrate retina is layered and contains

seven major cell types, six types of neurons (ganglion cells, amacrines, bipolars, horizontal cells, and rod and cone photoreceptors) and the Müller glia cells, providing structure and supporting homeostasis (Cepko et al., 1996; Stenkamp, 2015). Here, processing of visual information begins with phototransduction by rod and cone photoreceptors, converting incoming photons to electrical signals. Rods make up for approximately 97 % of photoreceptors in the mouse retina (Fu & Yau, 2007) and 95 % in the human retina (Curcio et al., 1987).

Rods are specialized for low-light vision and can even detect single photons with their photopigment, rhodopsin (Baylor et al., 1979). But rods respond rather slowly and have low spatial acuity and contrast sensitivity (Fu & Yau, 2007).

Cones on the other hand are specialized for day-time and color vision and have high spatial acuity and contrast sensitivity, also they react around 20 ms faster than rods to incoming light (Cao et al., 2007). Cones express different opsins, sensitive to short wavelengths (S-opsin), medium wavelengths (M-opsin) or long wavelengths (L-opsin), allowing for color vision. These opsins can have slightly different peak absorption wavelength for different species (Peichl, 2005). Most mammals are dichromatic, enabling discrimination of shorter wavelengths from longer wavelengths, except for some primates and humans, where three opsins can be found in the retina (Peichl, 2005). In humans, the absorption spectra of the three opsins peak at 430 nm (blue, S-opsin), the 530 nm (green, M-opsin) and 560 nm (red, L-opsin) (Merbs & Nathans, 1992). Mice and other rodents can see two colors, UV (S-opsin) and green (M-opsin), the peak sensitivity of these opsins being 360 and 508 nm, respectively.

Generally, diurnal mammals commonly have higher cone densities than nocturnal ones, since cones are less sensitive in low light conditions (Peichl, 2005). Accordingly, the average density of rods in the mouse retina is higher than in the primate's retina, interestingly the cone density is comparable to the primate's retina. But due to the small size of the mouse's eye (radius of 1.6 mm; Sakatani and Isa, 2004), less photoreceptors sample a given portion of the field of view, adding to mice' poor acuity (approximately 0.5 cycles/degree; Jeon et al., 1998; Prusky and Douglas, 2003).

Both opsins can be co-expressed by one cone type (M-cone) in the mouse retina. Coexpression of the S-opsin is most prominent in the central retina. A cone type exclusively expressing S-opsin (S-cones) constitutes only about 4 % of all cones and is equally spaced over the retina. Exclusively M-opsin expressing cones constitute more than 90 % of cones in the dorsal retina

and only around 20 % in the ventral area (Baden et al., 2013). This gradient renders the dorsal retina mostly green sensitive and the ventral retina UV sensitive. Besides the spectral tuning of cones, they are also often tuned to achromatic contrast. S-cones in the ventral retina, looking up into the sky region of the visual field, have a strong dark-contrast bias (Baden et al., 2013).
Some mammals have a specialization that enables high acuity, high contrast vision; a region of the retina with a higher density of cones (visual acuity of 30–64 cycles/degree, Veilleux and Kirk, 2014). Several primate species exhibit such a spot on the retina, called the fovea, the cone density in the fovea increases significantly compared to the surroundings (Bringmann et al., 2018), but it spans less than 1 % of the area of the retina (Hendrickson, 2005). Also other species like cats, some reptiles and birds have an area of higher cone density (Hauzman et al., 2018). Mice lack a fovea or anything similar on the level of the retina, even though photoreceptor density is also slightly higher in the center (Jeon et al., 1998). Another interesting irregularity in the mouse retina is the change in RF size and density in so called *alpha*-retinal ganglion cells (RGCs), which are more prominent in the temporal retina, where they also exhibit smaller RFs (Bleckert et al., 2014). This leads to enhanced sampling of visual space roughly in the frontal visual field of the animal. Additionally, a recent study could show that a specific mechanism of enhancing spatial resolution exists in primary visual cortex, which I will point out in 1.1.3.
But not only density of photoreceptors determine how good a specie's eye sight is. The last layer of the retina is dominated by RGCs which project information about the visual environment to several brain regions. RGCs receive photoreceptor signals, filtered from three classes of retinal interneurons: amacrine, bipolar and horizontal cells. One RGC usually sums up input from several cones, which decreases spatial resolution of the visual system. The only known exception is the primate fovea, where 1:1 connection between cones and ganglion cells exist (Peichl, 2005). RGC density in primate retina is highest in the foveal region, enhancing spatial resolution (Curcio & Allen, 1990). The distribution of RGCs in the mouse retina is only slightly non-uniform, a higher density is found in temporal parts of the retina, which covers the contralateral visual field, and the lowest density in the dorsal retina (Dräger & Olsen, 1981).
In the mouse retina, around 40 functionally different types of RGCs have been found (Baden et al., 2016), whereas so far there are only 18 RGC types known in the primate retina, and 23 in the cat retina (Kim et al., 2021). Some

exemplary RGC types present in the mouse retina are direction-selective, orientation-selective (Barlow & Hill, 1963) or sensitive to specific edges (Cleland & Levick, 1974). Also, there are RGCs which respond to a RF divided into an outer and inner region, "center-surround" RFs (Sanes & Masland, 2015). ON-center RGCs, for example, respond best to a bright stimulus in the center region and a low luminance stimulus in the OFF surround. "Suppressed-by-Contrast" RGCs respond to contrast between the outer and the inner area or, more specifically, are suppressed by either a dark or a bright contrast (Sanes & Masland, 2015). Another interesting type, found in several mammalian species, is the intrinsically photosensitive RGCs (ipRGCs), expressing melanopsin, a photosensitive pigment with spectral sensitivity peaking in the blue range (Do & Yau, 2010; Keeler, 1928; Lockley et al., 2003; Zaidi et al., 2007). These RGCs contribute to the pupillary light reflex, controlling the amount of light hitting the retina, by constricting or dilating the pupil.

Color vision starts within the retina, even at the very first synapse of the visual system. Cones of different spectral sensitivity are controlled by each other via horizontal cells. Also on the RGC level, color opponency can be found, if two spectrally defined bipolar cells connect to the same RGC, one inhibitory, one excitatory (Baden & Osorio, 2019; Mills et al., 2014). The spectral division of the retina seems to be hindering color discrimination in mice. But a behavioral study showed that mice are indeed able to distinguish UV from green, however only in the upper visual field, which is likely monitored with the UV sensitive ventral retina (Denman et al., 2018). One theory of how mice can discriminate color on the level of the retina, involves rod photoreceptors, which are sensitive to a chromatic spectrum matching the mouse's M-opsin. A specific RGC type, the JAM-B-RGC, is mainly present in the ventral retina and, via horizontal cells, connected to rod output. The J-RGCs respond strongly to rod input in their surround RF and to S-cone input in the center (Joesch & Meister, 2016). This phenomenon has also been shown at the photoreceptor level, where the one type of horizontal cells mice have, connect rods and cones and create a inhibitory, green-sensitive surround response of S-cones in the ventral mouse retina (Szatko et al., 2020).

After extensive processing on the retinal stage, RGC axons transmit the output to more than 50 areas in the brain (Martersteck et al., 2017). Most RGC projection cross over to the contralateral hemisphere at the optic chiasm (Seabrook et al., 2017).

1.1.2 *Subcortical targets of visual information from the retina*

The superior colliculus (SC) is a sensorimotor midbrain structure, which receives input from several sensory modalities, especially also the primary visual cortex (see next section 1.1.3). In the mouse it receives input from 85-90 % of all RGCs and mediates defensive behaviors, such as alertness, freezing or escape (Almada et al., 2018; Ellis et al., 2016), and also plays a role in prey capture (Hoy et al., 2019). In primates the SC receives input from only 10 % of RGCs (Perry & Cowey, 1984) and is involved in e.g. spatial attention and visual target selection (Seabrook et al., 2017).
The dorsal lateral geniculate nucleus (dLGN) is the main connection between retina and visual cortex (Cruz-Martín et al., 2014). 30 % to 40 % of RGCs of the mouse's retina project to the dLGN (Ellis et al., 2016), in contrast, 90 % of RGC axons in the primate terminate in dLGN (Perry & Cowey, 1984). The dLGN is organized in a retinotopic way, reflecting a topographic representation of the retinal RF organization, equivalent to visual space. Several RGCs can converge on one dLGN neuron (Hammer et al., 2015). Half of the neurons in the mouse dLGN have center-surround RF structure, others are orientation- or direction-selective (Piscopo et al., 2013). Interestingly, even though around 40 % of all dLGN neurons receive input from the ipsilateral eye, mainly in the binocular zone, dLGN is mainly dominated by contralateral information (Rompani et al., 2017). The reason that these connections do not seem to have a functional purpose can be explained on synaptic level, where ispilateral input is weaker (Bauer et al., 2021).

1.1.3 *The primary visual cortex*

The next processing stage of visual information is the primary visual cortex (V1), which is a six-layered structure in neocortex. As the dLGN, also V1 is retinotopically organized. It receives its main input from the dLGN. In cats and primates, dLGN mostly projects to layer 4, and to a smaller portion to layer 6. In contrast, all layers of mouse V1 receive direct dLGN input, but strongest connection still occur in layer 4 (Ji et al., 2015). In primates, the size of RFs in V1 is smallest at the retinotopical location of the fovea, ensuring high acuity (Hubel & Wiesel, 1974). A new study in mice has shown a

similar effect for a certain region of the mouse's visual field, which they called the '*focea*' (van Beest et al., 2021). More precisely, the population RFs are smaller in an area of V1 that corresponds to the visual field 0° azimuth, i.e., directly in front of the mouse and 20° elevation, i.e. slightly above the mouse's head (van Beest et al., 2021). Many V1 neurons in cats or primates can be stimulated by showing a stimulus to either eye, they have binocular RFs (Hubel & Wiesel, 1962; 1969). The mouse V1 can be broadly separated into two regions depending on eye-specific inputs from one or both eyes. First, a larger monocular area where exclusively contralateral information is processed, and secondly, a binocular area, which processes information from both eyes (Kalatsky & Stryker, 2003).

1.1.4 *Binocular vision*

All vertebrates and also most invertebrates watch their visual environment through two eyes, which is costly for the organism, but the advantages seem to prevail (Pettigrew et al., 1986). For example, two eyes improve signal-to-noise ratio under unfavorable lighting conditions, or provide the ability to see 'around' occlusions in the visual field. Another important advantage is the possibility to create a 3D view of the surroundings from the 2D images on the retina. This can be achieved by using the deviations between the two retinal images, which represent different regions in space, depending on the position of the eyes relative to each other. Some neurons in mouse V1 are tuned to these deviations, which are called binocular disparities (La Chioma et al., 2019), and mice are more sensitive to contrast when presented binocularly (Speed et al., 2019). These binocular disparities can be used to triangulate distance of objects from the observer, and also generate a three dimensional perception of depth, also referred to as stereopsis (Nityananda & Read, 2017). Binocular vision is enabled by RGC axons projecting to the ipsilateral hemisphere, these projections contribute only 5 % to 10 % of all RGC projections in mice, in primates, on the other hand, around 45% do not decussate (Coleman et al., 2009; Erskine & Herrera, 2014). For primates, RGCs located in the temporal area of the retina commonly project ipsilaterally, whereas in mice, RGC axons that do not cross the chiasm, arise in ventro-temporal retina (Coleman et al., 2009; Dräger & Olsen, 1980; Johnson et al., 2021; Sterratt et al., 2013).

1.1.5 *Modelling the visual system*

Computational models have become a large part of neuroscience for different purposes; e.g. they can be used to investigate causal relations between behavior and different properties of neurons or population activity. They can predict neuronal patterns or so called 'neural code', as response to a certain stimulus, which can help specify a hypothesis about the underlying mechanisms in the brain (Carandini et al., 2005).
One promising technique of modelling computations in the early visual system is the efficient coding approach, which is an unsupervised modelling method. The efficient coding theory in neuroscience postulates that sensory circuits encode maximal information about their environment under constraints, like metabolic costs or noise (Barlow & Rosenblith, 1961; Field, 1994; Laughlin, 1981). The visual environment, to which the corresponding visual system is adapted, is analyzed by a model, which derives a neural code, efficiently representing the stimulus. These models have produced feature representations in different stages of the visual system, that are plausible in a biological context (Barlow & Rosenblith, 1961; Roy et al., 2021; Simoncelli & Olshausen, 2001).
An example for efficient coding is sparse coding, which is based on the idea that a neuronal population encodes various stimulus features efficiently by activation of the smallest possible set of neurons (Zylberberg & DeWeese, 2013). To achieve sparseness in a model, it learns an over-complete basis function, with sparse activation to recover the input stimuli, for example natural images (Olshausen & Field, 1996). These models generate localized and oriented filters, that can resemble RFs of neurons along the early visual pathway (Hubel & Wiesel, 1959).
In convolutional neural networks, several hidden layers connect input and output layers, imitating neurons, that are connected via several synapses to the next layer of neurons (Fukushima & Miyake, 1982; Lindsey et al., 2019). One example is a convolutional autoencoder, which is trained, in an unsupervised manner, to first encode the input, e.g. a natural scene image, to a lower dimensional representation and then decode this representation 'back' to the original stimulus (Kramer, 1991). The compressed representation is forced by an imposed bottleneck, which e.g. resembles the principles of the optic nerve as a stringent bottleneck, with a low transmission capacity relative to the high number of RGCs (Zhaoping, 2006). This type of model employs one or more layers of convolutional filters in the encoder network,

which can be again regulated by resource constraints (Doi & Lewicki, 2007; Vincent & Baddeley, 2003). There can be enforcement of smooth filters or an activation constraint for activation within a layer, which resembles sparse activation (Qiu et al., 2021; Shi et al., 2019; van Rossum et al., 2003). With these regularizations, a convolutional autoencoder can produce antagonistic center-surround filters like RF properties along the early visual system (Ocko et al., 2018; Qiu et al., 2021).
Even though efficient coding approaches can result in feature selectivity that is very similar to biological RFs, it is challenging to test, whether biological systems employ the model-derived strategy (Eichhorn et al., 2009; Paiton et al., 2020).

1.2 NATURAL VISUAL ENVIRONMENT AND BEHAVIOR OF MICE

Mice have an impressive ability to adapt to almost any environment on earth. Some mouse species live in 2000 m altitudes, in 50° deserts or extremely cold areas. But the mouse (*Mus musculus*) with highest genetic similarity to the laboratory mouse strain, usually lives close to humans and their natural environment comprises forests, meadows, steppe and cities (Phifer-Rixey & Nachman, 2015).
Mice observe their visual world with eyes that are placed laterally within their skull, with an azimuth angle of 60° and pointed upwards with an elevation of 30° (Sakatani and Isa, 2007; alternative model: azimuth: 64°, elevation: 30° from Oommen and Stahl (2008)). When mice freely roam in their habitat, they keep their head at a negative pitch of 29° (Oommen & Stahl, 2008; Stabio et al., 2018). The visual field of one eye spans 180° and there is a small overlap of the fields of both eyes, the binocular zone, of around 40° (Michaiel et al., 2020; Seabrook et al., 2017). Resulting in a total visual field of around 320° covering a large fraction around the animal (Seabrook et al., 2017).
With mice living on the ground and their eyes slightly pointing up, the vertical center of their visual scene is approximately the horizon, which divides the visual field into upper and lower visual field (Sterratt et al., 2013). Whereas the upper visual field usually shows the sky, high shrubs and trees, and the lower visual field features gravel, grass and undergrowth. Considering the chromatic specialization of the retina, mice survey the

ground with their mainly green-sensitive dorsal retina. In the lower area of the visual field, they need to forage for food and interact socially with other mice. The sky region is monitored by the ventral retina, which is UV sensitive and biased to dark contrast detection (Baden et al., 2013). As small mammals that are mostly considered prey animals, most predators will attack from above, especially since a considerable fraction of animals preying on mice are birds, e.g. owls and hawks (Dickman et al., 1991; Graf, 1947). Mice exhibit innate freezing or escape behaviors, when confronted with dark objects overhead (Yilmaz & Meister, 2013). More precisely, a common stimulus used in lab environment is the looming stimuli, meaning a dark object on a brighter background, which represents dark contrast, that is either moving or expanding above the animal. When the same stimulus is shown below the mouse, or the contrast is inverted, bright object on dark background, mice do not show these defensive behaviors as frequently or as quickly (Yilmaz & Meister, 2013).
But mice are not only prey animals, they are successful predators themselves, hunting many different types of small insects (Seabrook et al., 2017). Prey capture includes a series of different complex actions, such as prey detection, approaching the prey, orienting to pursuit and initiation of capture, which are based on vision, as Hoy et al. (2016) could show. They let mice capture crickets under different conditions, impairing either their visual or auditory sense. In the dark, mice performed very poorly, whereas ear-plugging them, changed almost nothing in their preying behavior. Combining these two manipulations, earplugs and darkness, made it even harder for mice hunt. This shows that mice use auditory cues to hunt, if available, but mainly rely on their eyes to catch their prey. Another factor that seems crucial for preying success is binocular vision. The mouse's binocular field extents in front and above the animal (Wallace et al., 2013) and it has been shown that they try to keep the prey within in this binocular zone (Hoy et al., 2016; Michaiel et al., 2020).

1.3 EYE MOVEMENTS IN MICE

Why do we move our eyes? This is a question Gordon L. Walls posed 60 years ago and as a human, the answer seems obvious - to change our line of sight to some object in our peripheral vision that we want to look at (Walls,

1962). But that is just the smaller part of the function of eye movements and only holds true for animals with high acuity vision, supported by a fovea (in the case of primates) or similar anatomical specializations, like cats, some birds or snakes (Land, 2015). Many animals do not look at objects the way we do, and in general, looking at different parts of the visual surroundings, head movements would suffice, since eyes are fixed in the head and would move with it. Of course for humans and most primates, the large head has a lot more inertia than eyes, controlling this is more difficult than for animals with smaller heads (Land, 2019). The barn owl is an extreme example of strongly visual driven animal with eyes that are barely movable (Harmening & Wagner, 2011). A mammalian example of shifting gaze within the visual field with mainly head movements is the rabbit (Collewijn, 1977).
This shows that eye movements did not only develop for shifting gaze. The actual problem becomes apparent, if one follows a moving object in front of a stationary background. The object will be in focus, but the background will be blurred to a point where objects cannot be recognized. This is due to long response latencies of photoreceptors, cones need 15 - 20 ms to reach peak response levels after a change in light intensity (Friedburg et al., 2004). When the scene changes before this time has passed or an object moves too fast, motion blur will occur. Motion blur or smear is well known for digital cameras with photoelectric detector surfaces consisting of an array of small sensors. The signal is accumulated over time and movement will cause the same image information to be distributed across several detectors, resulting in blur (Bedell et al., 2010).
Since animals have to move fast sometimes, there is no real solution for this problem. But a coping mechanism is to reduce the overall duration during which image blur occurs, which was already present in fish species 450 million years ago (Land, 2019).
This coping mechanism is based on information from direction selective RGCs (Yonehara et al., 2009) - the optokinetic reflex (OKR) (Katoh et al., 1998). The direction and velocity information of the visual scene is derived by RGCs and sent to the extraocular muscles. It serves to stabilize a drifting scene on the retina by eliciting steady eye movements in the same direction and with the same velocity as the scene. The drifting eye motion is frequently interrupted by fast recentering eye movements in the opposite direction to again follow the scene (Cahill & Nathans, 2008).
A second compensatory mechanism for image stabilization during self-motion works complementary to the OKR, the vestibular okular reflex (VOR). This reflex can also be elicited in the dark, during complete absence

of visual stimulation (Oommen & Stahl, 2008). It is based on information from the vestibular system consisting of the otholit organs and three semicircular canals (Khan & Chang, 2013).
The semicircular canals are located in the inner ear, oriented around the pitch, tilt and yaw axis of the head and filled with fluid called endolymph. The fluid starts moving with angular or rotational acceleration of the head in each direction, but only with a certain lag due to inertia. This discrepancy between head and fluid applies a force to a gelatinous structure, the cupula, at the bottom of each canal, containing cilia that are connected to motion sensors, hair cells, embedded in a neuroepithelium, the crista ampullaris (Khan & Chang, 2013). Linear acceleration or gravitational forces are detected by the otholit organs, the utricle and the saccule. The sensory neuroepithelium, called macula, of the saccule detects vertical movement, whereas the macula of the utricle senses movement in the horizontal plane. The macula contains hair cells, similar to the crista ampullaris, but with finer cilia, which can be deflected by gravitation (Morsli et al., 1998). The hair cells of both vestibular structures, semicircular canals and otholith organs, signal direction and strength of head velocities via the vestibulocochlear nerve to the vestibular nuclei in the brainstem and to the cerebellum. From there, information travels to the extraocular motor nuclei, which signal extraocular muscles to move the eye contrary to the direction of the head, to compensate for the head movement (Khan & Chang, 2013). The VOR is divided into angular (semicircular canals) VOR or translational (otholit organs) VOR components. It ensures a stable image on the retina, even if the animal's head is moving relative to the body or relative to space during locomotion (Iwashita et al., 2001).
In freely roaming mice, many eye movements can be explained by head movements relative to the horizontal plane, called head tilt (Meyer et al., 2020, discussed in Manuscript 2 - Kautzky and Busse, 2020). Head tilt comprises pitch of the head, the nose pointed up or down, and head roll, rotation along the anterior posterior axis. Most of these compensatory eye movements are non-conjugate, which means the eyes move in opposite directions. For example, if a mouse rolls it's head to the right, the right eye will move up and the left eye down (Oommen & Stahl, 2008). This coupling of head and eye movement aligns the visual scene relative to the ground, which could provide a stabilization of the horizon (Meyer et al., 2018; Oommen & Stahl, 2008). This clear separation into upper and lower visual field might be advantageous, considering the chromatic division of the retina in green sensitive ventral and UV sensitive dorsal retina (Baden

et al., 2013).
If these two reflexes work properly and the mouse would make a turn around the yaw axis, the eyes would get stuck and hit the limits of their mobility. In this case the gaze is shifted to a new position in the surroundings by yet another reflex. More precisely a special case of the VOR, the horizontal angular VOR (Khan et al., 2019; Migliaccio et al., 2010; van Alphen et al., 2001), which is again led by head motion and the eyes follow. A head rotation around the yaw axis is initiated, which triggers the eyes to counter rotate, as expected from the VOR. But after a short period of time, around 100–200 ms, the VOR is suspended and both eyes make a horizontal, fast and conjugate movement in head direction, a saccadic eye movement, to then counter rotate again, driven by the recommenced VOR, to the position where the head stops (Meyer et al., 2020; Michaiel et al., 2020). In total, the combined pattern of head and eye motions shifts the line of sight of a mouse around 23°, whereas a saccadic, non-compensatory eye movement only shifts gaze around 9° and a horizontal head movement around 16° (Meyer et al., 2020).
Overall the horizontal gaze pattern of freely moving mice consists of fast shifts of direction ('saccades'), interspersed with longer faces of stabilization ('fixation'). This pattern is called 'saccade and fixate' and is highly conserved over evolution (Land, 2015). Most afoveated animals, like mice, are thought to shift their gaze predominately by moving the head, and secondary eye motion following the head (Land and Nilsson, 2012, e.g. rabbits: Collewijn, 1977, rats: Wallace et al., 2013). Freely moving mice make around one or two gaze shifts per second (Meyer et al., 2018), comparable to human behavior (Einhäuser et al., 2009). However, humans or more general, primates, occasionally shift their gaze by exclusively making a saccade to target a desired object in visual space (Freedman, 2008), taking advantage of the good spatial resolution of the *fovea*.
In head fixed mice, saccade-like eye movements are frequently observed, they can have peak velocities of 1,000°/s and shift the visual field about 5° (Sakatani & Isa, 2007). In fact, head fixed mice exhibit barely non-conjugate eye movements and mainly move their eyes in the horizontal plane (Meyer et al., 2020; Payne & Raymond, 2017; Samonds et al., 2018). Most of these rapid, horizontal eye movements are connected to attempted head movements (Meyer et al., 2020, discussed in Manuscript 2 - Kautzky and Busse, 2020). This promotes the primary role of head movements for gaze shifts, but Zahler et al. (2021) found a specific case, where saccadic eye movements do not follow the head; touch-evoked saccades. Mice were head fixed and

received a tactile stimulus, which evoked saccades that were not preceded by attempted head rotation and targeted to stimulus position. In other species, targeted head and eye movements are often driven by SC (Freedman, 2008; Roucoux & Crommelinck, 1976) and Zahler et al. (2021) could demonstrate involvement of SC in touch-evoked, targeted saccadic motion patterns of mice. Even though this study has been conducted under head fixed conditions, it might illustrate, that gaze shifts in mice are more flexible than so far assumed and saccades can be targeted, at least towards tactile stimuli. But why do mice make saccades, if they do not direct them to specific features in the visual scene? Targeted saccades seem unlikely, if one considers their big visual field of 270° and the in relation relatively small saccades during head fixation. Samonds et al. (2018) posed the hypothesis, that saccadic eye movements serve the purpose of providing the individual visual neurons with novel information. It is known, that neurons adjust and decrease their responsiveness when confronted with constant, unvarying stimuli (Stroud et al., 2012). In fact, Samonds et al. (2018) could show, that saccade size depends on the size of the natural images that were passively viewed by head fixed mice. The smaller the image, the smaller the saccadic eye movements. This seems to be an efficient strategy to sample the environment for visual processing.

In another recent study the neuronal mechanisms around gaze shifts have been investigated. Parker et al. (2022) found distinct dynamics in V1 neurons, when comparing purely compensatory and gaze shifting eye- and head-movements; barely any V1 neurons responded to compensatory head and eye movements, in contrary to gaze shifting motion patterns. Gaze shifts were accompanied by a specific, temporally ordered firing pattern in V1, which was absent in the dark. In head fixed mice, V1 neurons mimicked the response to gaze shifts, when flashed full-field stimuli were shown. Consequently, Parker et al. (2022) hypothesize that V1 responses to gaze shifting head and eye motion patterns could be triggered by changes in the visual scene.

Freely moving mice stabilized a region of enhanced spatial resolution on the retina, the '*focea*', ahead and slightly above them (van Beest et al., 2021). This might be essential for evaluating optic flow arising from locomotion or estimating distance to certain objects in the heading direction of the animal. Both cues are important for navigation, which in mice is supported by eye movements (Bergmann et al., 2022). The stabilization of the '*focea*' seems to also be important for an other complex behavior of mice - hunting small insects. During cricket hunting, mice try to keep the cricket within

the binocular zone, which roughly overlaps with the '*focea*' and monocular mice have proven to be unsuccessful hunters (Hoy et al., 2016; Johnson et al., 2021; Michaiel et al., 2020). Also mice lacking ipsilateral projecting RGCs exhibit inefficient hunting behavior, as Johnson et al. (2021) could show. Four contrast-sensitive RGC types seem to be particularly important for hunting, as they reliably responded to prey stimuli during patch-clamp recordings in isolated retinas (Johnson et al., 2021).
In conclusion, mice, even though their eye sight is not phenomenal, use vision for ecologically highly relevant behaviors, such as hunting, avoiding danger and navigation.

1.4 SCENE STATISTICS OF NATURAL SCENES

As before mentioned, sensory systems have been optimized to the specific characteristics of a species's natural habitat. Probing visual systems with naturalistic stimuli might therefore be inevitable to understand them fully. This idea was already present many years ago, when Brunswik and Kamiya (1953) noticed that some perceptual biases of the human visual system match statistical biases in naturalistic scenes. Brunswik and Kamiya (1953) did not yet know about orientation tuned neurons along the visual pathway, which have been found a bit later, and are now one of the most prominent examples of how the visual system encodes scene statistics. In many natural scene images cardinal orientations are dominant (Coppola et al., 1998; Girshick et al., 2011; Switkes et al., 1978), which is represented in a significant larger portion of visual neurons preferring cardinal orientations over oblique orientation in several animal species (Nasr and Tootell, 2012; Yacoub et al., 2008, monkeys: Shen et al., 2014, cats: Li et al., 2003, ferrets: Coppola et al., 1998, mice: Kreile et al., 2011).
Not only orientations in the visual field are processed by visual neurons, but also luminance is one basic feature of our visual environment. Luminance might be most obvious for us in our everyday live, comparing night- to daylight conditions. But there are also less obvious clues that are transferred by luminance, as it is negatively correlated with depth in natural images (Lee & Potetz, 2005; Samonds et al., 2012). Contrast is another fundamental stimulus dimension encoded by the visual system at various stages and can be defined in different ways. Root mean square (RMS) contrast is often

used to analyze natural scenes (Abballe & Asari, 2022; Bex & Makous, 2002; Mante et al., 2005; Qiu et al., 2021), and seems to be a good indicator of contrast detectability for human subjects (Bex & Makous, 2002; Peli, 1990). It is defined as the ratio of standard deviation of intensities to mean intensity. We investigated naturalistic movies, recorded from a mouse's perspective and found that RMS contrast of UV and green channel differed more in the upper visual field, than in the lower field, i.e. mice' natural habitat above the horizon contains more chromatic information (Manuscript 1 - Qiu et al., 2021). This nicely ties to behavioral findings, that mice can discriminate color in the upper, but not lower visual field (Denman et al., 2018) and also that on a neural basis, color vision is promoted in the ventral retina, looking up into the sky region (Szatko et al., 2020). Another contrast type we used is ON-OFF contrast, which is defined as difference-of-Gaussian (DoG) filters and normalized by sum of center and surround Gaussian (Manuscript 1 - Qiu et al., 2021). ON-OFF contrast can determine the polarity of contrast, and for the natural videos, it is biased towards dark contrast, as shown before (Baden et al., 2013), and higher in the upper part of the scenes. Comparing green and UV channel ON-OFF contrast distributions, we found a wider spread in the UV band. Again this is supporting the idea that the mouse receives more chromatic and contrast information in the sky region. This might be due to the need to detect flying predators as quickly as possible.
An interesting approach to describe the underlying neuronal computations, is to train a convolutional autoencoder, which is trained in an unsupervised manner, to investigate the image reconstruction under certain resource constraints, that are also posed by the visual system. A bottleneck in the visual system is the transmission of information from RGCs to different brain structures under bandwidth limitations (Essen et al., 1991). We trained such an autoencoder with patches of the natural movie scenes, optimized such that the learned filters resemble center-surround RFs similar to RTG RFs. Interestingly UV-green color-opponent filters more often emerged while encoding visual scenes above the horizon (Manuscript 1 - Qiu et al., 2021).
In natural scenes, intensities are commonly spatially correlated. The second-order correlation of intensities in the spatial domain can be examined with the power spectrum in the frequency domain (Geisler, 2008). It can be calculated by summing two-dimensional Fourier power spectra across orientations. When plotting the power of spectra against spatial frequency on a logarithmic scale for two axes, the slope is commonly around -2 for natural images (Field, 1987; Ruderman & Bialek, 1994; Tolhurst et al.,

1992). By randomly reordering the phase spectrum of natural scenes, while keeping the amplitude spectrum, higher-order correlations are removed, whereas second order correlations are preserved. Froudarakis et al. (2014) tested V1 neuron's responses to phase scrambled frames of natural movies, recorded with a camera on top of a mouse's head. In comparison to the original movie frames, the phase scrambled movies evoked less sparse V1 population responses, which decreased the discriminability between movie frames. Consequently, phase spectra, more generally higher-order statistical dependencies seem to carry relevant information for perception of an image (Bolaños et al., 2022; Gerhard et al., 2013; Simoncelli & Olshausen, 2001).
In summary, there are different statistical features of natural scenes, that provide crucial input to the mouse's early visual system. Which makes it a necessity to investigate them further in order to understand how the mouse's visual system processes visual information.

1.5 Setups to record eye motion in mice in naturalistic settings

Mice have a large field of view (180° per eye, Seabrook et al., 2017). To record ecological appropriate stimuli with a camera, it has to be equipped with a fish eye lens and ideally mounted onto a gimbal, to keep the image stable. Additionally both chromatic channels, the mouse retina can perceive, i.e. UV and green light, have to be recorded on separate camera sensors, to acquire detailed information about both. We developed such a 'mouse view' camera system, which furthermore is low-cost and the building instructions are freely available. With this camera, they recorded movies in various different natural settings, that are likely to be mouse habitats, e.g. in a meadow along mouse tracks, or in a forest. The camera was held close to the ground on a gimbal, imitating a mouse's compensatory eye movements to stabilize the gaze (Manuscript 1 - Qiu et al., 2021).
Presenting those movies under laboratory conditions, to record behavioral or electrophysiological reactions of mice, poses some challenges. Off-the-shelf displays, e.g. LCD screens, do not meet the spectral needs of a mouse eye, since they are configured for human vision. Generating visual stimuli for mice requires a stimulator with the option to flexibly choose chromatic channels, like a projector developed by Franke et al. (2019). To accommodate

the visual field of mice, displays have to cover 207° around, also below and above, the animal. One solution is a spherical dome setup, in which the stimuli are projected onto the inner surface of the dome sphere via a spherical mirror (Manuscript 3 - Denman et al., 2017; Kautzky et al., 2022; Muzzu & Saleem, 2022). The spherical mirror introduces spatial distortions to the image projected onto the dome (Bourke, 2005). We developed a simple and efficient calibration procedure, which does not infer information about the specific geometry of the setup (Manuscript 3 - Kautzky et al., 2022). In this dome environment, naturalistic movies can be presented to head fixed mice, meeting chromatic and spatial requirements of the mouse visual system (Manuscript 3 - Kautzky et al., 2022).
However, due to the significant vestibular component in the generation of eye motion in mice (Meyer et al., 2020, discussed in Manuscript 2 - Kautzky and Busse, 2020), it would be ideal to study them in freely roaming mice. To this end, several research groups designed light-weight camera systems, that can record one or two eyes of the animal, the scene around it and, employing a gyroscope, the head position in space, additionally combined with electrophysiological recordings (Meyer et al., 2018; Parker et al., 2022; Sattler & Wehr, 2021). In these three studies, mice were moving in an arena, without naturalistic properties, the next step towards recording in natural surroundings, would maybe be a virtual reality system for freely moving mice (virtual reality system: Stowers et al., 2017), rendering mouse movies as virtual environment.

1.6 FOCUS OF THE THESIS

This thesis comprises three manuscripts which investigate scene statistics in mouse natural environments and how mice move their eyes in natural contexts. In the first part we built a camera system, designed to approximate how the mouse views it's environment (Manuscript 1 - Qiu et al., 2021). Analysis of scene statistics of the recorded footage revealed more chromatic contrast in the upper visual field, which could have driven color opponency in the ventral retina of mice (Szatko et al., 2020). Also overall contrast was stronger in the upper visual field, especially in the UV channel in the sky region, maybe supporting effective predator detection.
The second part of the thesis comprises a discussion of the work from Meyer

et al. (2020) (Manuscript 2 - Kautzky & Busse, 2020). In this study eye movements of mice were recorded in freely moving condition. Meyer et al. (2020) found eye motion to be closely coupled to head movement in two distinct patterns. First, movements of the head relative to the horizontal plane are compensated by eye movements, which results in an alignment of gaze direction to the horizontal plane. The second pattern of eye-head coupling shifts the gaze in a 'saccade and fixate' manner.
Thirdly, we shift the focus to eye movements as response to naturalistic movies (Manuscript 3 - Kautzky et al., 2022). The movies for this study were taken from the dataset produced in the first part of the thesis (Manuscript 1 - Qiu et al., 2021). We developed a hemispheric dome setup to present these movies in an ecologically relevant style, including wide field and UV/green stimulation. To be able to present undistorted images on the dome, we developed a robust method for spatial calibration. We could show that head fixed mice do not orient their towards specific features of the visual scene with saccadic eye movements. But overall eye position during movie presentation compared to mean luminance gray screen, was shifted more ventral and anterior.
In sum, this work offers insight in naturalistic eye motion behavior of mice and the means to further investigate the visual system of mice in context of naturalistic stimuli.

2

NATURAL ENVIRONMENT STATISTICS IN THE UPPER AND LOWER VISUAL FIELD ARE REFLECTED IN MOUSE RETINAL SPECIALIZATIONS

This article was published as:
Qiu, Y., Zhao, Z., Klindt, D., Kautzky, M., Szatko, KP., Schaeffel, F., Rifai, K., Franke, K., Busse, L., Euler, T. (2021) Natural environment statistics in the upper and lower visual field are reflected in mouse retinal specializations. *Current Biology* 9; 31(15):3233-3247.e6, 10.1016/j.cub.2021.05.017.

Contribution summary:

Conceptualization of ideas: Frank Schäffel, Katharina Rifai, Laura Busse and Thomas Euler; Methodology: Yongrong Qiu, Zhijian Zhao, Laura Busse and Thomas Euler, with input from David Klindt and Magdalena Kautzky; Formal analysis: Yongrong Qiu, with input from David Klindt, Laura Busse, and Thomas Euler; Investigation: Yongrong Qiu, Zhijian Zhao, and Klaudia P Szatko, with input from Katrin Franke, Laura Busse, and Thomas Euler; Writing – original draft: Yongrong Qiu, Laura Busse, and Thomas Euler; Writing – review and editing and preparation: Yongrong Qiu, Zhijian Zhao, David Klindt, Klaudia P Szatko, Magdalena Kautzky, Katrin Franke, Laura Busse, and Thomas Euler; Visualization: Yongrong Qiu and Thomas Euler; Supervision: Laura Busse and Thomas Euler; Funding acquisition: Laura Busse, Frank Schaeffel, Katharina Rifai, Katrin Franke, and Thomas Euler

Personal contributions:

I contributed with suggestions and discussions to the design of the hand-held camera and the analysis of recorded movies. Together with the other authors, I reviewed and edited the manuscript, both for the initial submission and the revision.

Article

Current Biology

Natural environment statistics in the upper and lower visual field are reflected in mouse retinal specializations

Graphical abstract

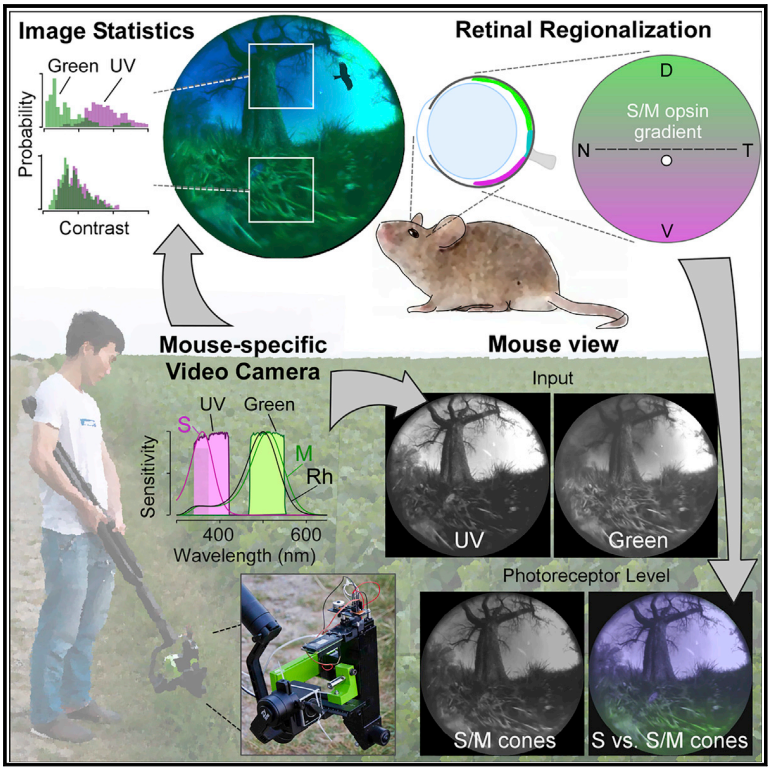

Highlights

- Open-source UV-green camera system for recording footage of mouse habitats
- Natural scenes are rich in UV-green contrast in upper, but not lower visual field
- Upper-field UV-green contrast may have driven ventral color opponency in mice
- Footage recorded at twilight supports a role for UV vision in predator detection

Authors

Yongrong Qiu, Zhijian Zhao, David Klindt, ..., Katrin Franke, Laura Busse, Thomas Euler

Correspondence

busse@biologie.uni-muenchen.de (L.B.), thomas.euler@cin.uni-tuebingen.de (T.E.)

In brief

Pressures for survival drive sensory circuit adaption to a species' habitat, making it essential to characterize natural scenes. Qiu et al. record outdoor footage in the spectral bands relevant for mice—UV and green. Their analyses suggest that chromatic scene statistics shaped dorso-ventral specializations of visual circuits in mice.

Qiu et al., 2021, Current Biology *31*, 3233–3247
August 9, 2021
https://doi.org/10.1016/j.cub.2021.05.017

CellPress

Current Biology

CellPress

Article

Natural environment statistics in the upper and lower visual field are reflected in mouse retinal specializations

Yongrong Qiu,[1,2,3] Zhijian Zhao,[1,2] David Klindt,[1,2,3] Magdalena Kautzky,[4,5] Klaudia P. Szatko,[1,2,3,6] Frank Schaeffel,[1] Katharina Rifai,[1,7] Katrin Franke,[1,2,6] Laura Busse,[4,8,*] and Thomas Euler[1,2,6,9,10,*]

[1]Institute for Ophthalmic Research, University of Tübingen, 72076 Tübingen, Germany
[2]Centre for Integrative Neuroscience (CIN), University of Tübingen, 72076 Tübingen, Germany
[3]Graduate Training Centre of Neuroscience (GTC), International Max Planck Research School, University of Tübingen, 72076 Tübingen, Germany
[4]Division of Neurobiology, Faculty of Biology, LMU Munich, 82152 Planegg-Martinsried, Germany
[5]Graduate School of Systemic Neurosciences (GSN), LMU Munich, 82152 Planegg-Martinsried, Germany
[6]Bernstein Centre for Computational Neuroscience, 72076 Tübingen, Germany
[7]Carl Zeiss Vision International GmbH, 73430 Aalen, Germany
[8]Bernstein Centre for Computational Neuroscience, 82152 Planegg-Martinsried, Germany
[9]Twitter: @teulerlab
[10]Lead contact
*Correspondence: busse@biologie.uni-muenchen.de (L.B.), thomas.euler@cin.uni-tuebingen.de (T.E.)
https://doi.org/10.1016/j.cub.2021.05.017

SUMMARY

Pressures for survival make sensory circuits adapted to a species' natural habitat and its behavioral challenges. Thus, to advance our understanding of the visual system, it is essential to consider an animal's specific visual environment by capturing natural scenes, characterizing their statistical regularities, and using them to probe visual computations. Mice, a prominent visual system model, have salient visual specializations, being dichromatic with enhanced sensitivity to green and UV in the dorsal and ventral retina, respectively. However, the characteristics of their visual environment that likely have driven these adaptations are rarely considered. Here, we built a UV-green-sensitive camera to record footage from mouse habitats. This footage is publicly available as a resource for mouse vision research. We found chromatic contrast to greatly diverge in the upper, but not the lower, visual field. Moreover, training a convolutional autoencoder on upper, but not lower, visual field scenes was sufficient for the emergence of color-opponent filters, suggesting that this environmental difference might have driven superior chromatic opponency in the ventral mouse retina, supporting color discrimination in the upper visual field. Furthermore, the upper visual field was biased toward dark UV contrasts, paralleled by more light-offset-sensitive ganglion cells in the ventral retina. Finally, footage recorded at twilight suggests that UV promotes aerial predator detection. Our findings support that natural scene statistics shaped early visual processing in evolution.

INTRODUCTION

During evolution, the structure and function of neural circuits have been shaped to improve the species's chances to survive and procreate in their specific natural environments. Such adaptations, for instance in eye placement or shape of high-acuity retinal areas,[1] have long been described in the visual system.[2–5] Furthermore, computational modeling (reviewed in Turner et al.[6]) has provided powerful frameworks for relating properties of natural scenes and principles of visual coding. Imposing biologically inspired resource constraints, such as sparseness of firing[7] or a limited amount of hidden units in convolutional autoencoders,[8–10] is sufficient to drive the emergence of spatial filters reminiscent of receptive fields (RFs) in the visual system.

Given such specific adaptations, characterizing the properties of natural visual environments is crucial for advancing our understanding of the structure and function of the visual system,[11] in particular for species with visual systems different from ours, such as mice. Yet studying mouse vision in the context of their natural environment is only starting (reviewed in Krakauer et al.,[12] Datta et al.,[13] and Hasson et al.[14]), despite mice having become a prominent model system for vision research in the past decade (reviewed in Huberman and Niell[15] and Seabrook et al.[16]). The importance of probing the mouse visual system with ecologically inspired stimuli is highlighted by recent work, showing superior spatial frequency tuning for V1 neurons for naturalistic flow stimuli compared to drifting gratings,[17] which might underlie accurate visually driven approach performance during prey capture.[18]

Color is an ethologically highly relevant visual feature: which colors an animal sees will influence its ability to forage and hunt, select mates, and avoid predators. Beyond the absence

of a fovea, a major difference between mice and primates is that mice are dichromats and perceive UV light. Next to a medium (M) wavelength-sensitive opsin peaking at 510 nm (green), mice have a short (S) wavelength-sensitive opsin peaking at 360 nm in the UV range.[19] Due to co-expression of the S-opsin in ventral M-cones,[20–23] the mouse retina is subdivided into a more green-sensitive dorsal and a strongly UV-sensitive ventral half. Notably, ventral cones are tuned to signal dark contrasts[22] and, hence, may support the detection of dark shapes against the sky. Such dorso-ventral retinal regionalization suggests a functional specialization, according to which the ventral retina monitors the overhead space to detect predators,[24,25] whereas the dorsal retina supports foraging and hunting for food.[26,27] Therefore, any statistical analysis of the mouse's visual environment—like quantifying spectral content of natural scenes—should separately consider the upper and lower visual field.

To record and analyze the chromatic information available to UV-sensitive animals, such as mice, we have built a low-cost, open-source camera that is hand-held, mounted on a gimbal for image stabilization, and, unlike standard cameras,[5] covers the spectral bands—UV and green—relevant for mice. We used this camera to record footage near mouse tracks in the field, capturing various outside scenes at different times of the day—providing a resource of natural scenes for vision research in mice, which can be expanded by the community. Focusing on spectral information, we found that the contrast in the two spectral channels greatly diverged in the upper, but not in the lower, visual field, paralleling the superior chromatic opponency in the ventral retina[28] and behavioral color discrimination in the upper visual field.[29] Notably, our analyses suggest that the mouse's UV sensitivity may help detecting aerial predators also at dusk and dawn. Finally, our computational modeling shows that color-opponent filters are more likely to emerge in unsupervised models trained with images from the upper visual field than from the lower visual field. Together, this lends further support to the idea that retinal circuits have evolved to process natural scene statistics in a species-specific manner (reviewed in Baden et al.[1]).

RESULTS

A camera for recording visual scenes from the mouse's perspective

The goal of this study was to capture the visual environment of mice while considering some key aspects of mouse vision. Specifically, we focused on (1) the perspective from only a few centimeters above the ground, (2) the large FOV that approaches ~180° per eye,[30] and (3) the spectral sensitivities of the mouse photoreceptors.[19]

We developed a "mouse camera" that simultaneously captures movies in the UV and green spectral bands using two separate camera modules (Figure 1; Key resources table; STAR Methods; Table 1). The two spectral channels were simultaneously recorded by two Raspberry Pi microcomputers attached to the camera modules. A fisheye lens with a FOV of 180° served as objective (Figures 1A–1E). The camera was mounted on an active gimbal for stabilization and could be moved close to the ground (Figures 1C–1E).

Assuming that eye movements in mice serve mainly to stabilize the retinal image and are typically coupled to head movements[32–35] (but see Zahler et al.[36] for targeted saccades), we restricted our recordings to a view with the horizon oriented parallel to ground and positioned around the middle elevation of the camera image.

The camera modules we used are consumer products and, hence, are optimized for taking color pictures that look natural to humans. This is achieved by a checkerboard-like pattern of thin RGB filters (Bayer filter) coated on the chip surface. While the green Bayer filter matches the spectral sensitivity of mouse rods and M cones ($\lambda_{Peak} \approx 510$ nm),[19,37] it largely blocks UV light. For the UV-channel camera chip, we therefore mechanically removed the Bayer filter layer.[38]

The effective spectral sensitivity of each camera channel results from the combination of bare chip sensitivity, Bayer filter (green channel), and a spectral band-pass filter (Figure 1F). In addition, the cameras automatically adjust image intensities to match gamma curves typically found in consumer displays. To account for these factors, we developed an intensity correction procedure, which we verified using a scanning spectrometer,[22] providing us with intensity-corrected images without substantial over- or underexposure (STAR Methods; Figure S1). Then, the movies from the two channels were temporally synchronized and spatially overlaid, yielding a single UV-green movie (Video S1).

Movie recordings, first-order statistics, and relation to photoisomerization rates in the mouse retina

Next, we used the camera to record footage of representative outdoor natural scenes in places with traces of mouse activity (Figure 2A). Most scenes were recorded in summer and spring during the day and some at twilight (cf. Figure 5).

We first focused on first-order statistics, i.e., brightness, and explored each channel's normalized intensity distribution as a function of elevation (Figure 2B). Examining image patches ("crops") from an example movie, we found that the relative intensities in both channels were usually higher in the upper compared to the lower visual field (Figure 2B, right). Interestingly, intensities of the two chromatic channels were less correlated in the upper compared to the lower visual field (Figure 2C). We therefore quantified the linear correlation between the intensities of the two channels using principal component analysis (PCA)[40] and found a 2–5 times higher variance along the color-opponent axis in images from the upper versus the lower visual field (Figure S3). This indicates a higher variability in chromatic intensity differences, i.e., contrasts, above the horizon. We therefore decided to focus our further analyses on image crops ($(128 \text{ pixels})^2 \approx (53°)^2$) that would be processed by either the dorsal or ventral mouse retina. Considering that the mouse eye is tilted ~22° toward the sky,[41] we selected image crops located well above and below the camera's midline. To account for the substantial variations of brightness of the recorded scenes, depending on time of day, weather, and scene content (compare Figure 2A left-center versus right-top), we decided to split the footage cropwise into three groups (Figures 2D and 2E) using mean intensity as a simple yet objective criterion (STAR Methods; Table S1) and performed all subsequent analyses for each of these mean intensity classes (I_{1-3}).

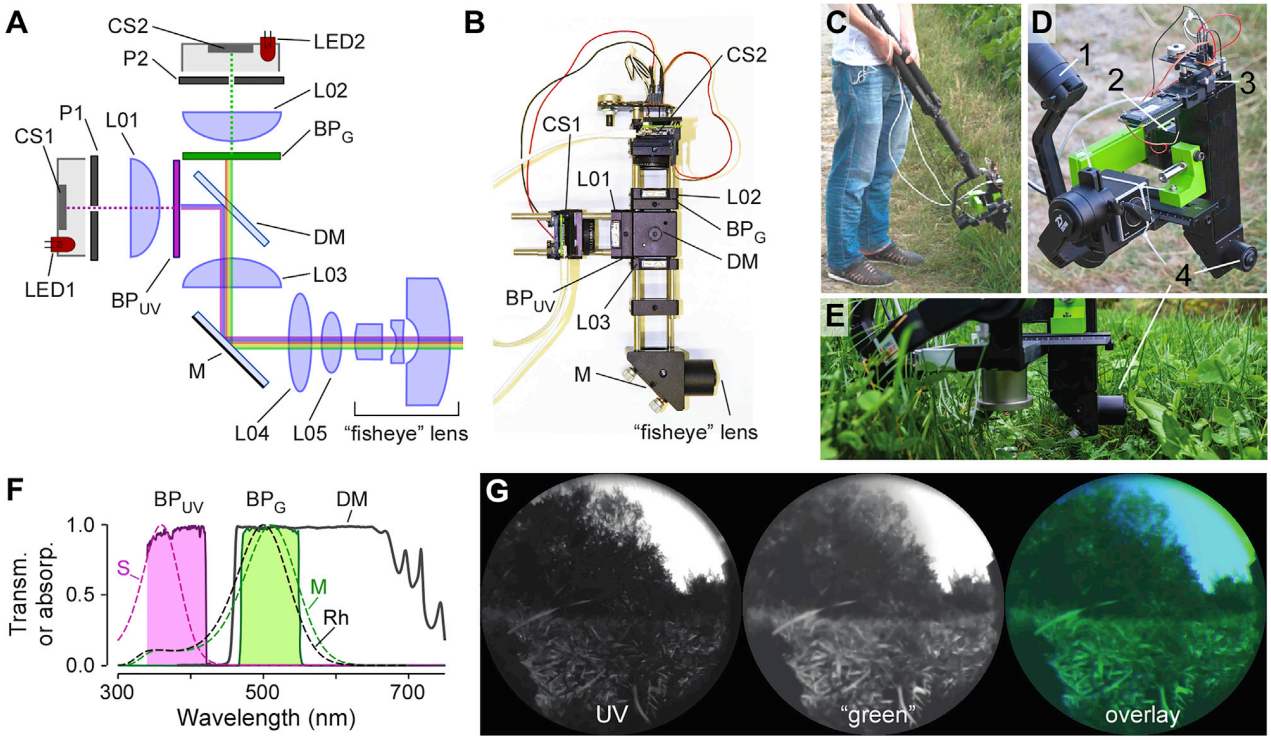

Figure 1. Mouse camera module

(A) Schematic drawing of mouse camera with two spectral channels (UV, green). BP_G, green bandpass filter (470–550 nm); BP_{UV}, UV bandpass filter (350–419 nm); CS, camera sensor; DM, dichroic mirror (>90% reflection: 350–442 nm; >90%, transmission: 460–650 nm); L01–05, lenses; LED, light-emitting diode; M, silver mirror; P, pinhole.

(B) Picture of the assembled camera module.

(C–E) Pictures of assembled camera module, with gimbal (1), UV camera (2), green camera (3), and fisheye lens (4).

(F) Normalized transmission spectra of DM, BP_{UV}, and BP_G, with normalized absorption spectra of mouse cone opsins (S and M) and rhodopsin (Rh) overlaid.[31]

(G) Movie frame with UV (left), green (center) channel, and overlay (right).

See also Figure S1 and Video S1.

The recorded movies represent some of the information that would be available to mice in the environment; what reaches the mouse retinal circuits will additionally depend on factors, such as pupil size, filtering of the mouse eye optics, opsin spectral sensitivities and expression patterns, and photoreceptor collection area. To simulate what our footage would look like at the photoreceptor level, we estimated from our image crops expected photoisomerization rates, considering the aforementioned parameters, including opsin co-expression in the ventral retina (STAR Methods; Table S1; Figures S2A and S2B). Not unexpectedly, we found that dominant S-opsin co-expression allows ventral M cones to better pick up contrast in the upper visual field (Figure S2C)—at the cost of much reduced UV/green chromatic contrast sensitivity. Besides cones, rods have also been implicated in generating color opponency in the mouse retina.[28,42] Having similar spectral sensitivity as M cones, rods may provide the "green image" for ventral retinal circuits. Therefore, we estimated rod photoisomerization rates (Figure S2B, right) and found that rod signals may be able to recover the available chromatic UV-green contrast (Figure S2D) and, hence, support S cone versus rod color vision in the upper visual field—at least for scenes up to the medium mean intensity group (Discussion).

Chromatic contrast is higher in the upper versus the lower visual field

Retinal output to the rest of the brain is also driven by second-order statistics, such as differences in brightness, i.e., contrast.[43–45] To assess chromatic contrast, we next compared the contrast distribution in the chromatic channels in our natural scenes above

Table 1. Camera settings

Parameter	UV camera (CS1)	Green camera (CS2)
Resolution	(720,540)	(720,540)
Frame rate (Hz)	25	25
Exposure_mode	off	off
Shutter speed (ms)	35	35
ISO	800	100
Analog_gain	8.0–8.2	1.0–1.2
Awb_mode	off	off
Awb_gains	(1,1)	(1,1)
$P = av^b + c$, with normalized pixel value v, and power P (in [μW])	a = 0.741, b = 2.102, c = 0.015	a = 6.197, b = 4.331, c = 0.366

and below the horizon and across the three mean intensity groups (Figure 3).

We first focused on root mean square contrast (C_{RMS}), commonly used in psychophysics for describing contrast in complex natural scenes.[43,46] We extracted circular image patches (kernels) of various diameters (d_{RF}, 2°–14°), a range that includes the RF center sizes of mouse RGC types, from 3° (≈90 μm) for UHD[47] and F-mini cells[48] to 13° (≈400 μm) for sOn alpha cells,[49] and computed C_{RMS} as standard deviation of the normalized pixel intensities divided by mean intensity. To quantify differences between C_{RMS} distributions, we used a two-sided permutation test (distribution medians; statistics summarized in Tables S2 and S3) and the Jensen-Shannon divergence (JSD), which measures the general similarity between probability distributions, with JSD = 0 indicating identical distributions.

Our analysis of the C_{RMS} distributions across 1,500 crops revealed two key features of the recorded mouse natural scenes (Figure 3): first, as illustrated by two representative examples (Figures 3A–3C; upper two versus lower two rows; from Videos S1 and S2), C_{RMS} distributions of the UV and green channel differed more strongly in the upper compared to the lower visual field (for median and JSD, see Figures 3F and 3G). Second, for the tested kernel sizes, C_{RMS} increased with kernel diameter (see examples in Figure 3B; compare Figure 3D versus 3E; for median and JSD, see Figures 3F and 3G), consistent with the dominance of low spatial frequencies in natural scenes.[50–52] The differences in C_{RMS} distribution between chromatic channels and upper versus lower visual field were significant (Tables S2 and S3) for all kernel diameters except in the high mean intensity group.

The differences in JSD between upper and lower visual field likely reflect differences in chromatic contrast: when plotting green C_{RMS} as a function of UV C_{RMS}, the data points for the lower visual field tended to be distributed tightly along the identity line (e.g., Figure 3D_1 and 3E_1, bottom), indicative of a high correlation between the channels and, thus, low chromatic contrast. For the upper visual field, however, the C_{RMS} distributions for UV compared to green were broader and shifted toward higher values, in particular for larger RF kernel diameters (e.g., Figure 3E_1, top), suggesting a lower channel correlation and high chromatic contrast, respectively.

In summary, we found that, except for bright scenes, UV-green chromatic contrast was higher in the upper compared to the lower visual field, particularly for the large RF kernel diameters (Figure 3G). Taken together, this suggests that the natural environment of mice above the horizon is rich in chromatic information, which may preferentially drive color-opponent RGCs with large RFs.

Natural scenes are biased toward dark contrasts

It has been reported that the contrast distribution of (monochromatic) natural scenes is biased toward dark (negative) contrasts and that this bias is mirrored in the higher proportion of Off- versus On-responding neurons in the early visual system.[39,53,54] Therefore, we studied the distribution of dark and bright contrasts in our scenes (Figure 4). To measure the contrast polarity distribution ("On-Off contrast," C_{On-Off}) in each channel, we convolved the crops separately with the center and surround of difference-of-Gaussian (DOG) kernels of various diameters (d_{RF}, 2°–14°) and computed the Michelson contrast between center and surround (Figures 4A–4C).[39] Like for C_{RMS}, we analyzed the distributions of C_{On-Off} separately in both chromatic channels for the mean intensity groups (Figures 4D–4F; statistics summarized in Tables S2 and S3).

In crops with low and medium mean intensities, we found the C_{On-Off} distributions—despite being wide—to be skewed to negative values, particularly in the upper visual field and for larger RF kernel diameters (for examples, see Figures 4A–4C; for distributions, median, and JSD, see Figures 4D–4G and S4A; Tables S2 and S3). The dark bias in upper visual field scenes resonates with earlier results,[22] showing that mouse cones that survey the sky preferentially encode dark contrasts and suggesting a neural representation bias that starts already at the cone level.

We next asked whether such a neural representation bias is also present in the retinal output, where we would expect a bias toward Off responses in ventral, large-RF RGCs. To test this prediction, we exploited a published dataset of visually evoked RGC responses recorded in ventral retina.[55] For each cell, we extracted an On-Off index (OOi), which indicates whether a cell responds more strongly to light-on ($OOi > 0$) or light-off transitions ($OOi < 0$), and RF diameter (d_{RF}) (Figures S4B–S4F; STAR Methods). We found that, indeed, Off cells with large RF ($d_{RF} > 8°$, equivalent to >240 μm in diameter) displayed a dark-biased OOi (Figure S4C) and were more frequent than their On counterparts (Figure S4D). This finding is consistent with the skewed distributions toward dark contrasts in our footage, suggesting that the Off preference in large-RF RGCs reflects retinal circuit adaptations toward exploiting the dark bias present in natural scenes above the horizon.

We also compared the C_{On-Off} distributions in the two channels and found chromatic On-Off contrast (quantified as JSD; Figure 4G) to be systematically higher in the upper visual field, with the exception of the high mean intensity group. Moreover, like for C_{RMS}, the C_{On-Off} distribution seemed broader for UV, supporting that the mouse's UV channel may provide the animal with more nuanced information about the sky region than the green channel.

UV channel for predator detection?

So far, we focused on footage recorded during daytime, and while mice are active during the day,[56] they also forage from dusk till dawn. We thus asked whether UV sensitivity was also useful for detecting objects in the twilight sky and recorded footage before sunrise and after sunset (Figure 5). Previous measurements of the spectral composition of sunlight over the course of a day revealed an overrepresentation of short wavelengths during twilight (increase in ratio between 360 nm and 520 nm).[57,58] Because of the camera's relatively low sensitivity, we recorded movies in the direction of the sun from a fixed camera position (Figure 5A) and restricted our analysis to the upper visual field, where the image crops met our exposure criteria (STAR Methods).

First, we explored for the example frames the intensity profiles along a 70° arc starting at the sun's position (Figure 5B). In the sun's vicinity, the intensity in the green channel was always higher than that in the UV channel, whereas further away from

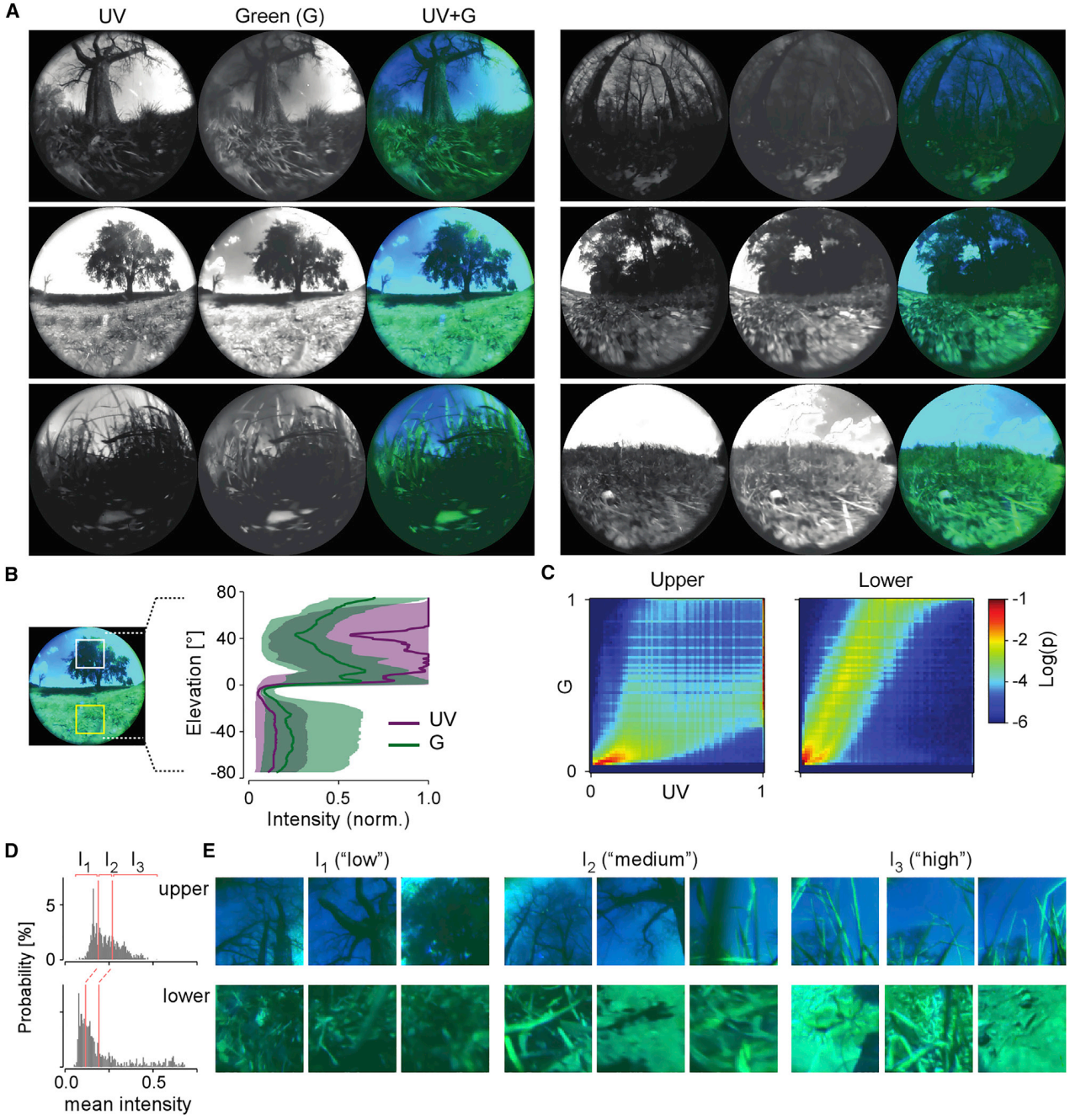

Figure 2. Example scenes and intensity distribution

(A) Example frames (UV, green, and overlay) from movies of different scenes recorded outside in the field (near Waldhäuser Ost, Tübingen, Germany; 48°33'02.4"N 9°03'01.2"E).

(B) Normalized intensity for green (G) and UV as a function of elevation across the n = 1,936 frames of one example movie (median w/ 25th and 75th percentile).

(C) 2D histograms of intensities of the same movie as in (B), visualizing the G-UV intensity distribution for an image cut-out (crop) in the upper (left) and lower (right) visual field (for crop placement, see white and yellow boxes in B, left, respectively; Pearson correlation coefficients G-UV: upper, 0.64 ± 0.20; lower 0.83 ± 0.07; R^2 for linear regression: upper, 0.45 ± 0.18; lower, 0.69 ± 0.12).

(D) Distribution of mean intensities for 1,500 image crops from upper and lower visual field, selected randomly from 15 movies, and division into 3 intensity classes (percentiles I_{1-3}).

(E) Example image crops ((53°)^2) from the three mean intensity classes.

See also Figure S2 and Table S1.

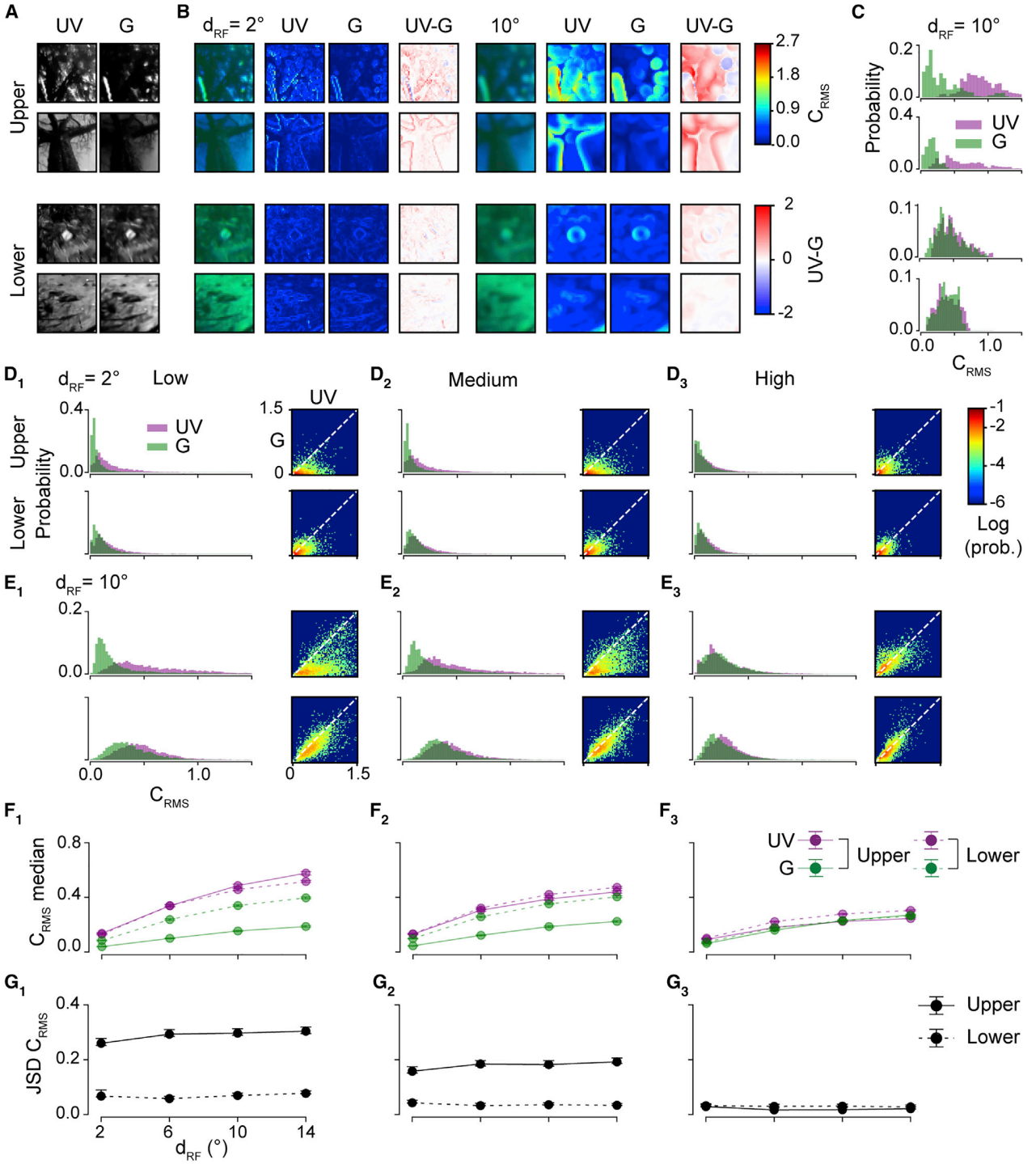

Figure 3. Chromatic contrast is higher in image crops from the upper visual field

(A) Examples for image crops ((53°)^2) from upper and lower visual fields (each from mean intensity classes I_1 and I_2).

(B) Images from (A) filtered with different receptive field (RF) diameters, d_{RF}, with each of the columns showing (from left): UV-green overlay, UV and green channel maps visualizing RMS contrast (C_{RMS}), and difference between maps (UV-G).

(C) Distributions of C_{RMS} for UV and green for d_{RF} = 10°.

(D and E) 1D (left) and 2D histograms for C_{RMS} of all n = 1,500 image crops from randomly picked frames (out of n = 15 movies) for the three intensity groups (I_1–I_3 from Figures 2D and 2E) and d_{RF} = 2° (D) and d_{RF} = 10° (E).

(F) Median C_{RMS} as a function of RF size for UV and green channels in the upper (solid lines) and lower (dashed) visual field, for the three intensity groups.

(G) Like (F) but with median Jensen-Shannon divergence (JSD) between C_{RMS} distributions of the two chromatic channels as a function of d_{RF}.

Error bars in (F) and (G) represent 2.5 and 97.5 percentiles with bootstrapping (STAR Methods). See also Figure S3, Tables S2 and S3, and Videos S1 and S2.

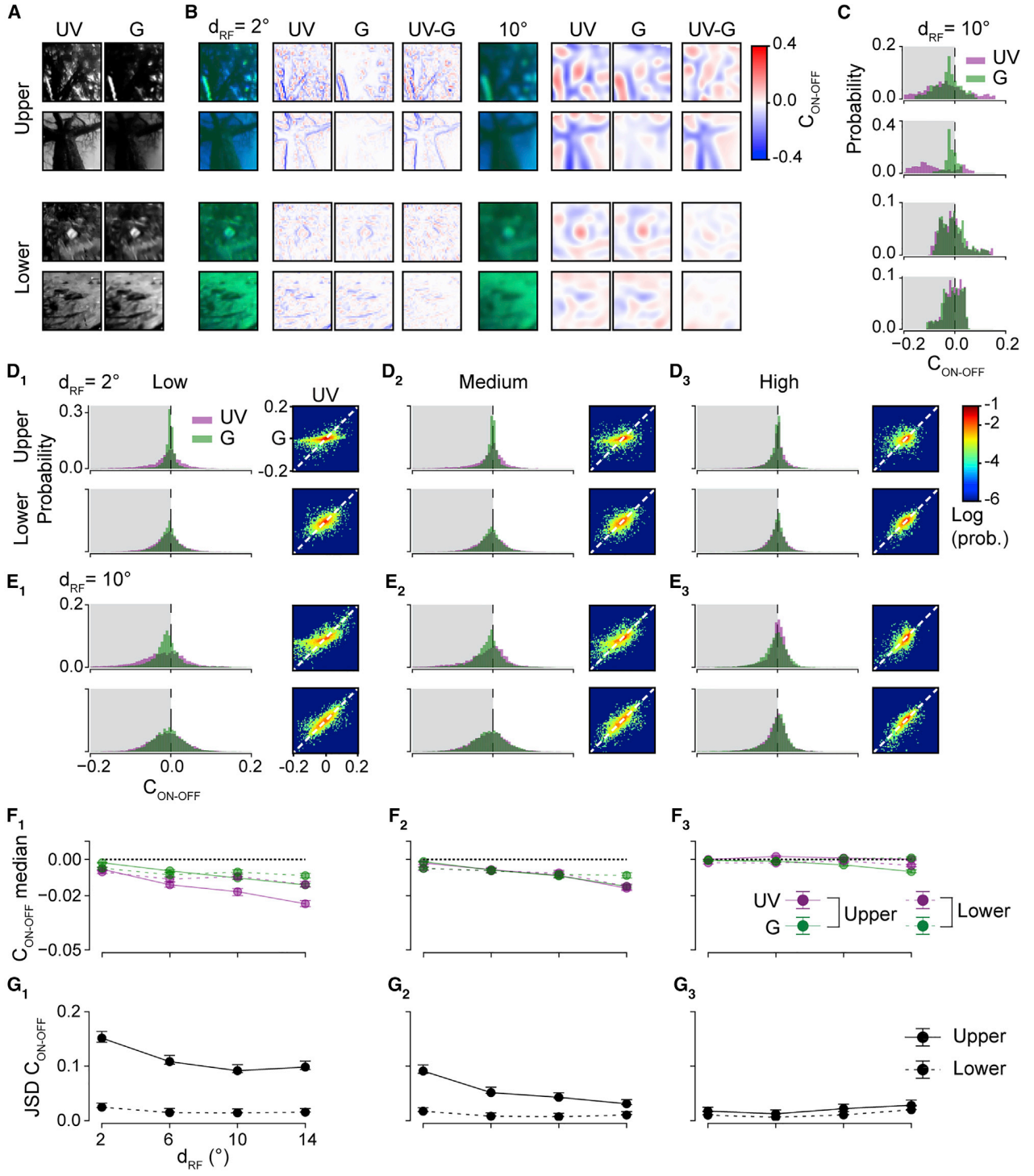

Figure 4. The upper visual field is biased toward negative contrast

(A) Example image crops from upper and lower visual field (same as in Figure 3A).

(B) Images from (A) after application of On-Off filter kernel (STAR Methods) with different RF diameters, d_{RF}, with each of the two columns showing the UV-green overlay (left), UV (center), and green (right) channel maps visualizing On-Off contrast (C_{On-Off}).

(C) Distributions C_{On-Off} for UV and green for a medium-sized d_{RF} of 10°.

(D and E) 1D (left) and 2D histograms for C_{On-Off} of all n = 1,500 image crops from randomly picked frames out of n = 15 movies for the three intensity groups (I_1–I_3 from Figures 2D and 2E) and d_{RF} = 2° (D) and d_{RF} = 10° (E).

(F) Median C_{On-Off} as a function of d_{RF} for UV and green channels in the upper (solid lines) and lower (dashed) visual field for the three intensity groups.

(legend continued on next page)

the sun, UV and green reached similar intensity levels (Figure 5B; e.g., profiles from image no. 4 for >55°), in line with earlier observations.[57] Moreover, for distances larger than ~5° from the sun, the UV intensity profile was much flatter than that of green, resulting in a more homogeneous UV illumination of the sky. Finally, in the sky's dome, the intensity rose faster for UV compared to the green over the course of the sunrise (Figure 5C). Akin to daytime scenes, C_{RMS} was significantly higher in the UV than the green channel (Figure 5D; $p < 0.0001$, for all images, two-sided permutation test, n = 10,000 repeats) and increased with kernel diameter (Figure 5E).

Together, these characteristics render the UV channel suitable for object detection, in particular for dark objects in front of a brighter (twilight) sky. We tested this hypothesis with a black drone mimicking an aerial predator (Figure 5F). As predicted, the drone was much more easily detectable in the UV versus the green channel, which likely holds also for birds preying on mice during twilight. Therefore, the UV channel may contribute to increasing the species' survival chances in their natural habitat (Video S3).

Autoencoder model predicts color opponency in the ventral retina

Until here, we characterized the contrast statistics of scenes from the mouse natural environment and found significant differences in chromatic contrast between upper and lower visual field. Next, we explored whether these differences can give rise to color opponency and, hence, shape neural representations. Recently, Ocko et al.[10] trained a convolutional autoencoder (CAE)[8,9] model to reconstruct pink $(1/f)$ noise and showed that the model learned spatial filters with center-surround organization resembling the RFs of different RGC types. Thus, we next asked whether such CAE models can also learn color-opponent RFs (Figure 6).

Convolutional autoencoders are trained in an unsupervised way to closely match the input, while featuring a resource constraint ("bottleneck") that forces them to capture reconstruction-relevant features. This conceptually resembles the early visual system, where the information flow from the retina to downstream targets in the brain is constrained by bandwidth limitations.[59–61] Given the resource constraint in the network, investigating the representations (kernels) in the hidden layers can reveal interesting structure in the data.

We optimized our CAE model to yield good reconstructions under the qualitative constraint that the learned filters resemble smooth, center-surround RFs (Figure S5; STAR Methods). We then quantified the model's performance in reconstructing the input images (Figure 6B) using structural similarity (SSIM)[62] as metrics. Qualitatively, we searched for hyperparameter combinations that used smooth center-surround-like kernels to reliably yield good reconstruction performance (SSIM $\geq$ 0.6; Figure 6C; STAR Methods). For these combinations, we ran the model (n = 10 random seeds; kernel sizes: 5×5, 9×9, and 13×13 pixels) and determined whether the number of color-opponent spatial kernels differed between the upper versus lower visual field (Figure 6D). Kernels were considered color opponent if their UV and green channel were negatively correlated ($p < 0.05$; Pearson correlation; Figure 6C).

We found that, except for the smallest kernel size (5 × 5 pixels ≈ $(4.1°)^2$), color-opponent kernels were significantly more frequent in CAEs trained with scenes from the upper versus the lower visual field (Figure 6D; for statistics, see Table S4). This suggests that, in systems with bottleneck and for sufficiently large kernel sizes, UV-green color-opponent kernels preferentially emerge when encoding visual scenes above the horizon.

We compared our CAE with classical approaches (PCA and zero-phase component analysis [ZCA] whitening; STAR Methods) that explain the unsupervised emergence of color-opponency[40] or center-surround RFs from natural stimuli.[63,64] However, although both found more color-opponent kernels with upper visual field images (Figure S3), the kernels either did not resemble the center-surround RFs of RGCs (PCA; Figure 6E) or were small and mainly different in spatial position (ZCA whitening; Figure 6F). In summary, all three unsupervised models confirm that specific chromatic statistics in the upper visual field may be sufficient to drive the emergence of color-opponent spatial RFs.

DISCUSSION

Using a custom-built camera with spectral channels matching the UV and green sensitivities of mouse photoreceptors, we captured movies from the natural visual environment of mice. Statistical analyses of scenes from these movies revealed that chromatic contrast was stronger above the horizon and that such contrast would preferentially drive large RFs. This enrichment of chromatic contrast in the upper visual field might underlie the preferential emergence of color-opponent RFs found in the ventral retina, as suggested by a CAE model trained to represent UV-green scenes. Furthermore, we found the upper visual field, and in particular the UV channel, to be biased toward dark contrast, which indicates that UV could be an important source of information about dark objects (i.e., birds) against a brighter sky. Together, our findings lend further support to the idea that retinal circuits have evolved to optimally process natural scene statistics (reviewed in Baden et al.[1]).

Recording natural scenes

Capturing the spectral information in the environment beyond the limits of human perception has been successful with hyperspectral imagers (reviewed in Nevala and Baden[65]). Here, typical solutions use different species-matched interference filters iteratively placed in front of a camera chip with broad spectral sensitivity[66] or scanning spectrometers.[22] In both cases, acquisition of a hyperspectral image is slow and does not allow recording movies. Instead of relying on an existing imager, we designed

(G) Like (F) but with JSD between $C_{On\text{-}Off}$ distributions (cf. 2D plots in D and E) of the two chromatic channels as a function of d_{RF}. Error bars represent 2.5 and 97.5 percentiles with bootstrapping (STAR Methods). Note that, for larger RF kernel sizes, the distribution mode was slightly shifted to negative values (e.g., E), yet, when pooling images across chromatic channels, visual fields, and intensity groups, the distribution mode of all four kernel sizes was at zero (data not shown), in line with earlier observations.[39]
See also Figure S4 and Tables S2 and S3.

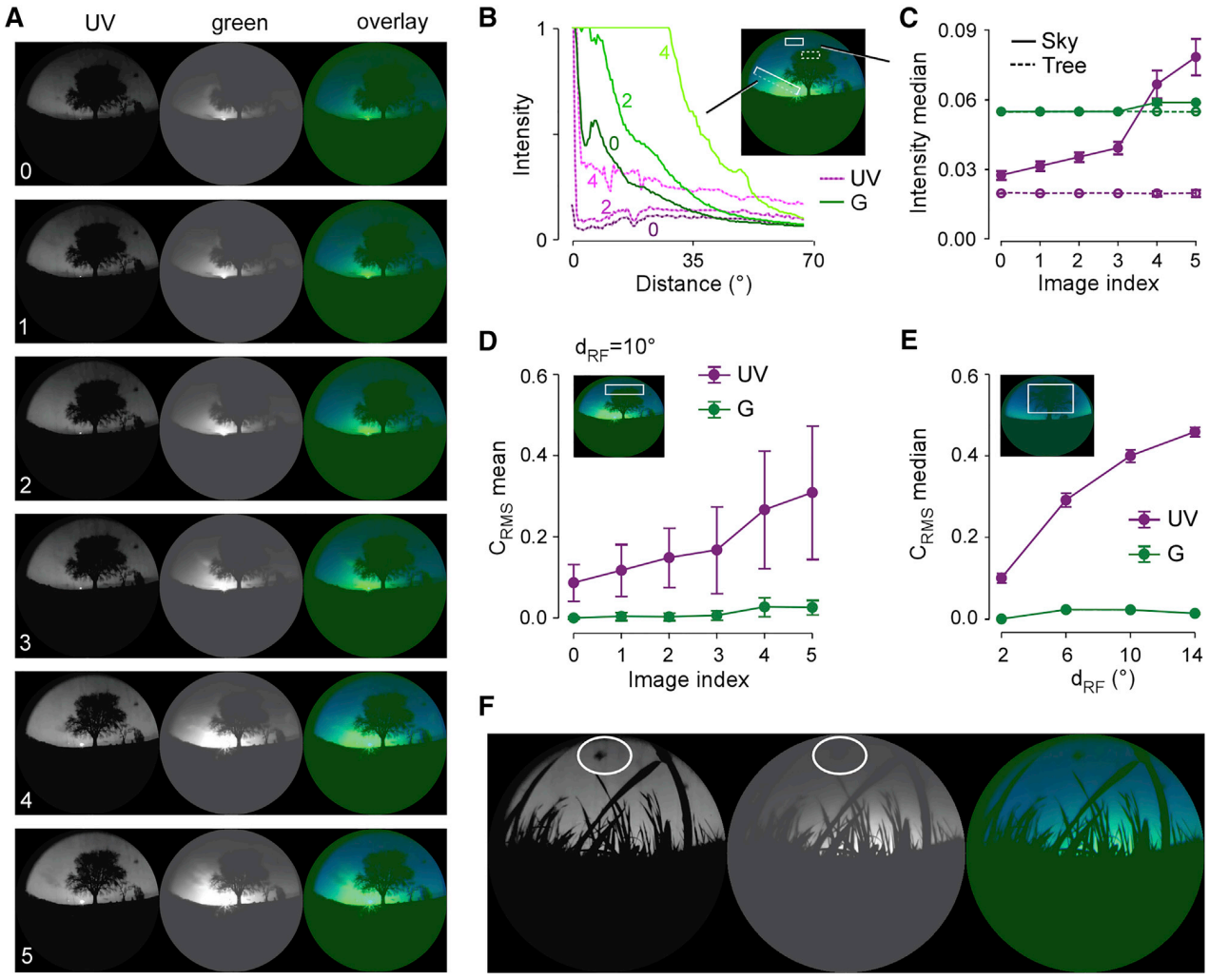

Figure 5. UV channel might facilitate detection of dark shapes in the upper visual field also at dusk and dawn

(A) Representative scene recorded with the mouse camera at sunrise (image 0) and in the following 15 min (time between images ~3 min; for image 5, the solar angle was ~3° above the horizon).

(B) Intensity profiles along a line (dashed, see inset) starting at the sun for images from (A).

(C) Median intensities in two image crops (see inset in A; dashed box, tree; solid box, sky) as function of image series index.

(D) C_{RMS} (mean) in image crop at the edge of a tree (rectangle in inset) as function of image index.

(E) C_{RMS} (median) in image crop placed on the tree (rectangle in inset) as function of RF kernel diameter (d_{RF}).

(F) Image showing an approaching black drone mimicking a bird of prey.

Panels recorded at dawn (A–D) and dusk (E and F). Error bars in (C)–(E) represent 2.5 and 97.5 percentiles with bootstrapping. See also Video S3.

a simple system with two Raspberry Pi camera chips, one for UV and one for green. By relying on open-source, low-cost, easily reproducible, and portable hardware and by setting up a public repository for our videos, we envision that—as a community effort—our initial collection will turn over time into a more general footage of mouse natural environments, covering more scenes, environments, seasons, and times of day.

The main disadvantage of our choice was the chip's relatively low light sensitivity, which restricted recordings of natural scenes to daytime and twilight. With other cameras—e.g., smartphone cameras optimized for low-light recordings—a more night-time-enabled mouse camera with a larger dynamic range may be in reach. A further improvement may be opsin-matched filters.[66]

Mouse camera movies as natural stimuli

Stimuli used in vision research cover a broad spectrum, ranging from artificial stimuli, like gratings and noise (reviewed in Rust and Movshon[67]) or screen-rendered 3D objects,[68,69] to more naturalistic ones.[70–72] The movies recorded here represent suitable natural stimuli to probe mouse vision: (1) they were recorded outdoors in places where mice can be seen at daytime and (2) contain the spectral bands perceived by mice. With a UV-capable stimulator, they should drive the mouse visual system better than gray-scale stimuli on a standard monitor (discussed in Franke et al.[31]). (3) Because our camera was gimbal mounted, the movies approximate well the input reaching the mouse's eye, as a large fraction of mouse eye movements serves to stabilize the retinal image in

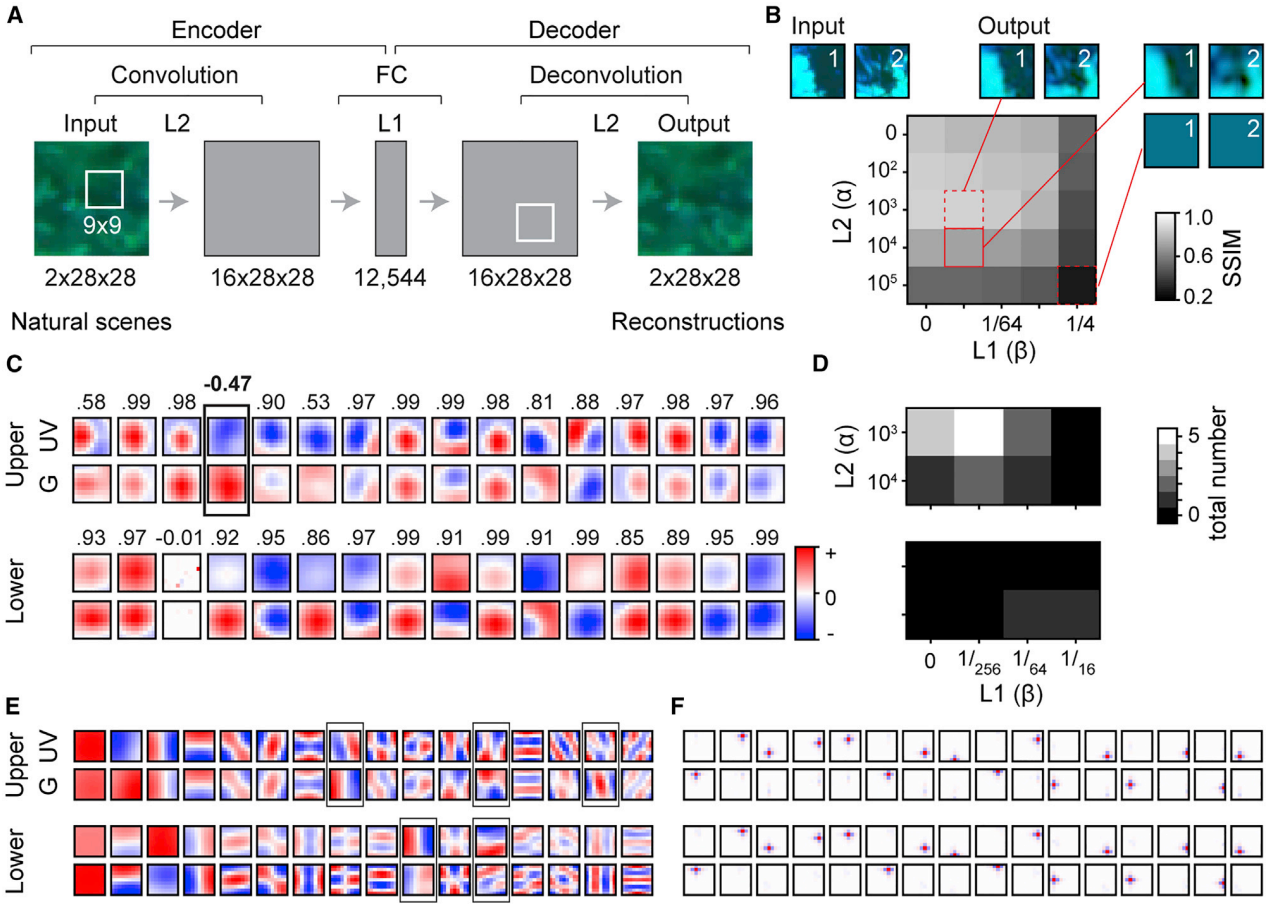

Figure 6. Convolutional autoencoder (CAE) model learns color-opponent kernels from upper visual field footage

(A) Architecture of the CAE model (FC, fully connected; numbers indicate feature shapes; for details, see STAR Methods).

(B) Reconstruction performance measured as structural similarity (SSIM) under different regularization strengths α (L2 regularization) and β (L1 penalty; STAR Methods), with two example images (input; top left) and the corresponding CAE outputs depicted for certain combinations of α and β (red boxes). Training images from all three mean intensity groups I_{1-3} (for results for $I_{1,2}$ and I_3 only, see Table S4).

(C) Convolutional kernels learned by the model from upper (top) and lower (bottom) visual field scenes (for $\alpha = 10^4$, $\beta = 1/256$; see solid red box in B; correlation indicated above each kernel pair; $p < 0.05$ for all kernel pairs except third one in bottom row [$p = 0.9$]). Example for color-opponent kernel indicated by box is shown.

(D) 2D histogram showing total number of color-opponent kernels per random seed learned from upper (top) and lower (bottom) visual field scenes (n = 10 random seeds).

(E and F) 16 kernels for UV and green, each for upper and lower visual field crops; same presentation and dataset as in (C). In (E), first kernels from PCA are shown (STAR Methods), with color-opponent kernels indicated by boxes. The color opponency index (COi) (cf. Figure S3 and STAR Methods) of the upper and lower visual field is 0.0393 and 0.0182, respectively. In (F), randomly selected kernels from ZCA whitening are shown (STAR Methods). Here, all 162 kernels (9x9×2 channels; cf. A) were color opponent for the upper visual field, while only 143 were color opponent for the lower visual field.

See also Figure S5 and Table S4.

the presence of head movements.[33] Nonetheless, our footage is limited, as it does not include fast shifts of perspective, as might be expected from orienting movements, e.g., shifts of gaze arising from combined eye-head movements.[33] A first validation of these stimuli could be to test whether they allow separating anatomically defined RGC types that so far could not be reliably disambiguated based on their responses to standard synthetic stimuli.[55]

Retinal opsin gradient, color opponency, and color vision in mice

Our scene analysis revealed that chromatic contrast was higher in the upper visual field. As suggested by the autoencoder model, this might have driven, over the course of evolution, the presence of color-opponent cells in the ventral retina. In line with this prediction, a recent neurophysiological study showed that color-opponent RGCs are indeed more frequent in the ventral retina.[28] Moreover, mice perform better in color discrimination task when stimuli were presented in the upper visual field.[29]

However, this interpretation seems at odds with the fact that M cones in the ventral mouse retina co-express both opsins,[20] with S-opsin dominating.[20–22,73] Such regional opsin co-expression found in mice and other vertebrates (reviewed in Peichl[74]) constitutes a challenge for a color opponency mechanism that

compares signals from spectrally distinct cone types. This conundrum may be resolved by involving rod signals: indeed, some of the color-opponent mouse RGCs rely on antagonistic center-surround RF mechanisms, with the RF center dominated by signals from UV-sensitive S/(M) co-expressing cones and the green-biased RF surround mediated by rods[28,42] and/or by long-range inputs from dorsal M cones.[75] These mechanisms rely on pooling signals from a large surround, which resonates well with our finding that larger RF cells should be better in picking up chromatic contrast.

Up to which light levels are mouse rods responsive such that they can contribute to color vision? The rod photoisomerization rates we estimated for images in the medium mean intensity group (I_2) seem to roughly match those used in the recording studies that demonstrated S cone versus rod color opponency,[28,42] indicating that mouse rods may be active in the photopic range. Indeed, recordings in retina, dorsolateral geniculate nucleus,[76] and V1[77] suggest that mouse rods can escape saturation for photoisomerization rates 10–100 times higher than those we estimated. Taken together, rods could play a role in daytime (color) vision in mice.

If chromatic regionalization of the retina was evolutionarily advantageous, why is it not more widespread among critters in similar habitats? Some members of the subfamily Murinae, like the steppe mouse (*Mus spicilegus*), share S/M opsin regionalization with the house mouse (*Mus musculus*), whereas others lack it (*Apodemus sylvaticus*) or have lost the S-opsin (*Apodemus microps*).[78] Interestingly, these *Apodemus* species live in shrubberies, where a "bird-in-the-sky" detector may not be as useful as in relatively open spaces, as inhabited by *M. spicilegus*. Hence, retinal regionalization found in some mouse species may reflect an environmental adaptation—akin to the UV-sensitive "strike zone" in the ventral retina of zebrafish larvae, which helps the animal detect UV-reflecting prey and avoid dark predators in the upper visual field.[79] Reminiscent of this "strike zone" is the S cone "hotspot" recently described in the ventral mouse retina.[23]

Note that such dorso-ventral specialization seems only useful if upper and lower visual field is reliably projected onto ventral and dorsal retina, respectively. Indeed, mouse eye movements are tightly coupled to head movements and often stabilize the retinal image relative to the ground,[32,33,35,72] likely ensuring that the temporo-nasal retinal axis is largely aligned with the horizon.

UV vision in mice

UV sensitivity is thought to play an important role in the behavior of many animals. One of the earliest reports on the many roles of UV vision was published by Wilson,[80] showing that locusts use UV contrast between sky and ground to detect the horizon.[81] In addition to navigation, UV vision was also implicated in communication, foraging, and predator and prey detection (reviewed in Cronin and Bok[82]). In rodents, UV vision has been mainly discussed in the context of communication via urine marks[42,83] and predator detection,[22] but it may also play a role in foraging with respect to enhanced chromatic contrast of foliage[66] and fruit.[84]

Our results shed light onto why mice specifically profit from UV sensitivity for predator detection: first, consistent with previous studies,[22,82] our results suggest that, during daylight, UV sensitivity enhances the detection of dark silhouettes against the brighter sky. Second, at twilight, when the spectrum becomes more dominated by short wavelengths,[57] we estimated from our footage that the intensity of the sky's dome at sunset was equivalent to ~3,000 R^*s^{-1} per S cone. This is clearly above the S cone's threshold of ~20 R^*s^{-1} per cone[85] and suggests that S cones stay responsive during twilight. Third, at lower intensities, when rod photoreceptors dominate,[85] UV light from the sky may still play a role, because rhodopsin—like any opsin—features a secondary sensitivity peak ("beta band") around ~350 nm.[86] Therefore, mice may perceive near-UV at low light levels via rods.[82]

Bias toward dark contrasts

In line with our own findings, previous studies showed that the distribution of contrast in natural scenes is biased toward dark contrasts.[39,87] The dark bias in our footage was more prominent in the upper visual field and specifically in the UV channel, which resonates well with earlier retinal recordings showing that light-off steps are particularly faithfully encoded by ventral cones.[22] Our analyses of RGC responses from a published dataset[55] revealed that, in ventral RGCs, dark contrasts elicited stronger responses than bright contrasts, suggesting an overrepresentation of Off information in the visual system.[88–90] Interestingly, the dark bias was most prominent in large-RF RGCs, which ties into an ongoing controversy whether Off cells are expected to predominantly feature large[87] or small RFs[39] (discussed in Mazade et al.[91]).

For animals such as mice, the early detection of dark shapes (e.g., aerial predators) against the brighter sky is crucial for their survival. Whether and to which degree the observed dark preference for large-RF RGCs plays a direct role in predator detection will need to be directly tested in future studies. Past studies have implicated different mouse RGC types in this task, including the small-field local edge detector (LED)/WB3 cells, which respond to small, dark objects that move,[25] and the large-field transient Off alpha cells, which signal dark looming stimuli.[92] One recent study showed that VG3 amacrine cells, which feed into several RGC circuits, respond to expanding shadows and thus may be involved in predator detection as well.[93] Overall, this indicates that predator detection presumably relies on multiple RGC channels, including some with small and some with larger RF sizes.

Are natural scene statistics encoded in mouse retinal circuits?

Autoencoders have long been used to learn efficient representations by imposing a resource constraint in the network.[9,94] Therefore, they are a natural choice for exploring feature transformations in the early visual system, where visual information has to pass the anatomical constraint of the optic nerve, posing a bottleneck between the retina and its downstream targets. For instance, in the mouse retino-geniculo-cortical pathway, 25%–40% of the estimated 45,000 RGCs[95] project to the dorsolateral geniculate nucleus of the thalamus,[96,97] where information is upsampled by 20,000 relay neurons.[98] Recently, Ocko et al.[10] trained a convolutional autoencoder with pink $(1/f)$ noise, mimicking the distribution of spatial frequencies in natural scenes,[51] and obtained spatial filters that resembled center-surround RFs of a subset of primate RGC types. We used a similar CAE architecture trained with

natural UV-green images, which learned not only spatial filters resembling diverse RGC RFs but also color opponency. While approaches based on PCA and ZCA whitening also revealed color-opponency and center-surround structure (ZCA), the CAE was unique in the diversity of resulting spatial filters reminiscent of different RGC types.

In the future, it would be informative to further investigate which method for limiting the encoding capacity of the latent representation ("bottleneck") best mimics the specific constraints represented by bottlenecks in the early visual system (and why). A further decisive step would be to systematically manipulate the input images, as we have started here with respect to spatial scale, to obtain insights into which features give rise to color opponency.[99] Finally, it would be interesting to explore whether the kernels learned by the CAE indeed help predicting RGC responses to natural or synthetic stimuli.

STAR★METHODS

Detailed methods are provided in the online version of this paper and include the following:

- KEY RESOURCES TABLE
- RESOURCE AVAILABILITY
  - Lead contact
  - Materials availability
  - Data and code availability
- METHOD DETAILS
  - Camera design
  - Movie recordings
  - Temporal alignment
  - Spatial alignment
  - Spectral calibration
  - Relating camera readings to photoisomerization rates in mouse photoreceptors
- QUANTIFICATION AND STATISTICAL ANALYSIS
  - Statistical analysis of the natural scenes
  - Root mean square (RMS) contrast
  - On-Off contrast
  - On-Off preference for retinal ganglion cells (On-Off index)
  - Comparing contrast distributions
  - PCA and ZCA whitening
  - Convolutional autoencoder model

SUPPLEMENTAL INFORMATION

Supplemental information can be found online at https://doi.org/10.1016/j.cub.2021.05.017.

ACKNOWLEDGMENTS

We thank Tom Baden, Heiko Schütt, and Matthias Bethge for helpful discussions and Gordon Eske for excellent technical assistance. This work was supported by the German Research Foundation (DFG) through Collaborative Research Centre CRC 1233 (project number 276693517; sub project 10), the European Union's Horizon 2020 research and innovation programme under the Marie Skłodowska-Curie grant (agreement no. 674901), the Max Planck Society (M.FE.A.KYBE0004), and the German Ministry of Research and Education (01GQ1002). The funders had no role in study design, data collection and analysis, decision to publish, or preparation of the manuscript.

AUTHOR CONTRIBUTIONS

Conceptualization of ideas, F.S., K.R., L.B., and T.E.; methodology, Y.Q., Z.Z., L.B., and T.E., with input from D.K. and M.K.; formal analysis, Y.Q., with input from D.K., L.B., and T.E.; investigation, Y.Q., Z.Z., and K.P.S., with input from K.F., L.B., and T.E.; writing – original draft, Y.Q., L.B., and T.E.; writing – review & editing and preparation, Y.Q., Z.Z., D.K., K.P.S., M.K., K.F., L.B., and T.E.; visualization, Y.Q. and T.E.; supervision, L.B. and T.E.; funding acquisition, L.B., F.S., K.R., K.F., and T.E.

DECLARATION OF INTERESTS

The authors declare no competing interests.

Received: January 10, 2021
Revised: April 6, 2021
Accepted: May 11, 2021
Published: June 8, 2021

REFERENCES

1. Baden, T., Euler, T., and Berens, P. (2020). Understanding the retinal basis of vision across species. Nat. Rev. Neurosci. *21*, 5–20.
2. Attneave, F. (1954). Some informational aspects of visual perception. Psychol. Rev. *61*, 183–193.
3. Barlow, H.B. (1961). Possible principles underlying the transformations of sensory messages. In Sensory Communication, W.A. Rosenblith, ed. (MIT), pp. 216–234.
4. Simoncelli, E.P., and Olshausen, B.A. (2001). Natural image statistics and neural representation. Annu. Rev. Neurosci. *24*, 1193–1216.
5. Warrant, E., Johnsen, S., and Nilsson, D.-E. (2020). Light and Visual Environments. The Senses: A Comprehensive Reference, B. Fritzsch, ed. (Elsevier), pp. 4–30.
6. Turner, M.H., Sanchez Giraldo, L.G., Schwartz, O., and Rieke, F. (2019). Stimulus- and goal-oriented frameworks for understanding natural vision. Nat. Neurosci. *22*, 15–24.
7. Olshausen, B.A., and Field, D.J. (1996). Emergence of simple-cell receptive field properties by learning a sparse code for natural images. Nature *381*, 607–609.
8. Ballard, D.H. (1987). Modular learning in neural networks. In AAAI-87 Proceedings (AAAI), pp. 279–284.
9. Hinton, G.E., and Salakhutdinov, R.R. (2006). Reducing the dimensionality of data with neural networks. Science *313*, 504–507.
10. Ocko, S., Lindsey, J., Ganguli, S., and Deny, S. (2018). The emergence of multiple retinal cell types through efficient coding of natural movies. In Advances in Neural Information Processing Systems 31, S. Bengio, H. Wallach, H. Larochelle, K. Grauman, N. Cesa-Bianchi, and R. Garnett, eds. (Curran Associates), pp. 9389–9400.
11. Masland, R.H., and Martin, P.R. (2007). The unsolved mystery of vision. Curr. Biol. *17*, R577–R582.
12. Krakauer, J.W., Ghazanfar, A.A., Gomez-Marin, A., MacIver, M.A., and Poeppel, D. (2017). Neuroscience needs behavior: correcting a reductionist bias. Neuron *93*, 480–490.
13. Datta, S.R., Anderson, D.J., Branson, K., Perona, P., and Leifer, A. (2019). Computational neuroethology: a call to action. Neuron *104*, 11–24.
14. Hasson, U., Nastase, S.A., and Goldstein, A. (2020). Direct fit to nature: an evolutionary perspective on biological and artificial neural networks. Neuron *105*, 416–434.
15. Huberman, A.D., and Niell, C.M. (2011). What can mice tell us about how vision works? Trends Neurosci. *34*, 464–473.
16. Seabrook, T.A., Burbridge, T.J., Crair, M.C., and Huberman, A.D. (2017). Architecture, function, and assembly of the mouse visual system. Annu. Rev. Neurosci. *40*, 499–538.

17. Dyballa, L., Hoseini, M.S., Dadarlat, M.C., Zucker, S.W., and Stryker, M.P. (2018). Flow stimuli reveal ecologically appropriate responses in mouse visual cortex. Proc. Natl. Acad. Sci. USA *115*, 11304–11309.
18. Hoy, J.L., Yavorska, I., Wehr, M., and Niell, C.M. (2016). Vision drives accurate approach behavior during prey capture in laboratory mice. Curr. Biol. *26*, 3046–3052.
19. Jacobs, G.H., Williams, G.A., and Fenwick, J.A. (2004). Influence of cone pigment coexpression on spectral sensitivity and color vision in the mouse. Vision Res. *44*, 1615–1622.
20. Röhlich, P., van Veen, T., and Szél, A. (1994). Two different visual pigments in one retinal cone cell. Neuron *13*, 1159–1166.
21. Applebury, M.L., Antoch, M.P., Baxter, L.C., Chun, L.L., Falk, J.D., Farhangfar, F., Kage, K., Krzystolik, M.G., Lyass, L.A., and Robbins, J.T. (2000). The murine cone photoreceptor: a single cone type expresses both S and M opsins with retinal spatial patterning. Neuron *27*, 513–523.
22. Baden, T., Schubert, T., Chang, L., Wei, T., Zaichuk, M., Wissinger, B., and Euler, T. (2013). A tale of two retinal domains: near-optimal sampling of achromatic contrasts in natural scenes through asymmetric photoreceptor distribution. Neuron *80*, 1206–1217.
23. Nadal-Nicolás, F.M., Kunze, V.P., Ball, J.M., Peng, B.T., Krishnan, A., Zhou, G., Dong, L., and Li, W. (2020). True S-cones are concentrated in the ventral mouse retina and wired for color detection in the upper visual field. eLife *9*, e56840.
24. Wallace, D.J., Greenberg, D.S., Sawinski, J., Rulla, S., Notaro, G., and Kerr, J.N.D. (2013). Rats maintain an overhead binocular field at the expense of constant fusion. Nature *498*, 65–69.
25. Zhang, Y., Kim, I.-J., Sanes, J.R., and Meister, M. (2012). The most numerous ganglion cell type of the mouse retina is a selective feature detector. Proc. Natl. Acad. Sci. USA *109*, E2391–E2398.
26. Shang, C., Liu, A., Li, D., Xie, Z., Chen, Z., Huang, M., Li, Y., Wang, Y., Shen, W.L., and Cao, P. (2019). A subcortical excitatory circuit for sensory-triggered predatory hunting in mice. Nat. Neurosci. *22*, 909–920.
27. Hoy, J.L., Bishop, H.I., and Niell, C.M. (2019). Defined cell types in superior colliculus make distinct contributions to prey capture behavior in the mouse. Curr. Biol. *29*, 4130–4138.e5.
28. Szatko, K.P., Korympidou, M.M., Ran, Y., Berens, P., Dalkara, D., Schubert, T., Euler, T., and Franke, K. (2020). Neural circuits in the mouse retina support color vision in the upper visual field. Nat. Commun. *11*, 3481.
29. Denman, D.J., Luviano, J.A., Ollerenshaw, D.R., Cross, S., Williams, D., Buice, M.A., Olsen, S.R., and Reid, R.C. (2018). Mouse color and wavelength-specific luminance contrast sensitivity are non-uniform across visual space. eLife *7*, e31209.
30. Sterratt, D.C., Lyngholm, D., Willshaw, D.J., and Thompson, I.D. (2013). Standard anatomical and visual space for the mouse retina: computational reconstruction and transformation of flattened retinae with the Retistruct package. PLoS Comput. Biol. *9*, e1002921.
31. Franke, K., Maia Chagas, A., Zhao, Z., Zimmermann, M.J.Y., Bartel, P., Qiu, Y., Szatko, K.P., Baden, T., and Euler, T. (2019). An arbitrary-spectrum spatial visual stimulator for vision research. eLife *8*, e48779.
32. Meyer, A.F., Poort, J., O'Keefe, J., Sahani, M., and Linden, J.F. (2018). A head-mounted camera system integrates detailed behavioral monitoring with multichannel electrophysiology in freely moving mice. Neuron *100*, 46–60.e7.
33. Meyer, A.F., O'Keefe, J., and Poort, J. (2020). Two distinct types of eye-head coupling in freely moving mice. Curr. Biol. *30*, 2116–2130.e6.
34. Land, M. (2019). Eye movements in man and other animals. Vision Res. *162*, 1–7.
35. Michaiel, A.M., Abe, E.T.T., and Niell, C.M. (2020). Dynamics of gaze control during prey capture in freely moving mice. eLife *9*, e57458.
36. Zahler, S.H., Taylor, D.E., Adams, J.M., and Feinberg, E.H. (2021). Mice make targeted saccades. bioRxiv. https://doi.org/10.1101/2021.02.10.430669.
37. Jacobs, G.H., Williams, G.A., Cahill, H., and Nathans, J. (2007). Emergence of novel color vision in mice engineered to express a human cone photopigment. Science *315*, 1723–1725.
38. Wilkes, T.C., McGonigle, A.J.S., Pering, T.D., Taggart, A.J., White, B.S., Bryant, R.G., and Willmott, J.R. (2016). Ultraviolet imaging with low cost smartphone sensors: development and application of a Raspberry Pi-based UV camera. Sensors (Basel) *16*, 1649.
39. Ratliff, C.P., Borghuis, B.G., Kao, Y.-H., Sterling, P., and Balasubramanian, V. (2010). Retina is structured to process an excess of darkness in natural scenes. Proc. Natl. Acad. Sci. USA *107*, 17368–17373.
40. Buchsbaum, G., and Gottschalk, A. (1983). Trichromacy, opponent colours coding and optimum colour information transmission in the retina. Proc. R. Soc. Lond. B Biol. Sci. *220*, 89–113.
41. Stabio, M.E., Sondereker, K.B., Haghgou, S.D., Day, B.L., Chidsey, B., Sabbah, S., and Renna, J.M. (2018). A novel map of the mouse eye for orienting retinal topography in anatomical space. J. Comp. Neurol. *526*, 1749–1759.
42. Joesch, M., and Meister, M. (2016). A neuronal circuit for colour vision based on rod-cone opponency. Nature *532*, 236–239.
43. Mante, V., Frazor, R.A., Bonin, V., Geisler, W.S., and Carandini, M. (2005). Independence of luminance and contrast in natural scenes and in the early visual system. Nat. Neurosci. *8*, 1690–1697.
44. Frazor, R.A., and Geisler, W.S. (2006). Local luminance and contrast in natural images. Vision Res. *46*, 1585–1598.
45. Rieke, F., and Rudd, M.E. (2009). The challenges natural images pose for visual adaptation. Neuron *64*, 605–616.
46. Bex, P.J., and Makous, W. (2002). Spatial frequency, phase, and the contrast of natural images. J. Opt. Soc. Am. A Opt. Image Sci. Vis. *19*, 1096–1106.
47. Jacoby, J., and Schwartz, G.W. (2017). Three small-receptive-field ganglion cells in the mouse retina are distinctly tuned to size, speed, and object motion. J. Neurosci. *37*, 610–625.
48. Rousso, D.L., Qiao, M., Kagan, R.D., Yamagata, M., Palmiter, R.D., and Sanes, J.R. (2016). Two pairs of ON and OFF retinal ganglion cells are defined by intersectional patterns of transcription factor expression. Cell Rep. *15*, 1930–1944.
49. Bleckert, A., Schwartz, G.W., Turner, M.H., Rieke, F., and Wong, R.O.L. (2014). Visual space is represented by nonmatching topographies of distinct mouse retinal ganglion cell types. Curr. Biol. *24*, 310–315.
50. Burton, G.J., and Moorhead, I.R. (1987). Color and spatial structure in natural scenes. Appl. Opt. *26*, 157–170.
51. Field, D.J. (1987). Relations between the statistics of natural images and the response properties of cortical cells. J. Opt. Soc. Am. A *4*, 2379–2394.
52. Ruderman, D.L., and Bialek, W. (1994). Statistics of natural images: scaling in the woods. Phys. Rev. Lett. *73*, 814–817.
53. Xing, D., Yeh, C.-I., and Shapley, R.M. (2010). Generation of black-dominant responses in V1 cortex. J. Neurosci. *30*, 13504–13512.
54. Wang, Y., Jin, J., Kremkow, J., Lashgari, R., Komban, S.J., and Alonso, J.M. (2015). Columnar organization of spatial phase in visual cortex. Nat. Neurosci. *18*, 97–103.
55. Baden, T., Berens, P., Franke, K., Román Rosón, M., Bethge, M., and Euler, T. (2016). The functional diversity of retinal ganglion cells in the mouse. Nature *529*, 345–350.
56. Hut, R.A., Pilorz, V., Boerema, A.S., Strijkstra, A.M., and Daan, S. (2011). Working for food shifts nocturnal mouse activity into the day. PLoS ONE *6*, e17527.
57. Hut, R.A., Scheper, A., and Daan, S. (2000). Can the circadian system of a diurnal and a nocturnal rodent entrain to ultraviolet light? J. Comp. Physiol. A Neuroethol. Sens. Neural Behav. Physiol. *186*, 707–715.
58. Johnsen, S., Kelber, A., Warrant, E., Sweeney, A.M., Widder, E.A., Lee, R.L., Jr., and Hernández-Andrés, J. (2006). Crepuscular and nocturnal

illumination and its effects on color perception by the nocturnal hawkmoth Deilephila elpenor. J. Exp. Biol. *209*, 789–800.

59. Van Essen, D., Olshausen, B.A., Anderson, C.H., and Gallant, J.T.L. (1991). Pattern recognition, attention, and information bottlenecks in the primate visual system. In Visual Information Processing: From Neurons to Chips (International Society for Optics and Photonics), pp. 17–28.
60. Gjorgjieva, J., Sompolinsky, H., and Meister, M. (2014). Benefits of pathway splitting in sensory coding. J. Neurosci. *34*, 12127–12144.
61. Perge, J.A., Koch, K., Miller, R., Sterling, P., and Balasubramanian, V. (2009). How the optic nerve allocates space, energy capacity, and information. J. Neurosci. *29*, 7917–7928.
62. Wang, Z., Bovik, A.C., Sheikh, H.R., and Simoncelli, E.P. (2004). Image quality assessment: from error visibility to structural similarity. IEEE Trans. Image Process. *13*, 600–612.
63. Bell, A.J., and Sejnowski, T.J. (1997). The "independent components" of natural scenes are edge filters. Vision Res. *37*, 3327–3338.
64. Graham, D.J., Chandler, D.M., and Field, D.J. (2006). Can the theory of "whitening" explain the center-surround properties of retinal ganglion cell receptive fields? Vision Res. *46*, 2901–2913.
65. Nevala, N.E., and Baden, T. (2019). A low-cost hyperspectral scanner for natural imaging and the study of animal colour vision above and under water. Sci. Rep. *9*, 10799.
66. Tedore, C., and Nilsson, D.-E. (2019). Avian UV vision enhances leaf surface contrasts in forest environments. Nat. Commun. *10*, 238.
67. Rust, N.C., and Movshon, J.A. (2005). In praise of artifice. Nat. Neurosci. *8*, 1647–1650.
68. Froudarakis, E., Cohen, U., Diamantaki, M., and Walker, E.Y. (2020). Object manifold geometry across the mouse cortical visual hierarchy. bioRxiv. https://doi.org/10.1101/2020.08.20.258798.
69. Zoccolan, D., Oertelt, N., DiCarlo, J.J., and Cox, D.D. (2009). A rodent model for the study of invariant visual object recognition. Proc. Natl. Acad. Sci. USA *106*, 8748–8753.
70. Baddeley, R., Abbott, L.F., Booth, M.C., Sengpiel, F., Freeman, T., Wakeman, E.A., and Rolls, E.T. (1997). Responses of neurons in primary and inferior temporal visual cortices to natural scenes. Proc. Biol. Sci. *264*, 1775–1783.
71. Betsch, B.Y., Einhäuser, W., Körding, K.P., and König, P. (2004). The world from a cat's perspective–statistics of natural videos. Biol. Cybern. *90*, 41–50.
72. Froudarakis, E., Berens, P., Ecker, A.S., Cotton, R.J., Sinz, F.H., Yatsenko, D., Saggau, P., Bethge, M., and Tolias, A.S. (2014). Population code in mouse V1 facilitates readout of natural scenes through increased sparseness. Nat. Neurosci. *17*, 851–857.
73. Szél, A., Röhlich, P., Caffé, A.R., Juliusson, B., Aguirre, G., and Van Veen, T. (1992). Unique topographic separation of two spectral classes of cones in the mouse retina. J. Comp. Neurol. *325*, 327–342.
74. Peichl, L. (2005). Diversity of mammalian photoreceptor properties: adaptations to habitat and lifestyle? Anat. Rec. A Discov. Mol. Cell. Evol. Biol. *287*, 1001–1012.
75. Chang, L., Breuninger, T., and Euler, T. (2013). Chromatic coding from cone-type unselective circuits in the mouse retina. Neuron *77*, 559–571.
76. Tikidji-Hamburyan, A., Reinhard, K., Storchi, R., Dietter, J., Seitter, H., Davis, K.E., Idrees, S., Mutter, M., Walmsley, L., Bedford, R.A., et al. (2017). Rods progressively escape saturation to drive visual responses in daylight conditions. Nat. Commun. *8*, 1813.
77. Rhim, I., Coello-Reyes, G., and Nauhaus, I. (2020). Variations in photoreceptor throughput to mouse visual cortex and the unique effects on tuning. bioRxiv. https://doi.org/10.1101/2020.11.03.366682.
78. Szél, A., Csorba, G., Caffé, A.R., Szél, G., Röhlich, P., and van Veen, T. (1994). Different patterns of retinal cone topography in two genera of rodents, Mus and Apodemus. Cell Tissue Res. *276*, 143–150.
79. Zimmermann, M.J.Y., Nevala, N.E., Yoshimatsu, T., Osorio, D., Nilsson, D.-E., Berens, P., and Baden, T. (2018). Zebrafish differentially process color across visual space to match natural scenes. Curr. Biol. *28*, 2018–2032.e5.
80. Wilson, M. (1978). The functional organisation of locust ocelli. J. Comp. Physiol. *124*, 297–316.
81. Khani, M.H., and Gollisch, T. (2021). Linear and nonlinear chromatic integration in the mouse retina. Nat. Commun. *12*, 1900.
82. Cronin, T.W., and Bok, M.J. (2016). Photoreception and vision in the ultraviolet. J. Exp. Biol. *219*, 2790–2801.
83. Chávez, A.E., Bozinovic, F., Peichl, L., and Palacios, A.G. (2003). Retinal spectral sensitivity, fur coloration, and urine reflectance in the genus octodon (rodentia): implications for visual ecology. Invest. Ophthalmol. Vis. Sci. *44*, 2290–2296.
84. Altshuler, D.L. (2001). Ultraviolet reflectance in fruits, ambient light composition and fruit removal in a tropical forest. Evol. Ecol. Res. *3*, 767–778.
85. Naarendorp, F., Esdaille, T.M., Banden, S.M., Andrews-Labenski, J., Gross, O.P., and Pugh, E.N., Jr. (2010). Dark light, rod saturation, and the absolute and incremental sensitivity of mouse cone vision. J. Neurosci. *30*, 12495–12507.
86. Govardovskii, V.I., Fyhrquist, N., Reuter, T., Kuzmin, D.G., and Donner, K. (2000). In search of the visual pigment template. Vis. Neurosci. *17*, 509–528.
87. Cooper, E.A., and Norcia, A.M. (2015). Predicting cortical dark/bright asymmetries from natural image statistics and early visual transforms. PLoS Comput. Biol. *11*, e1004268.
88. Yeh, C.-I., Xing, D., and Shapley, R.M. (2009). "Black" responses dominate macaque primary visual cortex v1. J. Neurosci. *29*, 11753–11760.
89. Kremkow, J., Jin, J., Wang, Y., and Alonso, J.M. (2016). Principles underlying sensory map topography in primary visual cortex. Nature *533*, 52–57.
90. Schröder, S., Steinmetz, N.A., Krumin, M., Pachitariu, M., Rizzi, M., Lagnado, L., Harris, K.D., and Carandini, M. (2020). Arousal modulates retinal output. Neuron *107*, 487–495.e9.
91. Mazade, R., Jin, J., Pons, C., and Alonso, J.-M. (2019). Functional specialization of ON and OFF cortical pathways for global-slow and local-fast vision. Cell Rep. *27*, 2881–2894.e5.
92. Münch, T.A., da Silveira, R.A., Siegert, S., Viney, T.J., Awatramani, G.B., and Roska, B. (2009). Approach sensitivity in the retina processed by a multifunctional neural circuit. Nat. Neurosci. *12*, 1308–1316.
93. Kim, T., Shen, N., Hsiang, J.-C., Johnson, K.P., and Kerschensteiner, D. (2020). Dendritic and parallel processing of visual threats in the retina control defensive responses. Sci. Adv. *6*, eabc9920.
94. Kramer, M.A. (1991). Nonlinear principal component analysis using autoassociative neural networks. AIChE J. *37*, 233–243.
95. Jeon, C.J., Strettoi, E., and Masland, R.H. (1998). The major cell populations of the mouse retina. J. Neurosci. *18*, 8936–8946.
96. Ellis, E.M., Gauvain, G., Sivyer, B., and Murphy, G.J. (2016). Shared and distinct retinal input to the mouse superior colliculus and dorsal lateral geniculate nucleus. J. Neurophysiol. *116*, 602–610.
97. Guido, W. (2018). Development, form, and function of the mouse visual thalamus. J. Neurophysiol. *120*, 211–225.
98. Evangelio, M., García-Amado, M., and Clascá, F. (2018). Thalamocortical projection neuron and interneuron numbers in the visual thalamic nuclei of the adult C57BL/6 mouse. Front. Neuroanat. *12*, 27.
99. Chalk, M., Marre, O., and Tkačik, G. (2018). Toward a unified theory of efficient, predictive, and sparse coding. Proc. Natl. Acad. Sci. USA *115*, 186–191.
100. Oommen, B.S., and Stahl, J.S. (2008). Eye orientation during static tilts and its relationship to spontaneous head pitch in the laboratory mouse. Brain Res. *1193*, 57–66.

101. Lowe, D.G. (2004). Distinctive image features from scale-invariant keypoints. Int. J. Comput. Vis. *60*, 91–110.

102. Fischler, M.A., and Bolles, R.C. (1981). Random sample consensus: a paradigm for model fitting with applications to image analysis and automated cartography. Commun. ACM *24*, 381–395.

103. Poynton, C. (2003). Digital Video and HD: Algorithms and Interfaces (Morgan Kaufmann).

104. Henriksson, J.T., Bergmanson, J.P.G., and Walsh, J.E. (2010). Ultraviolet radiation transmittance of the mouse eye and its individual media components. Exp. Eye Res. *90*, 382–387.

105. Nikonov, S.S., Kholodenko, R., Lem, J., and Pugh, E.N., Jr. (2006). Physiological features of the S- and M-cone photoreceptors of wild-type mice from single-cell recordings. J. Gen. Physiol. *127*, 359–374.

106. Simonyan, K., and Zisserman, A. (2014). Very deep convolutional networks for large-scale image recognition. arXiv, arXiv:1409.1556v6. https://arxiv.org/abs/1409.1556.

107. Paszke, A., Gross, S., Massa, F., Lerer, A., Bradbury, J., Chanan, G., Killeen, T., Lin, Z., Gimelshein, N., Antiga, L., et al. (2019). PyTorch: an imperative style, high-performance deep learning library. In Advances in Neural Information Processing Systems 32, H. Wallach, H. Larochelle, A. Beygelzimer, F. Alché-Buc, E. Fox, and R. Garnett, eds. (Curran Associates), pp. 8026–8037.

108. van Rossum, M.C.W., O'Brien, B.J., and Smith, R.G. (2003). Effects of noise on the spike timing precision of retinal ganglion cells. J. Neurophysiol. *89*, 2406–2419.

109. Doi, E., and Lewicki, M.S. (2007). A theory of retinal population coding. In Advances in Neural Information Processing Systems 19, B. Schölkopf, J.C. Platt, and T. Hoffman, eds. (MIT), pp. 353–360.

110. Field, D.J. (1994). What is the goal of sensory coding? Neural Comput. *6*, 559–601.

111. Hubel, D.H., and Wiesel, T.N. (1959). Receptive fields of single neurones in the cat's striate cortex. J. Physiol. *148*, 574–591.

112. Marr, D., and Hildreth, E. (1980). Theory of edge detection. Proc. R. Soc. Lond. B Biol. Sci. *207*, 187–217.

113. Vincent, B.T., and Baddeley, R.J. (2003). Synaptic energy efficiency in retinal processing. Vision Res. *43*, 1283–1290.

114. Kingma, D.P., and Ba, J. (2014). Adam: a method for stochastic optimization. arXiv, arXiv:1412.6980v9. https://arxiv.org/abs/1412.6980.

STAR★METHODS

KEY RESOURCES TABLE

REAGENT or RESOURCE	SOURCE	IDENTIFIER
Deposited data		
Jupyter notebooks and scripts for analysis	This paper	https://github.com/eulerlab/mouse-scene-cam/
Movies and data	This paper	https://doi.org/10.5281/zenodo.4812404
Software and algorithms		
Python 3.6	N/A	https://www.python.org/
OpenCV Framework for computer vision	N/A	https://opencv.org/
Pytorch Machine learning library	N/A	https://pytorch.org/
FreeCAD Open source 3D construction software	N/A	https://www.freecadweb.org/
VNC Viewer Screen-sharing and remote-control	RealVNC, UK	http://www.realvnc.com/en
Other		
UV-enabled spectrometer	Ocean Optics, Germany	STS-UV, https://www.oceaninsight.com/products/spectrometers/microspectrometer/sts-series/sts-uv/
Power meter	Newport, Germany	842-PE, https://www.newport.com/n/newport-power-meter-and-detector-legacy-and-compatibility
360 nm LED	Roithner, Austria	XSL-360-5E
380 nm LED	Roithner, Austria	VL380-5-15
400 nm LED	Roithner, Austria	XRL-400-5E
490 nm LED	Roithner, Austria	LED490-06
525 nm LED	Roithner, Austria	G58A5111P
Spectral sensitivity of Raspberry Pi camera (Depending on the camera version, different chips are used)	Raspberry Pi Foundation, UK	https://www.raspberrypi.org/documentation/hardware/camera/
Gimbal	Zhiyun, China	Crane 2 (1x)
Dichroic Mirror (DM)	AHF, Germany	F48-442 (1x)
“Green” Pass Filter (GPF)	AHF, Germany	F47-510 (1x)
UV Pass Filter	AHF, Germany	F37-424 (1x)
Raspberry PI Zero W	Raspberry Pi Foundation, UK	e.g. EXP-R12-143 (2x), EXP-TECH, Germany
Zero spy camera	Raspberry Pi Foundation, UK	e.g. EXP-R15-1309 (2x), EXP-TECH, Germany
Powerbank	Anker Technology, UK	e.g. ANKER 1252011 (1x), Reichelt, Germany
Fisheye lens	N/A	LS-40180 (1x), e.g., Watterott, Germany
Bi-Convex lens, L04, f = 35 mm	Thorlabs, Germany	LB4879-A (1x)
Bi-Convex lens, L05, f = 20 mm	Thorlabs, Germany	LB4854-A (1x)
Plano convex lens, L03, f = 150 mm	Thorlabs, Germany	LA4874-A (1x)
Plano convex lens, L01/02, f = 50 mm	Thorlabs, Germany	LA4148-A (2x)
Iris diaphragm, P1, 2	Thorlabs, Germany	SM1D12C (2x)
Protected silver mirror	Thorlabs, Germany	PF10-03-P01 (1x)
Kinematic mirror mount	Thorlabs, Germany	KCB1/M (1x)
Generic 3.3V green LEDs for camera synchronization	Conrad, Germany	(2x)
Cage Cube	Thorlabs, Germany	CM1-DCH/M (1x)
Slip Plate Positioner	Thorlabs, Germany	SPT1/M (1x)
Cage Plate	Thorlabs, Germany	CP02T/M (1x)
Cage Plate	Thorlabs, Germany	CP02/M (8x)

RESOURCE AVAILABILITY

Lead contact

Further information and requests for resources and reagents should be directed to and will be fulfilled by the Lead Contact, Thomas Euler (thomas.euler@cin.uni-tuebingen.de).

Materials availability

The mouse camera footage recorded in this study is publicly available (for link to repository, see Key resources table).

Data and code availability

Data analysis was performed using Python. Relevant custom-written Python scripts and Jupyter notebooks are available (see https://github.com/eulerlab/mouse-scene-cam/). Original data have been deposited to Zenodo: [10.5281/zenodo.4812404].

METHOD DETAILS

Camera design

As the front lens of our camera (Figure 1A), we used a fisheye lens ($f = 1.05\,mm$, $f/2$, LS-40180, Watterott, Germany) with a FOV of approx. 180°. Following an inverted periscope design, the lens was mounted at the bottom end of the camera, which allowed us to capture the scene from a distance of approx. 2-5 cm to the ground (Figures 1B–1F). After passing two relay lenses (L04, LB4879-A, $f = 35\,mm$; L05, LB4854-A, $f = 20\,mm$; both Thorlabs, German), which allowed us to transfer the fisheye lens' FOV to the camera sensor, a silver mirror reflected the light toward a dichroic mirror (F48-442, AHF, Germany; reflection, >90%, 350–442 nm; transmission, >90%, 460–650 nm; Figure 1C) that reflected wavelengths shorter than approx. 440 nm toward the first camera sensor (CS1) and transmitted longer wavelengths toward the second camera sensor (CS2; Figure 1A). An additional spectral bandpass filter in front of each camera chip (BP_G, F47-510, >90%, 470–550 nm; BP_{UV}, F37-424, >90%, 350–419 nm; both AHF) restricted the light reaching the chips to the approx. spectral ranges relevant for mouse opsins (Figure 1C). Because the spectral properties of dichroic filters (DM, BP_{UV}, BP_G) change with the incident angle of the light, we used relay lenses L1, L2 (LA4148-A, $f = 50\,mm$; Thorlabs, Germany) and L3 (LA4874-A, $f = 150\,mm$; Thorlabs) to ensure that light passes the dichroic bandpass filters collimated before being focused onto the camera chips. In addition, we added iris diaphragms (SM1D12C; adjusted to ~2 mm pinhole diameter) directly in front of the cameras to optimize depth-of-field and image contrast. For the parts list, including mechanical parts, see Key resources table.

For each chromatic channel, we used a Zero spy camera module (EXP-R15-1309, EXP-TECH, Germany) connected to separate Raspberry Pi Zero W single-board computers (EXP-R12-143, EXP-TECH), which were powered by a 15 Ah USB power bank (Anker 1252011, Reichelt, Germany). Lenses and infrared filters had been removed from the camera modules. To increase the UV sensitivity of the chip in the UV pathways, we mechanically removed its RGB Bayer layer, following a procedure described by Wilkers et al.[38]

Movie recordings

Movies were recorded onto the Raspberry Pi's Flash memory card; movie capture was remote-controlled from a laptop connected to the Raspberry Pis either via USB cable or an *ad hoc* Wifi network (VNC Viewer, RealVNC, UK). Camera parameters were fixed for all recordings (Key resources table). To stabilize the camera during the recordings, we mounted it on a gimbal (Crane 2, Zhiyun, China; Figures 1D and 1E). Since the camera weighed around 1 kg and its point of gravity was not centered, we added counterweights for the gimbal to work properly. When moving, we tried to maintain an azimuth angle of ~ 60° between the optical axis of the fisheye lens and movement direction, close to the azimuth angle of the mouse' eye.[30,41,100] In terms of elevation, we tried to obtain footage in which the horizon bisected the camera's visual field of ~180°.

Temporal alignment

Since we recorded with two camera chips simultaneously, the resulting movies needed to be temporally and spatially (next section) synchronized. For temporal alignment, we used LEDs mounted close to each camera chip (Figure 1A) and flashed (200-ms pulses every 20 s) them as synchronization markers. In addition, we manually checked the temporal alignment by comparing frames from the two channels (e.g., during fast movements).

Spatial alignment

Because we used optical rails to build the mouse-cam's optical pathway, the UV and green channels captured almost the same scene. To account for potential spatial offsets and differences in image magnification, we used a homography matrix (H) to spatially relate a point $(x_1, y_1)^T$ in the first channel to a corresponding point $(x_2, y_2)^T$ in the other channel:

$$\begin{bmatrix} x_1 \\ y_1 \\ 1 \end{bmatrix} = H \begin{bmatrix} x_2 \\ y_2 \\ 1 \end{bmatrix}.$$

To this end, we first extracted at least 20 feature points from both channels using the scale-invariant feature transform (SIFT) approach[101] and matched these feature points using the k-nearest neighbor algorithm. Next, H was determined by a random sample consensus algorithm,[102] allowing us to project all pixels in the first channel (green) to those in the second channel (UV), with the same H typically working for all frames of a particular recording.

Spectral calibration

Since we did not know the camera chip's exact sensitivity curve, we measured the sensitivity of the two camera channels using LEDs of defined spectrum and power. Specifically, to map image pixel values (v_{Raw}, 0...255) to absolute intensities (in $[\mu W]$), we first intensity-calibrated LEDs peaking in the UV (λ_{Peak} = 360, 380, 400 nm; see Key resources table; Figure S1A) or the green band (λ_{Peak} = 490, 525 nm) using a power meter (842-PE, Newport, Germany). Next we recorded images of these LEDs set to different intensities to determine the relationship between normalized pixel value (v, 0...1) and power (P) by fitting the data to $P = av^b + c$ (Figure S1B; for coefficients, see Table 1) using the Levenberg-Marquardt algorithm for least-squares curve fitting. We then used these fits to convert pixel values into normalized intensities (source versus intensity-corrected images; Figure S1C).

To verify this intensity correction, we acquired ground-truth spectral images of the outside natural scenes with a scanning spectrometer, as described earlier.[22] In brief, this custom-built device consisted of two servo motors that moved the fiber of a USB-spectrometer (STS-UV, Ocean Optics, Germany) to rasterize the scene with a resolution of ~10° of visual angle, yielding for each pixel the spectrum from 300 to 660 nm, which was convolved with the spectral sensitivities of mouse opsins to compute the spectrometer images (Figures S1D and S1F, right). For representative scene elements, such as grass and trees, we found that overall, the normalized intensities in the corrected camera images matched well those in the spectrometer images for both the UV and green channel (Figure S1E).

Our intensity correction reached its limit for extensive sky regions, because the camera chip has a limited dynamic range and may have saturated, when the spectrometer did not. Vice versa, at twilight, parts of the image may be underexposed. We considered these potential issues by including in our analysis only images without substantial over- or underexposure (see "Statistical analysis of the natural scenes" below).

Although in the natural environment, the absolute intensity of UV is known to be lower than that of longer wavelengths[57] (see Discussion), we decided to use the available range for both color channels by linearly mapping an intensity range of 0.02 – 0.76 μW (UV) and 0.37 – 6.56 μW (green) to pixel values between 5–255 and 14–255, respectively. For better visualization, we applied gamma correction ($v' = v^{1/\gamma}$, with $\gamma = 2.2$[103]) to the images in the figures (e.g., Figures S1C and S1D versus S1F).

Relating camera readings to photoisomerization rates in mouse photoreceptors

The spectral calibration enabled us to relate the camera output (normalized intensity) to absolute intensities (power P_{el} in $[W]$; Figure S1B). To relate P_{el} to photon flux (P_{Phi} in $[photons \cdot s^{-1}]$) at the cornea and finally photoisomerisation rate (R_{Iso} in $[R^* \cdot s^{-1}]$ per photoreceptor), we needed to consider (*i*) how much light we lose between the fisheye lens' surface and the camera chip for the UV and green channel ($\mu_{lens2cam,\,UV}$ and $\mu_{lens2cam,\,G}$, respectively); (*ii*) the wavelength-specific transmission of mouse optical apparatus (T_{UV}, T_G;);[104] and (*iii*) the ratio between pupil size and retinal area ($R_{pup2ret}$) to estimate how much light reaches the retina given that the pupil adapts to the overall brightness of the scene.

The calculation is detailed in a Jupyter notebook (for link to repository, see Key resources table). In brief, our approach consisted of two main steps:

(1) We first mapped P_{el} to P_{Phi}:

$$P_{Phi}(\lambda) = \frac{P_{el}(\lambda) \cdot a \cdot \lambda \cdot 10^{-9}}{c \cdot h} \cdot \frac{1}{\mu_{lens2cam}(\lambda)}$$

with λ the wavelength at which the opsin's spectral sensitivity curve peaks (λ_S = 360 nm, λ_M = 510 nm), a conversion factor (a = 6.2421018 eV/J), the Planck constant (h), and the speed of light (c).

(2) Next, we converted P_{Phi} to R_{Iso}:

$$R_{Iso}(\lambda) = \frac{P_{Phi}(\lambda)}{A_{Stim}} \cdot A_{Collect} \cdot S_{Act} \cdot T(\lambda) \cdot R_{pup2ret}$$

with $A_{Stim} = 10^8\ \mu m^2$, the area that is illuminated on the power meter sensor that was used to determine the attenuation in the camera, and $A_{Collect}$, the photoreceptor's outer segment (OS) light collection area,[105] for which we used 0.2 μm^2 for cones and 0.5 μm^2 for rods. With S_{Act} we took into account that the bandpass filters in the camera pathways did not perfectly match the sensitivity spectra.

QUANTIFICATION AND STATISTICAL ANALYSIS

Statistical analysis of the natural scenes

A movie frame contained a circular FOV of ~180°, corresponding to 437 pixels along the diameter. To minimize the influence of potential chromatic and spatial aberrations introduced by the fish-eye lens, we focused on image cut-outs ("crops"; $(53^\circ)^2$, equivalent to $(128\ \text{pixels})^2$ in size). These image crops were taken from the central upper and lower visual field, centered at ~53° and ~-44°, respectively, relative to the horizon. By choosing these locations we ensured that they correspond to regions that would be predominantly processed by ventral and dorsal parts of the mouse retina. Indeed, it is known that the mouse eye is tilted ~22° toward the sky,[41] such that the representation of the horizon on the retina is shifted ventrally. Focusing on image crops centered at ~-44° below the midline made it thus possible to largely avoid parts of the image that would be processed around the transition zone.

For the contrast analysis, we excluded image crops that contained more than 30% underexposed ($v_{Raw}(G) < 15, v_{Raw}(UV) < 6$) or overexposed ($v_{Raw}(G), v_{Raw}(UV) > 254$) pixels. Simulations, in which we systematically varied this intensity threshold and hence the percentage of overexposed pixels, revealed that our results were not driven by saturated pixels (data not shown). We randomly sampled one image crop every 10 frames from all movies (Figures 1B and 1E) until we had 1,500 crops for each upper and lower visual field.

Performing an analysis of contrast systematically across all recorded movies was challenging, given that the brightness of the recorded scenes could vary tremendously, e.g., depending on time of the day, the weather, and the scene content. We therefore divided the image crops into three "intensity classes" (I_{low}, I_{median}, I_{high}) using percentiles (1/3 and 2/3) of the mean intensity distribution as boundaries.

Note that scene content varied somewhat with the image group, because scenes in or near the forest were usually dimmer ("low mean") than those with open skies, bare ground and little vegetation ("high mean"). Since this bias was merely a side-effect of our mean intensity criterion, we refrained from linking statistics to scene content. In the future, it would be interesting to explore how scene content affects chromatic contrast statistics, for instance by classifying the images with pre-trained CNN models like VGG[106] before the statistical analyses. This could, for example, shed light on the question why contrast differences generally tended to decrease toward the high mean intensity group – that is, whether this is simply due to the limited dynamic range of the camera or in fact scene content-dependent. To determine C_{RMS} and C_{On-Off}, we randomly picked in each class for all images 10 locations per crop.

Root mean square (RMS) contrast

In psychophysical studies, C_{RMS} is commonly used for estimating contrast in natural scenes and defined as:

$$C_{RMS}(x,y) = \frac{\sigma(I_{Centre}(x,y))}{\mu(I_{Centre}(x,y))}$$

where $\sigma(I_{Centre}(x,y))$ and $\mu(I_{Centre}(x,y))$ are standard deviation and mean, respectively, of the normalized pixel intensities contained in an image spot ("receptive field"; RF) centered at (x,y) within the image crop. Spot diameters (d_{RF}) ranged from 2 to 14 degrees of visual angle. The results of all statistical comparisons are summarized in Tables S2 and S3.

On-Off contrast

We measured On-Off contrast (C_{On-Off}) at a point (x,y) using a difference-of-Gaussians (DOG) kernel with a normalized denominator to restrict the value range to $[-1, 1]$:

$$C_{On-Off}(x,y) = \frac{I_{Centre}(x,y) - I_{Surround}(x,y)}{I_{Centre}(x,y) + I_{Surround}(x,y)}$$

where $I_{Centre}(x,y)$ and $I_{Surround}(x,y)$ represent the summed pixel intensities after convolving the image with the center and surround Gaussian kernels, respectively. The spatial relationship between center and surround Gaussians were $\sigma_{Surround} = 1.5\sigma_{Centre}$; the total DOG kernel size was $3\sigma_{Centre}$. Note that d_{RF} was defined by the zero crossing radius of the kernel:

$$f\left(r|\mu, \sigma^2_{Centre}\right) = g\left(r|\mu, (1.5\cdot\sigma_{Centre})^2\right)$$

where $f(r|\mu, \sigma^2_{Centre})$ and $g(r|\mu, (1.5\sigma_{Centre})^2)$ are center and surround Gaussians, respectively. We ensure that the kernel response to a homogeneous input image 0 by setting $r = 1.2\sigma_{Centre}$. A negative kernel response resulted in $C_{On-Off} < 0$, indicating a negative contrast at this sample location. As for C_{RMS}, d_{RF} ranged from 2° to 14°. The results of all statistical comparisons are summarized in Tables S2 and S3.

On-Off preference for retinal ganglion cells (On-Off index)

To test if ventral mouse RGCs prefer dark contrasts, we re-evaluated a published dataset with recordings of ventral RGCs.[55] From this dataset, we extracted for all Off (groups 1-9) and On (groups 15-32) RGCs that passed the quality criterion ($Qi > 0.2$; $n = 2,380$

cells) the On-Off index (cell_oo_idx, *OOi*; see below) and the RF diameter (rf_size, in [μm]). The latter was converted from [μm] into [°] of visual angle, assuming $1^\circ \approx 30\ \mu m$ on the mouse retinal surface. The On-Off preference (OOi) of a cell and was defined as:

$$OOi = \frac{\langle r_{On} \rangle_t - \langle r_{Off} \rangle_t}{\langle r_{On} \rangle_t + \langle r_{Off} \rangle_t}$$

with r_{On} and r_{Off} defined as the activity during the response to the leading and the trailing edge of a bright-on-dark moving bar stimulus, respectively.

Note that we currently lack the corresponding data for dorsal RGCs, and therefore the question remains if the balanced contrast distribution in the lower visual field is also reflected in a more balanced distribution of On/Off preferences.

Comparing contrast distributions

To test if two contrast distributions originate from the same distribution, we performed a two-sided permutation test (distribution medians) with 10,000 repeats to estimate the p value. In addition, as a metric for similarity between the contrast distributions in the UV (P_{UV}) and the green (P_G) channel, we used Jensen-Shannon divergence (JSD):

$$JSD(P_{UV}||P_G) = \frac{D(P_{UV}||M)}{2} + \frac{D(P_G||M)}{2},$$

with the Kullback-Leibler (KL) divergence (D) defined as:

$$D(P||Q) = \sum P(x) \log\left(\frac{P(x)}{Q(x)}\right),$$

and $M = 0.5(P_{UV} + P_G)$. Instead of KL divergence, we used JSD because it is symmetric and bounded (0...1 for log base 2).

PCA and ZCA whitening

Buchsbaum and Gottschalk[40] have shown that achromatic and chromatic visual channels can be obtained using principal component analysis (PCA). As an extension, zero-phase component analysis (ZCA) whitening was shown to decorrelate signals and learned center-surround-like kernels.[63] Accordingly, we defined a covariance matrix C of the original centered data $\vec{x}$. By applying transformation matrix W, we would get uncorrelated data $\widehat{\vec{x}}$

$$\widehat{\vec{x}} = W\vec{x}$$

We performed PCA (without whitening) on the image crops using:

$$W = U^T$$

ZCA whitening was performed using:

$$W = U(D + \varepsilon)^{-\frac{1}{2}}U^T$$

where U and D contain eigenvectors and eigenvalues of C, respectively, and $\varepsilon = 10^{-8}$ for numerical stability.

We first applied PCA on intensities of chromatic channels. The eigenvector with two positive or two negative entries corresponds to an achromatic transformation and the other eigenvector with one positive and one negative entry corresponds to a chromatic (color-opponent) transformation. We also applied PCA on 9x9 image patches randomly drawn from the same set of image crops as for the CAE. We defined the color-opponent transformation when the kernels from the UV and green channels were negatively correlated (Pearson correlation coefficient, $p < 0.05$). In both cases, the color opponency index (CO_i), which represents the ratio between signal variance in the color-opponent dimensions to the variance in all dimensions, was defined as:

$$CO_i = \frac{\sum \lambda_{CO}}{\sum \lambda}$$

where λ_{CO} denotes the eigenvalues of the color-opponent transformation, and λ all eigenvalues.

With PCA, we found that crops from the upper visual field have a higher CO_i (higher variance along the color-opponent dimension) than ones from the lower visual field. Unlike the CAE, the PCA kernels did not resemble the center-surround RFs known in RGCs (Figure 6E). Also with ZCA whitening, we found more color-opponent kernels with images from the upper visual field. However, while these kernels were center-surround, they were small and mainly different in spatial position (Figure 6F).

Convolutional autoencoder model

We prepared datasets from the upper and the lower visual field separately. For both datasets, 10,000 image crops ($\vec{x_i}$ and i represents image index) were randomly picked. To keep model run time at bay, we used smaller (56x56 pixel $\approx (23^\circ)^2$ visual angle) image crops than for the statistical analysis and additionally rescaled them to 28x28 pixels (same visual angle but with $\approx 0.8^\circ$ pixels). These image crops met the same quality criteria (fewer than 30% of pixels under/over-exposure) as those for the statistical analysis. Among

them, 9,000 image crops were used for training and the rest for validation and testing. The images were offset-corrected separately in each chromatic channel (by subtracting the channel's mean intensity).

We implemented a simple convolutional autoencoder model (CAE; Figure 6A) following Ocko et al.[10] using PyTorch.[107] The encoder contained a single convolutional layer (with weights denoted $\overrightarrow{w_c}$) followed by a rectified linear unit (ReLU) function, one fully-connected (FC) layer and another ReLU function. The decoder contained one FC layer, one ReLU function, a single deconvolutional layer (with weights denoted $\overrightarrow{w_d}$), and a hyperbolic tangent (tanh) function to map back to the original data range (−1...1).

Classically, autoencoders are encouraged to learn an efficient encoding of the input in the presence of a "bottleneck" implemented by a low number of units in the hidden layer. Instead, we here implemented redundancy reduction of the input by adding Gaussian noise with $\sigma = 1$ to the encoder output,[10] and by imposing an L1 penalty (hyperparameter β) to its activations (sparse activations).[10,108–110] To encourage smooth kernels akin to those of early visual neurons (e.g., Hubel and Wiesel[111] and Marr and Hildreth[112]), we used L2 regularization (hyperparameter *a*) on the convolutional and deconvolutional layers, effectively constraining the norm of the weights.[113]

We used 16 convolutional kernels with filter sizes of 5x5 ($\approx(4.1^\circ)^2$ visual angle; $\approx$120 μm on the retina), 9x9 ($\approx(7.4^\circ)^2$; $\approx$220 μm) and 13x13 pixels ($\approx(10.7^\circ)^2$; $\approx$320 μm) for each chromatic channel, with zero-padded boundaries and without downsampling. Correspondingly, the deconvolutional kernels consisted of 5x5, 9x9, or 13x13 pixel filters per input channel. The size of the activation tensor after the first convolution was 28x28x16 (height x width x channel), which was flattened into a 12,544 dimensional vector before it was fed into the FC layer. The two FC layers had the same input and output size. The loss function was defined as:

$$L_{CAE} = \sum_i \left(\overrightarrow{x_i} - \widehat{\overrightarrow{x_i}}\right)^2 + \alpha(\|\overrightarrow{w_c}\|_2 + \|\overrightarrow{w_d}\|_2) + \beta\|\overrightarrow{h}\|_1$$

The first term is the MSE between prediction $\widehat{\overrightarrow{x_i}}$ and ground truth $\overrightarrow{x_i}$, the second term is the L2 penalty (α) on the weights of the convolutional $(\overrightarrow{w_c})$ and deconvolutional $(\overrightarrow{w_d})$ layers, and the third term is the L1 penalty (β) on the encoder output.

We trained the CAE models to minimize difference between reconstructed and original images from the upper and lower visual field (from all mean intensity groups, $I_{1\text{-}3}$; or separately for $I_{1,2}$ and I_3; Table S4) separately for different regularizations and different random initialization seeds. Specifically, the CAE models were trained for 100 epochs with 100 image crops in each mini-batch (learning rate, $\eta = 10^{-4}$) using the Adam optimizer[114] to minimize the loss functions. Image reconstruction performance of the CAE was estimated based on structural similarity (SSIM)[62] and MSE (Figures 6B and S5B, respectively).

Hyperparameters α and β were adjusted via grid search. We aimed at a trade-off between reconstruction performance ($SSIM \geq 0.6$ or $MSE \leq 0.01$) and regularizations (mitigation of overfitting), which we found for combinations of $\alpha = 10^3, 10^4$ and $\beta = 0 - 1/16$. Next, we performed a permutation test with 10,000 repeats to check if the models trained with images from the upper visual field learned color-opponent kernels more frequently than those trained with lower visual field images. We compared the number of color-opponent kernels generated under the two input conditions using a two-sided permutation test.

Current Biology, Volume *31*

Supplemental Information

Natural environment statistics in the upper and lower visual field are reflected in mouse retinal specializations

Yongrong Qiu, Zhijian Zhao, David Klindt, Magdalena Kautzky, Klaudia P. Szatko, Frank Schaeffel, Katharina Rifai, Katrin Franke, Laura Busse, and Thomas Euler

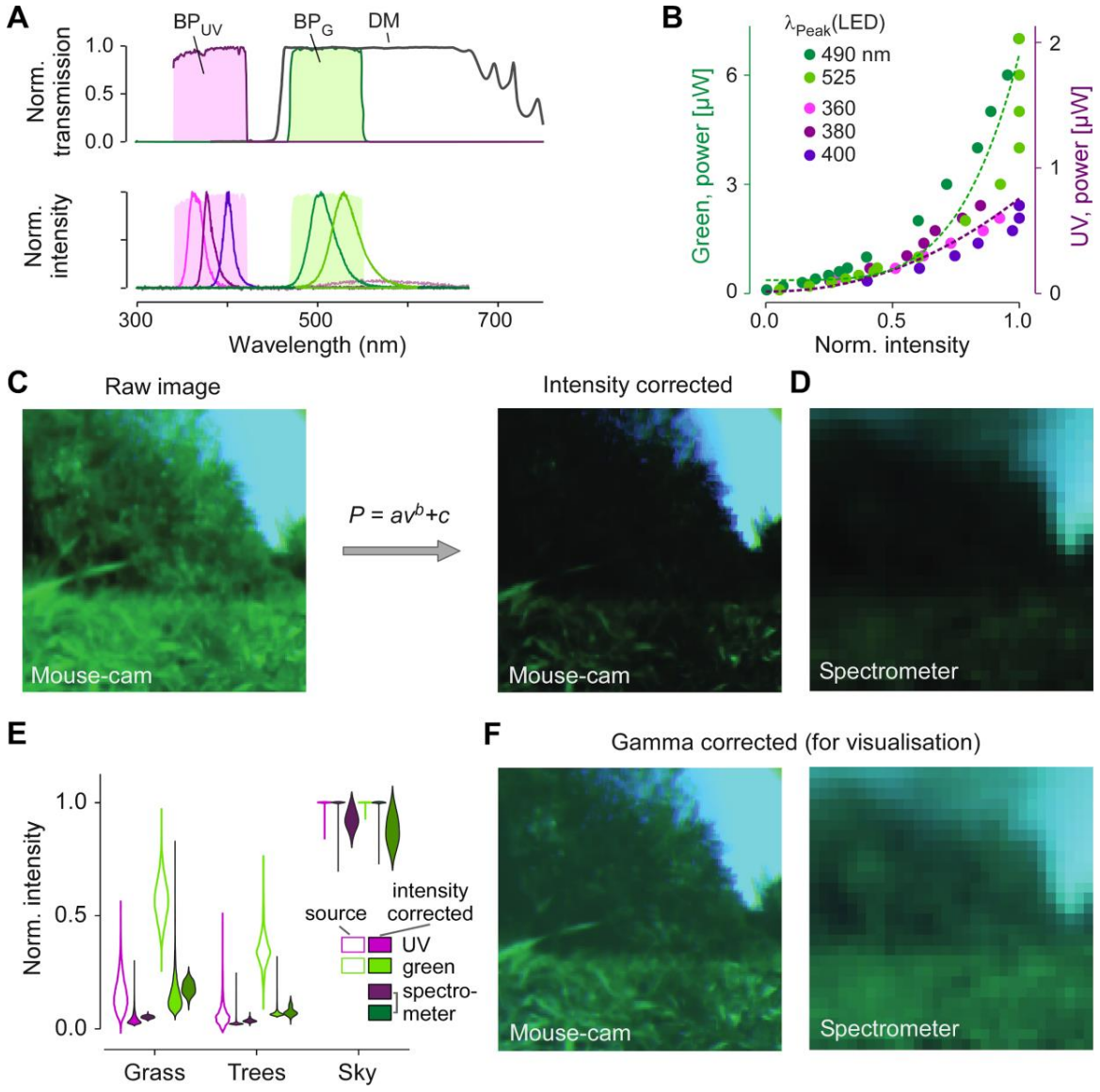

Figure S1 | **Intensity correction of the two camera channels**. **Related to Figure 1.**

A, Transmission spectra of bandpass filters in UV (BP_{UV}) and green (BP_G) channels, dichroic mirror (DM; top), and emission spectra of calibration LEDs (bottom; for peak wavelengths, see (B)), **B**, Power of LEDs (data points; measured with power meter) as function of normalised intensity reported by UV- and green-sensitive cameras (Methods). **C**, Example frame before (left; raw image) and after application of inverse-gamma curves (right; intensity-corrected) from (B). **D**, Same scene recorded with scanning spectrometer [S1]. **E**, Comparison of intensity distributions (violin plots) of scene "components" (grass, trees, sky) for spectrometer and camera data before and after calibration. Note that due to the limited dynamic range of the camera chip, saturation of pixels in the sky region cannot be completely avoided, hence the narrow distribution of the "Sky" values for the camera measurements. **F**, Images from (C, right) and (D) with gamma correction applied for visualisation (Methods).

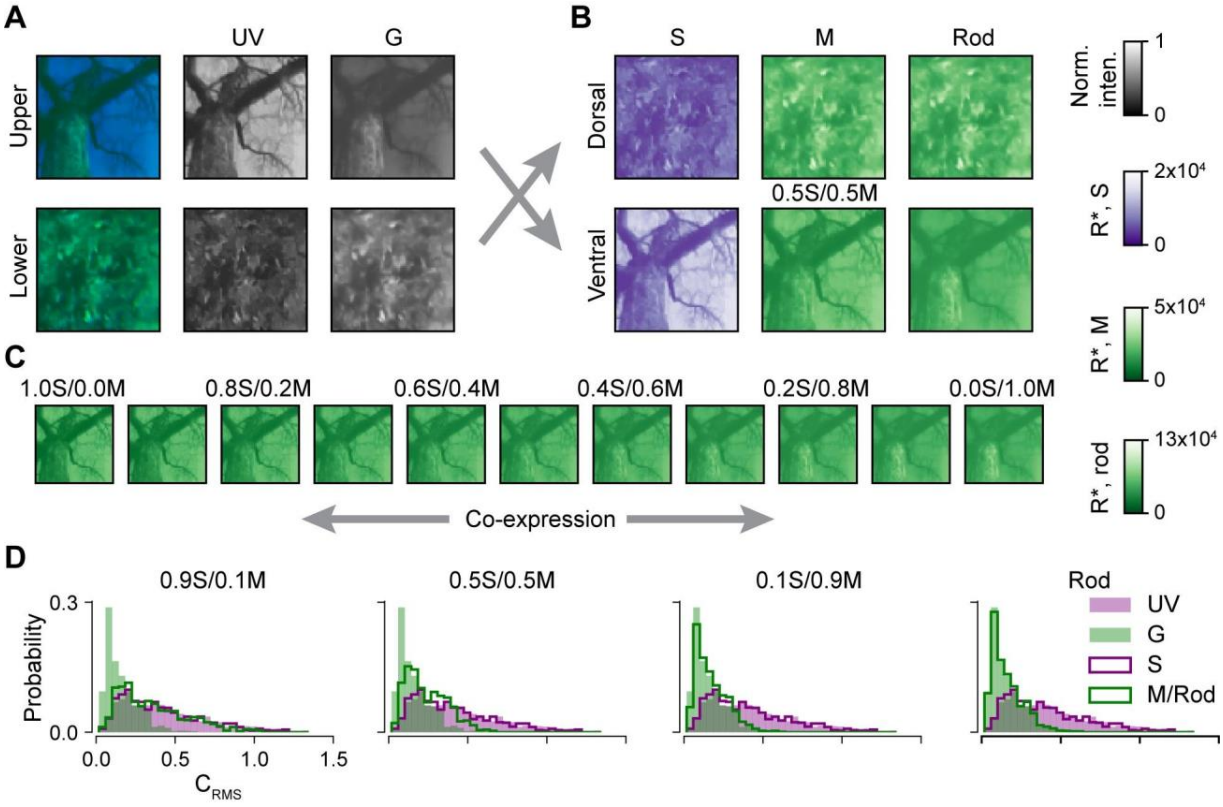

Figure S2 | Relating camera image intensities to photoisomerisation rates at the photoreceptor level. Related to Figure 2.

A, Example image crops (overlay, UV and green) from the upper and lower visual field (normalized intensities). **B**, Images from (A) but as estimated photoisomerisation rates (in R^*s^{-1} per photoreceptor) for S- (left) and M-cones (centre) as well as rods (right). For the ventral M-cones, a co-expression ratio of 1:1 was used. **C**, Like ventral M-cone image in (B) but for different S/M co-expression ratios, from 100% S-opsin (left) to 100% M-opsin (right). **D**, C_{RMS} distributions (d_{RF}=6°) for UV and green (filled bars; cf. Figure 3C-E) overlaid with distributions for S-cones, M-cones, and rods. From left to right: M-cones with 90%, 50% and 10% S-opsin co-expression, and rods.

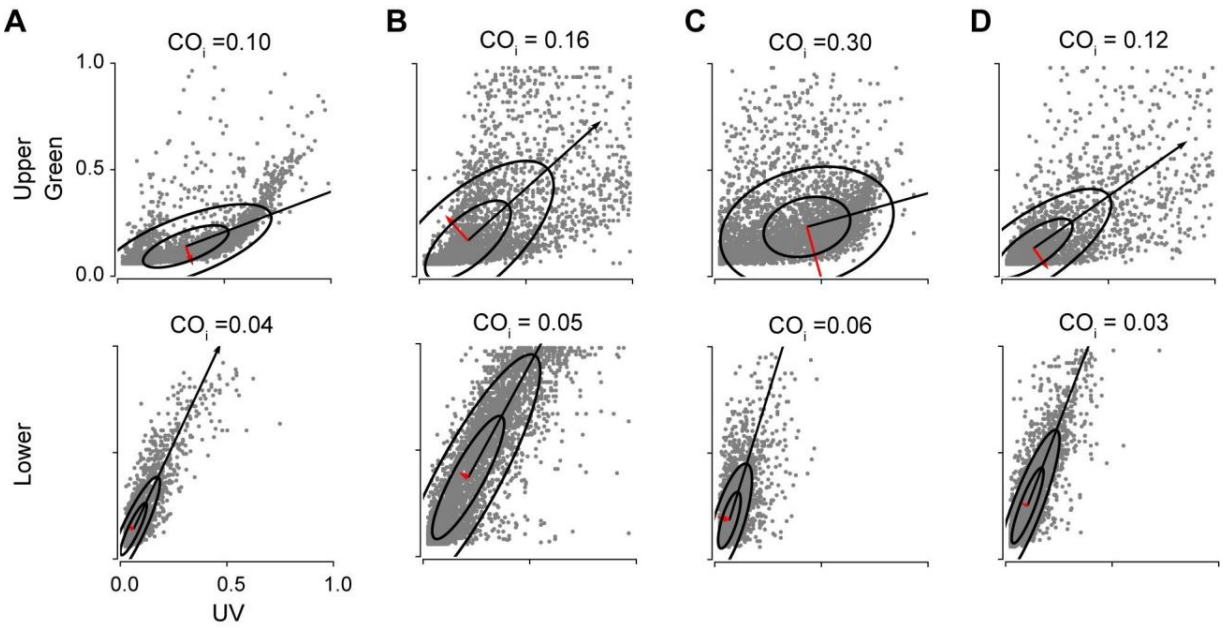

Figure S3 | The colour opponency index (COi) estimated with principal component analysis (PCA) is higher in the upper compared to the lower visual field. Related to Figure 3.

PCA is classically used to disentangle achromatic (1st PC) from colour-opponent (2nd and higher PCs) dimensions [S2]. **A-D**, 2D plots of 1st and 2nd principle components for intensities of image crops from the upper (top row) and lower (bottom row) visual field. Each dot represents a green-UV intensity pair. Data was fitted with bivariate normal distribution, with ellipses representing 1 and 2 SD. Black and red arrow indicate first and second eigenvector, reflecting the achromatic and the colour-opponent transforms, respectively. For movies, see Figure 2A and Table 4; (A) top-left, “20190329_13_3”; (B) centre-left, “20180713_13_1”; (C) centre-right, “20180905_14_2”; (D) bottom-left, “20190329 _12_1”). These results are consistent with the idea that chromatic signals are decorrelated at the retinal level [S3,S4] and in line with recent studies that suggest a predominance of colour opponent circuits in the ventral mouse retina [S5,S6].

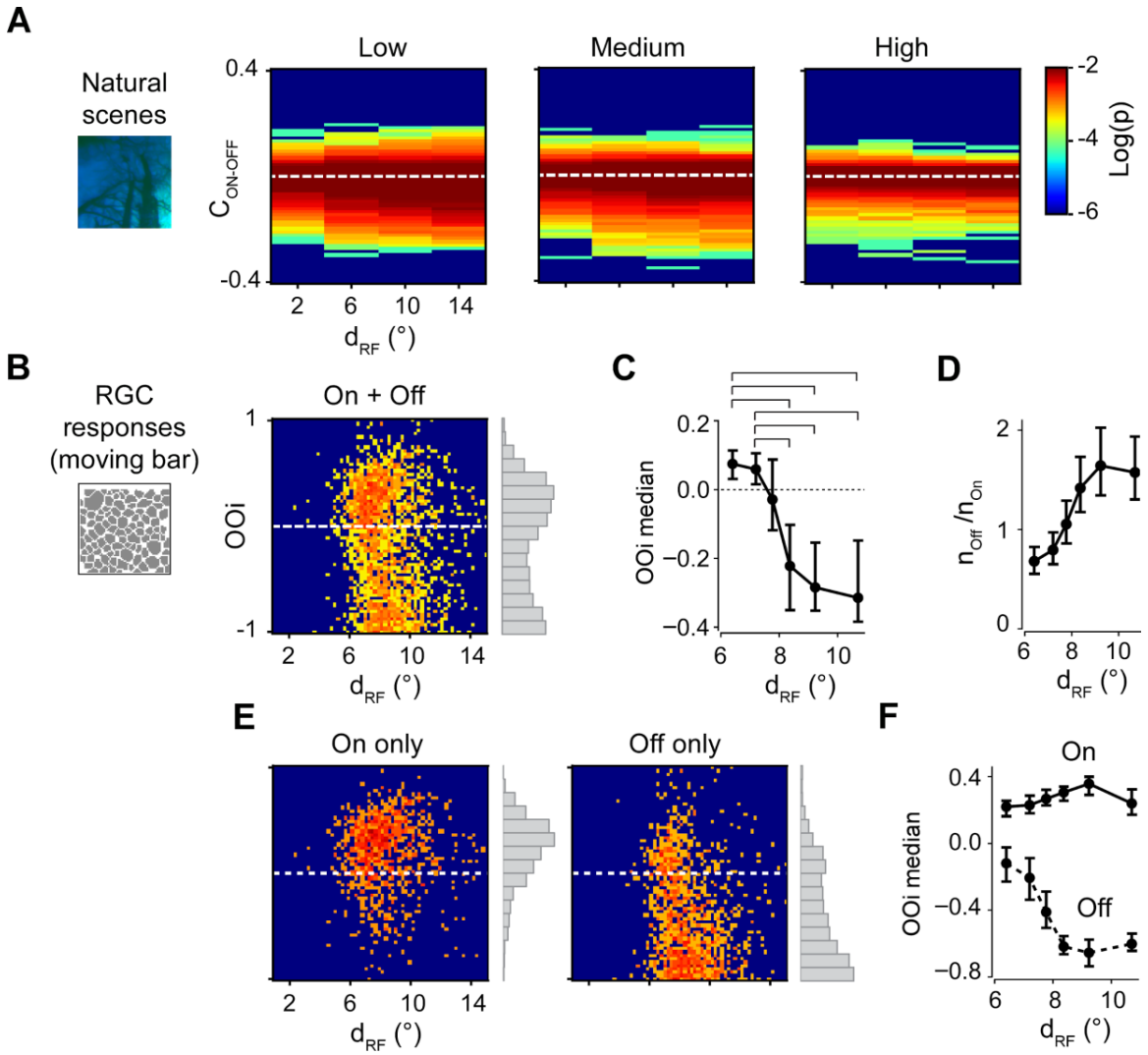

Figure S4 | Bias towards dark contrasts in the upper visual field is reflected in a higher frequency of larger-RF Off RGCs in the ventral retina. Related to Figure 4.

A, 2D histogram showing On-Off contrast (C_{On-Off}) measured in upper visual field image crops (same as used for C_{RMS} and C_{On-Off} in Figs. 3 and 4, respectively) as function of RF kernel diameter (d_{RF}). **B**, 2D histogram showing On-Off index (OOi; see Methods) as function of d_{RF} for n=2,380 RGCs recorded in the ventral retina (dataset from [S7]). Right: Histogram of OOi frequency across RF diameters. **C**, Median OOi as function d_{RF} (brackets indicate p<0.0001; permutation test). **D**, Ratio of Off vs. On RGCs as a function of d_{RF} (with Off and On cells defined as OOi <0 and OOi > 0, respectively). **E**, 2D histogram as in (B) but for On (left) or Off (right) RGCs separately (On, G_{15-30}; Off, $G_{1-9,31,32}$, as defined in [S7]). **F**, Like (C) but for On and Off RGCs separately. Panels (C-F): Same dataset as in (B); (C,D,F): Cells divided equally into 6 groups based on their d_{RF}; error bars represent 2.5–to-97.5 percentile confidence intervals after bootstrapping.

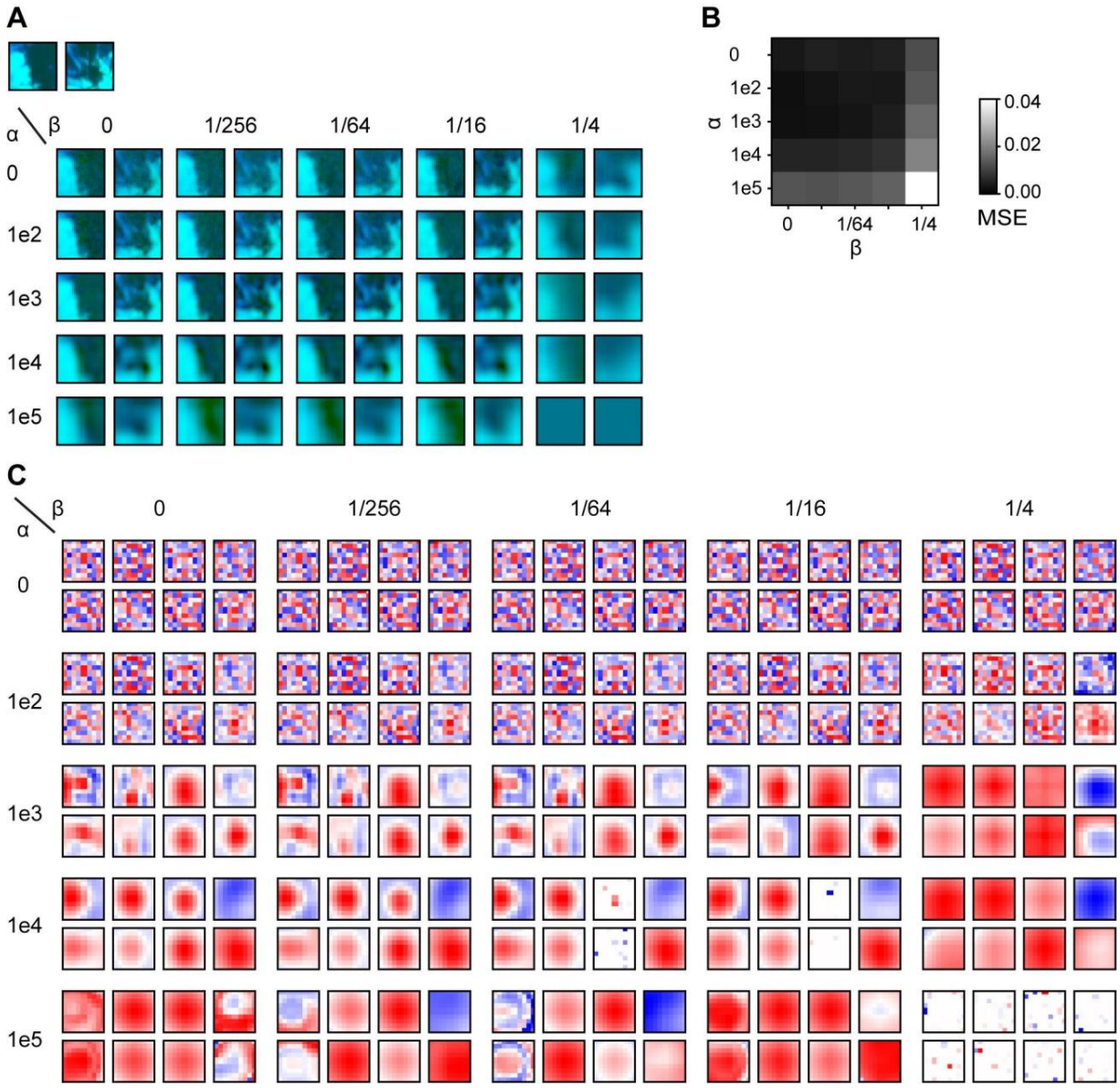

Figure S5 | Training the convolutional autoencoder (CAE) model using image crops from the upper visual field. Related to Figure 6.

A, Reconstruction of two exemplary image crops (upper left corner) under different regularization values for α (L2) and β (L1). **B**, Reconstruction performance using the mean square error (MSE) as metric. A sudden drop in performance happens for $\alpha = 10^5$ or β = 1/4, suggesting over-regularization. **C**, Four of the 16 convolutional kernels under the regularizations from (a). Smooth Gaussian- or Gabor-like kernels are learned for $\alpha = 10^3$ .. 10^4 and β = 0 … 1/16. For details, see Results and Methods.

Group	Visual field	Camera channel	Norm. intensity	Power in [µW]	Photon flux in [photons/s] at the cornea	Pupil area in [mm^2] (diameter)	Photoisomerisation in [P*/photoreceptor/s]		
					x 10^{15}		S, x10^4	M, x10^4	Rod, x10^4
I_1 (Low)	Upper	UV	0.18	0.14	1.9	0.1 (0.36)	0.5	<0.1	0.2
		G	0.11	0.73	1.2		<0.1	0.7	1.7
	Lower	UV	0.06	0.05	0.7		0.2	<0.1	<0.1
		G	0.14	0.93	1.5		<0.1	0.9	2.1
I_2 (Medium)	Upper	UV	0.28	0.22	2.9		0.7	0.1	0.3
		G	0.16	1.06	1.7		<0.1	1.0	2.4
	Lower	UV	0.09	0.07	1.0		0.2	<0.1	0.1
		G	0.21	1.39	2.3		<0.1	1.3	3.2
I_3 (High)	Upper	UV	0.50	0.38	5.1		1.3	0.2	0.6
		G	0.34	2.24	3.7		<0.1	2.1	5.1
	Lower	UV	0.22	0.17	2.3		0.6	0.1	0.3
		G	0.46	3.02	5.0		<0.1	2.8	7.0
Twilight	Upper	UV	0.05	0.04	0.6	0.22 (0.53)	0.3	<0.1	0.2
		G	0.06	0.40	0.7		<0.1	0.8	2.0
	Lower (1)	UV	0.02	0.02	0.3		0.2	<0.1	<0.1
		G	0.05	0.34	0.6		<0.1	0.7	1.7

Table S1. | Related to Figure 2.

Mean intensities of the three image classes for the UV and the green channel in the upper and lower visual field. For calculations, see STAR Methods. (1) Note that at twilight, the lower limit cannot be reliably determined because parts of the camera chip may be affected by under-exposure.

Group	d_{RF}(°)	Upper UV vs. Upper G	Upper UV vs. Lower UV	Upper UV vs. Lower G	Upper G vs. Lower UV	Upper G vs. Lower G	Lower UV vs. Lower G
C_{RMS}							
I_1	2	<0.0001	0.0063	<0.0001	<0.0001	<0.0001	<0.0001
	6	<0.0001	0.9355	<0.0001	<0.0001	<0.0001	<0.0001
	10	<0.0001	<0.0001	<0.0001	<0.0001	<0.0001	<0.0001
	14	<0.0001	<0.0001	<0.0001	<0.0001	<0.0001	<0.0001
I_2	2	<0.0001	0.2608	<0.0001	<0.0001	<0.0001	<0.0001
	6	<0.0001	0.0018	<0.0001	<0.0001	<0.0001	<0.0001
	10	<0.0001	<0.0001	<0.0001	<0.0001	<0.0001	<0.0001
	14	<0.0001	<0.0001	<0.0001	<0.0001	<0.0001	<0.0001
I_3	2	<0.0001	0.0001	<0.0001	<0.0001	<0.0001	<0.0001
	6	<0.0001	<0.0001	0.3896	<0.0001	<0.0001	<0.0001
	10	0.0521	<0.0001	0.0631	<0.0001	0.8926	<0.0001
	14	<0.0001	<0.0001	<0.0001	<0.0001	0.0768	<0.0001
C_{On-Off}							
I_1	2	<0.0001	0.0385	0.2284	<0.0001	<0.0001	<0.0001
	6	<0.0001	0.0037	<0.0001	<0.0001	<0.0001	0.0024
	10	<0.0001	<0.0001	<0.0001	0.2957	<0.0001	0.0109
	14	<0.0001	<0.0001	<0.0001	0.7145	<0.0001	<0.0001
I_2	2	0.0088	<0.0001	<0.0001	<0.0001	<0.0001	0.9963
	6	0.7321	0.5489	0.5715	0.4779	0.5677	0.916
	10	0.6861	0.1849	0.7181	0.0271	0.2943	0.4051
	14	0.1577	0.2937	<0.0001	0.9944	<0.0001	<0.0001
I_3	2	0.001	<0.0001	0.0006	<0.0001	0.4675	0.0014
	6	<0.0001	<0.0001	<0.0001	0.0116	0.585	0.0865
	10	<0.0001	0.0001	0.5744	0.0001	<0.0001	0.013
	14	<0.0001	<0.0001	0.1236	<0.0001	<0.0001	<0.0001

Table S2 | **Related to Figure 3 and Figure 4.**

Statistics of C_{RMS} and C_{On-Off} between chromatic channels and upper vs. lower visual field as function of kernel diameter. Two-sided permutation test (distribution medians) with 10,000 repeats. White, light and dark orange indicating $p < 0.0001$, $0.0001 \leq p < 0.05$ and $p \geq 0.05$

Group		2° vs. 6°	2° vs. 10°	2° vs. 14°	6° vs. 10°	6° vs. 14°	10° vs. 14°
C_{RMS}							
I_1	Upper UV	<0.0001	<0.0001	<0.0001	<0.0001	<0.0001	<0.0001
	Upper G	<0.0001	<0.0001	<0.0001	<0.0001	<0.0001	<0.0001
	Lower UV	<0.0001	<0.0001	<0.0001	<0.0001	<0.0001	<0.0001
	Lower G	<0.0001	<0.0001	<0.0001	<0.0001	<0.0001	<0.0001
I_2	Upper UV	<0.0001	<0.0001	<0.0001	<0.0001	<0.0001	<0.0001
	Upper G	<0.0001	<0.0001	<0.0001	<0.0001	<0.0001	<0.0001
	Lower UV	<0.0001	<0.0001	<0.0001	<0.0001	<0.0001	<0.0001
	Lower G	<0.0001	<0.0001	<0.0001	<0.0001	<0.0001	<0.0001
I_3	Upper UV	<0.0001	<0.0001	<0.0001	<0.0001	<0.0001	<0.0001
	Upper G	<0.0001	<0.0001	<0.0001	<0.0001	<0.0001	<0.0001
	Lower UV	<0.0001	<0.0001	<0.0001	<0.0001	<0.0001	<0.0001
	Lower G	<0.0001	<0.0001	<0.0001	<0.0001	<0.0001	<0.0001
C_{On-Off}							
I_1	Upper UV	<0.0001	<0.0001	<0.0001	0.0008	<0.0001	<0.0001
	Upper G	<0.0001	<0.0001	<0.0001	<0.0001	<0.0001	<0.0001
	Lower UV	<0.0001	0.0028	<0.0001	0.1104	0.0052	<0.0001
	Lower G	<0.0001	<0.0001	<0.0001	0.0702	0.6212	0.0179
I_2	Upper UV	<0.0001	<0.0001	<0.0001	0.0015	<0.0001	<0.0001
	Upper G	<0.0001	<0.0001	<0.0001	<0.0001	<0.0001	<0.0001
	Lower UV	0.1519	0.0042	<0.0001	0.2354	<0.0001	<0.0001
	Lower G	0.047	<0.0001	<0.0001	0.0302	0.0052	0.5913
I_3	Upper UV	<0.0001	0.0001	0.5502	0.0294	0.0001	0.1266
	Upper G	0.0093	<0.0001	<0.0001	<0.0001	<0.0001	<0.0001
	Lower UV	0.8311	0.0262	0.0018	0.0159	0.0134	<0.0001
	Lower G	0.1939	0.0022	<0.0001	0.0006	<0.0001	0.5453

Table S3 | Related to Figure 3 and Figure 4.

Statistics of C_{RMS} and C_{On-Off} between chromatic channels and upper vs. lower visual field as a function of kernel diameter. Two-sided permutation test (distribution medians) with 10,000 repeats. White, light and dark orange indicating $p < 0.0001$, $0.0001 \leq p < 0.05$ and $p \geq 0.05$.

Kernel size [pixels]	equivalent RF diameter, visual angle [°] (distance on retina [µm])	Training data from mean intensity group(s)	p-value (Pearson correlation coefficient)
5x5	4.1 (≈120)	I_1, I_2, I_3	0.6043
9x9	7.4 (≈220)		0.0122
13x13	10.7 (≈320)		0.0111
9x9	7.4 (≈220)	I_1, I_2	0.0123
		I_3	<0.0001

Table S4 | **Related to Figure 6.**

Performance of CAE model for different kernel sizes. Except for the smallest kernel size (5x5), the CAE trained with images from the upper visual field learned significantly more often colour-opponent kernels than the one trained with lower visual scene images (validated by permutation test).

Supplemental References

S1. Baden, T., Schubert, T., Chang, L., Wei, T., Zaichuk, M., Wissinger, B., and Euler, T. (2013). A tale of two retinal domains: near-optimal sampling of achromatic contrasts in natural scenes through asymmetric photoreceptor distribution. Neuron *80*, 1206–1217.

S2. Buchsbaum, G., and Gottschalk, A. (1983). Trichromacy, opponent colours coding and optimum colour information transmission in the retina. Proc. R. Soc. Lond. B Biol. Sci. *220*, 89–113.

S3. Graham, D.J., Chandler, D.M., and Field, D.J. (2006). Can the theory of “whitening” explain the center-surround properties of retinal ganglion cell receptive fields? Vision Res. *46*, 2901–2913.

S4. Abbasi-Asl, R., Pehlevan, C., Yu, B., and Chklovskii, D. (2016). Do retinal ganglion cells project natural scenes to their principal subspace and whiten them? 2016 50th Asilomar Conference on Signals, Systems and Computers.

S5. Szatko, K.P., Korympidou, M.M., Ran, Y., Berens, P., Dalkara, D., Schubert, T., Euler, T., and Franke, K. (2020). Neural circuits in the mouse retina support color vision in the upper visual field. Nat. Commun. *11*, 3481.

S6. Nadal-Nicolás, F.M., Kunze, V.P., Ball, J.M., Peng, B.T., Krishnan, A., Zhou, G., Dong, L., and Li, W. (2020). True S-cones are concentrated in the ventral mouse retina and wired for color detection in the upper visual field. eLife *9*:e56840.

S7. Baden, T., Berens, P., Franke, K., Román Rosón, M., Bethge, M., and Euler, T. (2016). The functional diversity of retinal ganglion cells in the mouse. Nature *529*, 345–350.

3

VISION: HOW MICE CONTROL THEIR VIEW

This dispatch was published as:
Kautzky, M. and Busse, L. (2020) Vision: How Mice Control Their View. *Current Biology* 30, R635–R662, https://doi.org/10.1016/j.cub.2020.04.063.

Contribution summary:

Writing - Original Draft: Laura Busse, Magdalena Kautzky; Writing - Review and Editing: Laura Busse, Magdalena Kautzky;

Personal contributions:

I wrote the original draft of the dispatch, and contributed to the review and preparation of the published version. I also conceptualized the illustration and contributed to its implementation.

Current Biology

CellPress

Dispatches

Vision: How Mice Control Their View

Magdalena Kautzky[1,2] and Laura Busse[1,3,*]
[1]Division of Neurobiology, Department Biology II, LMU Munich, 82151 Munich, Germany
[2]Graduate School of Systemic Neuroscience (GSN), LMU Munich, 82151 Munich, Germany
[3]Bernstein Centre for Computational Neuroscience, 82151 Munich, Germany
*Correspondence: busse@bio.lmu.de
https://doi.org/10.1016/j.cub.2020.04.063

Across vertebrates, eye movements serve the dual purpose of image stabilization during head or body movement, and gaze relocation. A new study has measured head and bilateral eye movements in freely moving mice, providing a detailed characterization of dynamic gaze behavior.

To gather visual information relevant for survival and reproduction, animals have evolved different types of eye movements to shift their line of sight, or gaze [1]. Among the mammals, for instance, some primates, including humans, have a fovea, a specialization of the retina consisting of a small region with peak cone density for high-acuity vision [2]. With this central spot on our retina, our frontal eyes, and thus a relatively narrow field of binocular vision, we scan our environment with high-velocity, conjugate movements of both eyes, known as saccades, which can be coupled to slow rotations of the head or occur independently [3,4]. In contrast, small animals, like mice, shift gaze almost exclusively with a combination of eye and head movements, during which fast head movements are coupled to slower eye movements [1].

Likely explanations for such a strategy in mice are that their laterally placed eyes already monitor a large fraction of their surroundings, and that the small size and weight of their head, compared to primates, makes rapid head motion energetically more affordable. Even though these general principles of sensorimotor gaze control in mice have been known for some time, detailed measurements of eye–head coupling in the mouse under unrestrained conditions are rare. This is mainly due to the technical obstacles imposed by the small eyes of mice, and their small body size and low weight, which require any head-mounted gear to be extremely lightweight and miniaturized. As they report in this issue of *Current Biology*, Meyer *et al.* [5] have overcome these challenges and provide, in a technical *tour de force*, a comprehensive characterization of two types of eye–head coupling during various visually guided behaviors.

Building on their earlier work [6], Meyer *et al.* [5] equipped mice with a lightweight, miniaturized tracking system (Figure 1, left). Two head-mounted miniature cameras tracked, through infrared mirrors, the position of both eyes. An inertial measurement unit, also mounted on the head, provided information about head motion and orientation relative to the ground. All relevant hardware, building instructions, and analysis code are shared by the authors as open resources with the community (https://arnefmeyer.github.io/mousecam), an exemplary model of open science. Outfitted with these custom–designed components, mice were set free to explore a confined environment.

Meyer *et al.* [5] found two distinct modes according to which mice controlled gaze, both being characterized by closely coupled eye and head movements (Figure 1, right). The first mode of gaze control that the authors highlight stabilizes the visual field with respect to the ground (Figure 1, right top). This mode occurs during head movements relative to the earth–horizontal plane, which are called tilt, and comprise head roll (rotations of the head around the nose–tail axis) and head pitch (rotations around the interaural axis or, equivalently, up–down movements of the nose). Coupled to these head movements are bilateral eye movements in opposite directions, also called non-conjugate eye movements. For example, when the mouse performs a roll motion of the head to the right side, the right eye moves upward and the left eye moves downward [6–8]. These short latency, compensatory eye movements are highly conserved across mammals, and driven by a specific form of the vestibular-ocular reflex called 'ocular counter roll', which originates mainly from the otolith organs of the vestibular system [9]. When Meyer *et al.* [5] computed in their new data set the angle between the mouse's gaze and the horizontal plane, they realized that this gaze angle was relatively constant and centered on the angle of the eye axis when the head was horizontally levelled [5].

From these results, Meyer *et al.* [5] conclude that tilt-related eye–head coupling in the mouse could serve to stabilize the visual field relative to the horizon. Such an alignment with the horizontal plane might have substantial benefits for visual processing, considering the functional optimization of ventral and dorsal mouse retina to process contrast of the upper and lower visual field [10].

The second mode of gaze control described by Meyer *et al.* [5] consists of another ancient motion sequence found in most vertebrates, the 'fixate and saccade' mode [4] (Figure 1, right bottom). This mode occurs during head turns within the horizontal plane, which are accompanied by conjugate eye movements, where both eyes move in the same direction. Here, Meyer *et al.* [5] measured three distinct phases: first, an initial counteracting eye movement in the opposite direction to the horizontal head rotation; second, a rapid, saccadic eye movement in the direction of the head movement, which augments the gaze shift; and third, another compensatory eye movement in the direction opposite to head rotation. The authors interpret these eye movements as driven by the angular

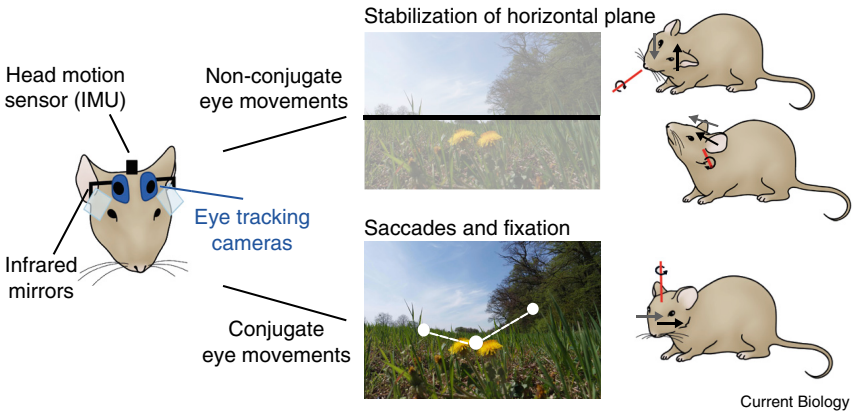

Figure 1. Two types of eye–head coupling in freely moving mice.
Using a head-mounted system for tracking movements of both eyes and the head (left), Meyer *et al.* [5] characterized two types of eye–head coupling in freely moving mice (right). During head roll and pitch, non-conjugate eye movements serve to keep gaze stable relative to the horizontal plane (right, top). Coupling of conjugate eye movements to head turns within the horizontal plane results in gaze shifts (saccades), separated by periods of stable gaze (fixation; right, bottom) (drawings: Annalenia Malzacher).

vestibular–ocular reflex, with the first and third phase contributing to gaze stability during periods of 'fixation', and the second phase to gaze shifts during periods of 'saccades'. Overall, the new study of Meyer *et al.* [5], together with a body of work in other species [4], suggests that mice primarily orient by head movements, which are the main drivers of gaze shifts around the scene.

How do these findings translate to richer behavioral conditions with salient sensory stimuli or when mice need to rely on vision? Previous evidence from humans and other animals suggests that gaze shifts can depend on the specific visual behavior that the individual is engaged in [4]. Two additional experiments allowed Meyer *et al.* [5] to shed light on this issue. First, the authors explored a naturalistic behavior and compared eye–head coupling before and during encounters with a conspecific male intruder, but found that both types of eye–head coupling were preserved. Because social behaviors likely engage multiple senses beyond vision, such as somatosensation and olfaction, the authors performed a second experiment. They implemented a more controlled visually guided task, which mimicked essential mouse behaviors, such as detection, approach, and tracking, but enforced the use of vision as the only relevant sense. In this task, mice were rewarded for tracking a moving square and indicating its target position on an infrared touchscreen. Even during this form of visually guided behavior, the two types of eye–head coupling described under exploration were preserved.

Remarkably, in parallel work reported in a pre-print [11], Cris Niell and colleagues have investigated the dynamics of gaze control in yet another ethologically relevant, visually guided mouse behavior — prey capture [12]. In this work too, mice were equipped with a head–mounted tracking system, which allowed to measure simultaneously movements of the eyes and head, while mice were chasing crickets. Even during rapid chasing of the prey, eye movements were found to serve the dual purpose of stabilizing gaze during head movements, and relocating gaze during directed head turns. Interestingly, Michaiel *et al.* [11] found that gaze stabilization was highly accurate (to nearly 1 deg), highlighting that, even during dynamic and interactive behaviors, vestibulo–ocular reflexes are adequately fast and precise enough to ensure that the mouse visual system receives a series of stable visual representations from the retina.

These tight stabilization mechanisms are unsurprising given the central fusion of signals from the semicircular canals and otoliths, and their appropriate distribution to the extraocular motor targets. However, the spatio–temporal adequacy is nonetheless highly interesting because it has important implications for mouse binocular vision and depth perception [13]. Whether mice can use disparity cues arising from viewing the same object from slightly different viewpoints provided by two eyes is still unclear: on the one hand, neurons in several areas of the mouse visual system have preferences for a range of binocular disparities [14,15] and mice are able to discriminate depth in random dot stereograms [15]; on the other hand, head-fixed mice neither seem to systematically vary relative eye position with depth nor use the vergence eye movements observed in primates [11,15]. Future studies exploiting the techniques developed by Meyer and colleagues [5,6] will provide excellent opportunities to clarify this issue under naturalistic viewing conditions.

At the level of neuronal circuits and cell types, we are beginning to understand how vestibular, proprioceptive and visual cues arising from eye or head movements are compared with predictions from internal forward models of motor control [16,17]. Such predictions, potentially in addition to low–level sensory mechanisms [18], might be responsible for the perception of a stable world in face of dynamic gaze shifts, and hence successful visual behavior.

REFERENCES

1. Land, M.F. (2015). Eye movements of vertebrates and their relation to eye form and function. J. Comp. Physiol. A *201*, 195–214.
2. Grünert, U., and Martin, P.R. (2020). Cell types and cell circuits in human and non-human primate retina. Prog. Retin. Eye Res. https://doi.org/10.1016/j.preteyeres.2020.100844.
3. Freedman, E.G. (2008). Coordination of the eyes and head during visual orienting. Exp. Brain Res. *190*, 369–387.
4. Land, M. (2019). Eye movements in man and other animals. Vision Res. *162*, 1–7.
5. Meyer, A.F., O'Keefe, J., and Poort, J. (2020). Two distinct types of eye-head coupling in freely moving mice. Curr. Biol. *30*, 2116–2130.
6. Meyer, A.F., Poort, J., O'Keefe, J., Sahani, M., and Linden, J.F. (2018). A head-mounted camera system integrates detailed behavioral monitoring with multichannel electrophysiology in freely moving mice. Neuron *100*, 46–60.

7. Wallace, D.J., Greenberg, D.S., Sawinski, J., Rulla, S., Notaro, G., and Kerr, J.N.D. (2013). Rats maintain an overhead binocular field at the expense of constant fusion. Nature *498*, 65–69.

8. Oommen, B.S., and Stahl, J.S. (2008). Eye orientation during static tilts and its relationship to spontaneous head pitch in the laboratory mouse. Brain Res. *1193*, 57–66.

9. Migliaccio, A.A., Meierhofer, R., and Della Santina, C.C. (2011). Characterization of the 3D angular vestibulo-ocular reflex in C57BL6 mice. Exp. Brain Res. *210*, 489–501.

10. Baden, T., Schubert, T., Chang, L., Wei, T., Zaichuk, M., Wissinger, B., and Euler, T. (2013). A tale of two retinal domains: near-optimal sampling of achromatic contrasts in natural scenes through asymmetric photoreceptor distribution. Neuron *80*, 1206–1217.

11. Michaiel, A.M., Abe, E.T.T., and Niell, C.M. (2020). Dynamics of gaze control during prey capture in freely moving mice. bioRxiv006817, 2020.03.25.

12. Hoy, J.L., Yavorska, I., Wehr, M., and Niell, C.M. (2016). Vision drives accurate approach behavior during prey capture in laboratory mice. Curr. Biol. *26*, 3046–3052.

13. Parker, A.J. (2007). Binocular depth perception and the cerebral cortex. Nat. Rev. Neurosci. *8*, 379–391.

14. La Chioma, A., Bonhoeffer, T., and Hübener, M. (2019). Area-specific mapping of binocular disparity across mouse visual cortex. Curr. Biol. *29*, 2954–2960.

15. Samonds, J.M., Choi, V., and Priebe, N.J. (2019). Mice discriminate stereoscopic surfaces without fixating in depth. J. Neurosci. *39*, 8024–8037.

16. Straka, H., Simmers, J., and Chagnaud, B.P. (2018). A new perspective on predictive motor signaling. Curr. Biol. *28*, R232–R243.

17. Cullen, K.E. (2019). Vestibular processing during natural self-motion: implications for perception and action. Nat. Rev. Neurosci. *20*, 346–363.

18. Idrees, S., Baumann, M.P., Franke, F., Münch, T.A., and Hafed, Z.M. (2020). Perceptual saccadic suppression starts in the retina. Nat. Commun. *11*, 1977.

Cell Biology: Tubulin Contributes to Spindle Size Scaling

Daniel L. Levy
Department of Molecular Biology, University of Wyoming, Laramie, WY 82071, USA
Correspondence: dlevy1@uwyo.edu
https://doi.org/10.1016/j.cub.2020.04.017

Sizes of intracellular structures are important for function, yet mechanisms underlying subcellular size control are largely unexplored. A new study reveals how differences in tubulin populations between two related *Xenopus* frog species influence microtubule dynamics and spindle length.

Our sense of size in the macroscopic world is relatively intuitive. A tape measure allows one to assess and modify the size of an object to fit within a defined space. Proper ingredient volumes and weights are dispensed when following a recipe. Perhaps less obvious is whether size is relevant at the microscopic level. Are cell sizes actively regulated and do cells care about the sizes of their internal structures? Apparently so, because in a given context, cell and organelle sizes tend to be maintained within a defined range and aberrant size regulation is often associated with disease [1]. A particularly useful framework for thinking about size is early embryonic development when rapid cell divisions occur without growth, giving rise to progressively smaller cells over time. As cells become smaller, intracellular structures such as the nucleus and mitotic spindle also reduce in size, a phenomenon referred to as organelle size scaling [2]. Comparing related species can provide other physiologically relevant settings to investigate size. One pair of frogs exemplifies interspecies size scaling: *Xenopus laevis* animals, eggs, cells, and organelles are generally larger than those of *Xenopus tropicalis*. A new study in this issue of *Current Biology* from Hirst *et al.* elucidates one mechanism that contributes to longer spindles in *X. laevis* compared with *X. tropicalis* [3].

When cells divide, duplicated chromosomes must be faithfully segregated into the two daughter cells. The mitotic spindle is a football-shaped structure responsible for grabbing chromosomes and pulling them in opposite directions as the mitotic cell divides. The main structural components of the spindle are microtubules, built from α/β-tubulin heterodimers that dynamically nucleate, assemble, and disassemble. Additional microtubule-associated proteins (MAPs), enzymes, and motors regulate spindle morphology and function [4]. It is important that the size of the spindle is properly regulated relative to the size of the cell. Spindles of the wrong size may not sufficiently segregate chromosomes, leading to aneuploidy associated with cancers and birth defects [5]. For instance, a short spindle may not be able to physically separate the chromosomes, while a long spindle may not interact properly with the cell cortex, leading to disrupted anaphase and cytokinesis.

Microtubule dynamics are key determinants of spindle length scaling. During early development in *Caenorhabditis elegans*, the sea urchin *Paracentrotus lividus*, and *X. laevis*, reductions in spindle length correlate with reduced microtubule growth rates, potentially mediated by limiting amounts of positive regulators of microtubule growth such as XMAP215 and CLS-2 [6–10]. In *X. laevis*, spindle recruitment of

4

MICE ADJUST EYE POSITION DURING VIEWING OF NATURALISTIC MOVIES

This manuscript is in preparation as:
Kautzky, M.*, Qiu, Y.*, Zhao, Z., Euler, T., Busse, L. (2022) Mice adjust eye position during viewing of naturalistic movies. *in preparation*
*shared first authorship between M.K. and Y.Q.

Contribution summary:

Conceptualization: Laura Busse, Thomas Euler; Methodology: Laura Busse, Thomas Euler, Magdalena Kautzky, Yongrong Qiu, Zhijian Zhao; Software: Magdalena Kautzky, Yongrong Qiu; Formal Analysis: Yongrong Qiu; Investigation: Magdalena Kautzky; Resources: Laura Busse, Thomas Euler; Data Curation: Laura Busse, Magdalena Kautzky, Yongrong Qiu; Writing - Original Draft: Laura Busse, Magdalena Kautzky; Writing - Review and Editing: all authors; Visualization: Magdalena Kautzky, Yongrong Qiu; Supervision: Laura Busse, Thomas Euler; Project Administration: Laura Busse, Thomas Euler; Funding Acquisition: Laura Busse, Thomas Euler

Personal contributions:

I developed the method for calibration of the dome setup, designed and built the device to hold the laser pointer and carried out the calibration. I also built the head-mounted camera system, did the implantation surgery and conducted all experiments. I designed the experiments with input from the rest of the team and implemented the visual stimuli. Eye movement movies were preprocessed by me by fitting pupil position with DLC and I developed the code for the analysis of eye movements for Figures 2 and 4 and contributed to code for further analysis. I created Figures 1-4 and provided input to figures 5, 6, 7. Lastly, I wrote the original draft of the manuscript together with Laura Busse, and performed the first sets of revisions and edits, before the other authors also joined the editing process.

Mice adjust eye position during viewing of naturalistic movies

Abbreviated title: Eye movements in mice

Magdalena Kautzky [1,2,*], Yongrong Qiu [3,4,*], Zhijian Zhao [3,4],
Thomas Euler [3,4,5,†], Laura Busse [1,6,†]

[1]Division of Neurobiology, Faculty of Biology, LMU Munich, 82152 Munich, Germany
[2]Graduate School of Systemic Neurosciences (GSN), LMU Munich, 82151 Munich, Germany
[3]Centre for Integrative Neuroscience, University of Tübingen, 72076 Tübingen, Germany
[4]Institute for Ophthalmic Research, University Hospital Tübingen, 72076 Tübingen, Germany
[5]Bernstein Centre for Computational Neuroscience, 72076 Tübingen, Germany
[6]Bernstein Centre for Computational Neuroscience, 82151 Munich, Germany
[*] Equal contribution
[†]Shared senior authors
thomas.euler@cin.uni-tuebingen.de; busse@bio.lmu.de

Conflict of Interest: The authors declare no competing financial interests.

Author Contributions: Conceptualization, L.B., T.E.; Methodology, L.B., T.E., M.K., Y.Q., Z.Z.; Software, M.K., Y.Q.; Formal Analysis, Y.Q.; Investigation, M.K.; Resources, L.B., T.E.; Data Curation, L.B., M.K., Y.Q.; Writing – Original Draft, L.B., M.K.; Writing – Review & Editing, all authors; Visualization, M.K., Y.Q.; Supervision, L.B., T.E.; Project Administration, L.B., T.E.; Funding Acquisition, L.B., T.E.

Acknowledgments: This research was supported by the Deutsche Forschungsgesellschaft (DFG) Sonderforschungsbereich (SFB) 1233, *Robust Vision: Inference Principles and Neural Mechanisms*, Teilprojekt (TP) 10, project number: 276693517 (L.B., T.E.). We thank A. Meyer for help with establishing head-mounted eye tracking, S. Katzner for software for visual stimulation and experimental control, and D. Crombie for software related to behavioral analyses, and L. Schmors for support with data management. We also thank T. Wachtler for advice and sharing of equipment used for calibrating the dome, and A. Genewsky for useful suggestions and discussion about hardware development. Thanks also go to M. Sotgia for lab management and support with animal handling, S. Schörnich for IT support, and B. Grothe for providing an excellent research infrastructure.

Abstract

For any given animal species, the structure and function of its visual system reflects the sensory and behavioral features of its ecological niche. In mice, such specializations comprise a wide field of view covering $> 300°$, including most of overhead space (reviewed in Seabrook et al., 2017), and a gradient in the distribution of the two cone opsin types in the retina (Szél et al., 1992). Indeed, this gradient of expression of the green-sensitive M-opsin and the UV-sensitive S-opsin results in a more green-sensitive dorsal and a strongly UV-sensitive ventral retina (Szél et al., 1992; Baden et al., 2013). To improve our understanding of these adaptations and how the mouse might exploit them during active sampling of visual information, a fruitful approach is to probe the visual system with naturalistic, species-specific stimuli.

To present mouse-specific stimuli, naturalistic with regards to coverage and color, we developed a hemispheric dome setup, which allows for controlled projection of wide-field movies with UV-/green spectral content. To overcome spatial distortions introduced by the projection (Bourke, 2005), we designed a low-cost, fast and precise calibration procedure, which does not make any assumptions about the specific geometry of the setup. To achieve sufficient light intensities, in particular for UV, we combined a powerful light source with several custom-adaptations of our projector. As visual stimuli, we exploited the outdoors movies of mouse habitats, which we had recently recorded with a custom-built UV- and green-sensitive camera (Qiu et al., 2021). To capture behavioral responses elicited by the visual input, we equipped mice with a head-mounted eye tracking system (adapted from Meyer et al., 2018; Sattler and Wehr, 2021).

After verifying sufficient brightness and ensuring that we could elicit eye movements with standard stimuli, we first focused on characterizing eye position during the presentation of our naturalistic movies. As expected based on earlier work (Land, 2015), we found that mice do not use saccadic eye movements to orient to specific features of the movie scenes. Interestingly, however, we observed that eye position was systematically shifted towards more frontal and ventral regions of visual space during viewing of the naturalistic movies compared to a uniform gray screen control. This indicates that depending on the content of visual input, mice adjust general eye position, potentially to optimize visual processing of information arising from the visual field just ahead. Together, these results contribute to the emerging view that mice perform complex oculo-motor behaviors to orient towards relevant visual information.

Introduction

Through evolutionary pressures, the visual system of animals is adapted to the statistics of their natural environments and behavioral needs, to promote survival and procreation (Baden et al., 2020; Land, 2015; Sedigh-Sarvestani and Fitzpatrick, 2022). For instance, tuning preference of populations of neurons in the visual system have been found to match to the statistics of natural scenes, which contain considerable biases in the distribution of visual features (reviewed in Geisler, 2007; Sedigh-Sarvestani and Fitzpatrick, 2022). One of the most well studied examples is the dominance of cardinal orientations in natural scenes (Switkes et al., 1978; van der Schaaf and van Hateren, 1996; Coppola et al., 1998; Girshick et al., 2011; Betsch et al., 2004), which is paralleled by a cardinal bias in neuronal preferences: studies in humans (e.g., Yacoub et al., 2008; Nasr and Tootell, 2012), monkeys (e.g., Shen et al., 2014), cats (e.g, Li et al., 2003), ferrets (e.g., Coppola et al., 1998), and mice (e.g., Kreile et al., 2011) provide evidence for a higher proportion of visual cortex neurons preferring cardinal compared to oblique orientations. The relationship between response properties of visual neurons and the statistical structure of natural images has also been demonstrated in computational models, where sparseness constraints make learning algorithms develop filters similar to receptive fields (RFs) typically found in early cortical neurons (Olshausen and Field, 1996; Bell and Sejnowski, 1997). Such matching of the visual encoding resources to natural scene statistics, within the framework of generative modeling, may constitute a universal mechanism to achieve optimal neural coding and robust visual performance (Ganguli and Simoncelli, 2010; Girshick et al., 2011).

In the mouse, two prominent adaptations of the visual system are the large field of view (FOV) and the retinal gradient for UV and green sensitivity. Typical for animals of prey, mice have laterally placed eyes, which provide a panoramic view of $> 180°$ extending to the front, the sides, and the overhead space (Seabrook et al., 2017). The mouse senses the visual information from its surroundings by its rod and two types of cone photoreceptors (Haverkamp, 2005). The cones express cone opsins with sensitivities for wavelengths in the UV (S-opsin, peak 360 nm) and green range (M-opsin, peak 510 nm) (Jacobs et al., 2004). The S-cones (5% of the cones) exclusively express the S-opsin and are distributed throughout the retina, albeit with a concentration in the ventral retina (Nadal-Nicolás et al., 2020). The M-cones (95%) further contribute to this dorso-ventral UV-green gradient by co-expressing S-opsin, with co-expression ratios increasing towards the ventral retina (Applebury et al., 2000; Röhlich et al., 1994; Haverkamp, 2005; Baden et al., 2013). Such dorso-ventral UV-green gradient seems to reflect the statistics of mouse visual environments (Qiu et al., 2021), and might be particularly relevant for the detection of dark contrasts in the sky region (Qiu et al., 2021; Baden et al., 2013).

A promising approach for probing the function of the visual system is to use naturalistic, species-specific stimuli. Such stimuli, however, have so far rarely been used for the mouse, given limitations in both the visual stimulus material and its presentation. While several studies, inspired

by previous work in cats (Betsch et al., 2004), have acquired footage from head-mounted cameras in mice roaming in a cage or arena (e.g., Froudarakis et al., 2014; Hofer et al., 2011), these movies were only gray-scale and did not consider the effective image-stabilization in mice through eye movements (Meyer et al., 2018, 2020). Also, visual stimuli for mice are often presented on small off-the-shelf consumer displays, which only cover a small fraction of the mouse visual field and cannot activate the UV-opsin.

Recently, some of the technical limitations regarding stimulus material and presentation have been overcome, but so far these advances have not yet been used to probe naturalistic vision in mice. Indeed, two data sets with movies or images of outdoor mouse environments have been acquired with custom-made cameras, mimicking some aspects of the mouse visual system (Qiu et al., 2021; Abballe and Asari, 2022). These cameras were equipped with lenses capturing the large FOV in the mouse, mounted in ways to achieve image stabilization, and were sensitive in the spectrally-relevant UV- and green wavelengths. Furthermore, several solutions for visual stimulation in the UV spectrum have been proposed (Rhim et al., 2017; Franke et al., 2019; Denman et al., 2017; Tan et al., 2015), including an arbitrary-spectrum spatial visual stimulator (Franke et al., 2019). Finally, immersive visual stimulation, including from the overhead space, can now be provided in hemispheric dome setups (Shapcott et al., 2022; Lopes et al., 2021). So far, however, these elements to create a naturalistic, immersive visual environment for mice, have not yet been combined.

Here, we developed methods to present naturalistic visual stimuli in a hemispheric dome setup with the appropriate spectral content to head-fixed mice and measure their behavioral responses. We describe the components of our setup and provide robust methods for spatial calibration. We validated that we achieved sufficient intensity of stimulation by measuring the pupil light reflex (PLR). Measuring the optokinetic reflex (OKR), we also verified that our methods for measuring and quantifying eye movements in our setup have appropriate precision. Exploiting the naturalistic movies that we captured in our previous work (Qiu et al., 2021), we confirmed that mice under head-fixation conditions do not use saccadic eye movements to orient to specific features of the scenes. Interestingly, however, we found that mice systematically shifted eye position to more ventral and frontal regions of the visual field when viewing naturalistic movies compared to a mean-luminance gray screen. This finding adds to growing evidence that mice perform complex visuo-motor adjustments according to visual input, potentially to maximize coverage of the visual field just ahead.

Part #	Name	Vendor	Part number
1	Laser pointer	Amazon	NC5360-944
2	Rotation platform 1	Thorlabs	RP005/M
3	Rotation platform 2	Thorlabs	FP90/M
4	Rails	Thorlabs	RLA300/M and RLA450/M
5	Carrier	Thorlabs	RC2/M
6	Perpendicular carrier	Thorlabs	RC3
7	RPI Camera	Mouser Electronics	485-1937
8	IR mirror	Qoptiq	G380227033
9	IR LED	Osram	SFH 4726S
10	Raspberry Pi	Conrad Electronic	2634243 - 62
11	Power meter	Newport	842-PE
12	3D Printer	Ultimaker	Ultimaker 3 Extended

Table 1 Equipment for spatial calibration of the dome setup and building the eye tracking system

Materials and methods

Animals

All procedures complied with the European Communities Council Directive 2010/63/EU and the German Law for Protection of Animals, and were approved by local authorities following appropriate ethics review.

The experiments were conducted with three male PVCre mice (B6;129P2-Pvalbtm1(cre)Arbr/J; #008069, Jackson Laboratory) of eleven months of age at the beginning of the experiment. They were housed on a 12/12 h light-dark cycle, with experiments being conducted in their light phase.

Surgical procedures

Thirty minutes before the start of surgery, mice were injected subcutaneously with an analgesic (Metamizole, 200 mg/kg, sc, MSD Animal Health, Brussels, Belgium). Isoflurane (5% in oxygen, CP-Pharma, Burgdorf, Germany) anesthesia was slowly induced in a chamber. After induction, mice were fixated in a stereotaxic frame (Drill and Microinjection Robot, Neurostar, Tuebingen, Germany), with isoflurane being delivered through a face mask. The mice were placed onto a closed-loop heat plate (ATC 1000, WPI, Berlin, Germany), to ensure a stable body temperature of 37° Celcius. The flow rate and isoflurane concentration (0.5%–2% in oxygen) were adjusted to ensure a stable depth of anesthesia, as judged by the absence of the pedal reflex.

The eyes were covered with Bepanthen (Bayer, Leverkusen, Germany), and the ointment was re-applied several times during surgery. Additional analgesic (Buprenorphine, 0.1 mg/kg, sc, Bayer,

Leverkusen, Germany) was administered. The head was thoroughly depilated (Avon Skin-so-Soft, facial, Avon, Germany). For disinfection of the surgical area on the animal's head, an iodine solution (Braunodivon, 10%, B. Braun, Melsungen, Germany) was applied. After administration of a local anesthetic (Lidocaine hydrochloride, bela-pharm, Vechta, Germany), a skin incision was made with a scalpel and an oval piece of skin was removed above the midline. Subsequently, the skull was cleaned from any tissue residues, the periosteum was removed, and the bone was roughened by a drop of H_2O_2 (3%, AppliChem, Darmstadt, Germany). To ensure a skull-flat implantation of the headbar, four reference points (bregma, lambda, and two points 2 mm to the left and right of the midline, respectively) were measured, and, if required, the head was re-positioned.

The exposed and cleaned area of the skull was covered with OptiBond FL primer and adhesive (Kerr dental, Rastatt, Germany) and then hardened with UV light. A lightweight aluminium headbar (24×4 mm, **Fig. 1b, left**) was positioned centrally anterior to the ears above the skull and attached with dental cement (Ivoclar Vivadent, Ellwangen, Germany). Next, an aluminum camera holder (**Fig. 1b, left**) was implanted, whose bottom and side surfaces were filed before implantation to roughen the material for better adhesion. To ensure long-term stability and reproducibility of the camera position, but also minimal weight, the camera holder was a non-symmetrical, pentagon shaped aluminum block (side lengths: 500 x 700 x 280 x 500 x 530 mm). A small hole with an M2 thread was positioned on the side of the block pointing towards the back of the animal. This hole held a 3 mm plastic screw (Polyamide MXD6) with a pan shaped head (CSPPNR-RENY-M2-3, Misumi, Mexico).

To correctly position the camera holder during implantation, a miniature eye tracking camera system (see below) was attached while the camera holder was lowered towards the skull. As soon as the position of the camera holder was appropriate to yield high-quality images of the eye, a thin layer of superglue was spread between headbar and camera holder, and the holder was further lowered onto the headbar. The surrounding spaces between camera holder and skull were filled with dental cement, which was also used to build a small rim around the sides of the camera holder.

At the end of the surgery, the edges of the wounds were treated with Braunodivon (10%, B. Braun, Melsungen, Germany). A long-term analgesic (Meloxicam, 2 mg/kg, sc, Boehringer Ingelheim, Ingelheim, Germany) was injected. For 1 animal, in addition, an antibiotic (Baytril, 5 mg/kg, sc, Bayer Animal Health GmbH, Leverkusen, Germany) was administered. The analgesic was given for 3 consecutive days and the antibiotics for 7 days post operation. The health status of the mice was evaluated with a score sheet for at least 5 days after the surgery.

After the recovery period of one week post surgery, mice were accustomed to the setup and head fixation. During this time the focus and the mirror of the eye tracking camera (see below) were adjusted if necessary. After acclimatization, two recording sessions were carried out per day, for a maximum of one hour per session.

Hemispheric dome setup, mirror and illumination

To present visual stimuli covering most of the large field of view of the mouse, we implemented a hemispheric dome setup, consisting of a screen, a mirror, and a projector, all fixed on a frame and a bread board table (**Fig. 1a, c**). The mouse was head-fixed in the center of the dome and was free to run on a linear treadmill (Speed belt, PhenoSys, Berlin, Germany).

The dimensions of the hemispheric screen (PhenoSys, Berlin, Germany) were 120 cm in width, 113 cm in depth and 106 cm in height. From the position of the mouse in the center of the dome, this corresponded to a width of 250° and a height of 160°, thus covering substantial portions of the visual field of mice. An acrylic spherical mirror (PhenoSys, Berlin, Germany), which was the size of a quarter sphere, provided illumination of the inner dome surface. The mirror was positioned on the table at the bottom of the hemispherical screen, which made it possible to fix the projector to the table behind and slightly below the dome, thus preventing shadows of equipment while keeping the distance of the optical components small. The projector was centered onto the mirror, such that the center of the image was displayed in the center of the dome, directly in front of the animal. The projector was angled by about 13° (**Fig. 1c**) to sufficiently diverge the light hitting the outer areas of the mirror and thus ensure full illumination of the 250° wide dome.

To illuminate the dome, we used a Digital Light Processing (DLP) LightCrafter 4500 Fiber Couple projector (Fiber-E4500MKIITM, EKB Technologies Ltd., Israel; referred to as "LC") (Franke et al., 2019). A 6-wavelength, high-power LED Source (Chrolis, Thorlabs, USA) was connected to the LC via a liquid light guide (LLG). For stimulation of the mouse S-opsin, two LEDs peaking at 385 nm and 405 nm were used, with a total maximum power of 2,150 mW (measured at the end of the LLG; from now on referred to as "UV"). For stimulation of the M-opsin, a 475 nm LED and a 590 nm LED were combined, yielding a total light power of 770 mW (from now on referred to as "green"). To optimize the LC's light transmission, we performed two custom modifications: (1) we removed the first collimating lens, and (2) we replaced the dichroic mirror by a silver mirror to improve reflection of all wavelengths, including the UV light. Considering the output at the end of the LLG as 100%, we achieved transmission as measured at the LC's front lens of 8% of light from the 385 nm LED, 14% of light from the 405 nm LED, and 33% of light from the 590 nm LED.

Stimuli were presented with 8 bit depth and at a resolution of 912 × 1440 pixels. To further increase stimulus intensity, the LC was configured to operate in "pattern mode", which, amongst others, allows assigning each of the 24 bitplanes (3 RGB color channels × 8 bit) of every frame to an arbitrary combination of LEDs. Hence, restricting the video output to only two colors (green and UV), resulted in more time within a frame for the green and UV LEDs, and thus brighter images (Franke et al., 2019).

To relate the light intensity on dome surface to photoisomerization rates at the photoreceptor level, we used a power meter (**Table 1**, part #11) to measure the light power at the center of

the dome for the different LEDs with different wavelengths (λ, in $[nm]$). We calculated the light power in unit area (P_{el}, in $[W/m^2]$), by dividing the measured light power by the sensor area $A_{stim} = 10^{-4}m^2$. We then converted light power to photon flux (P_{Phi}, in $[photons/s/m^2]$) using:

$$P_{Phi}(\lambda) = \frac{P_{el}(\lambda) \cdot a \cdot \lambda \cdot 10^{-9}}{c \cdot h} \tag{1}$$

with constants $a = 6.242 \cdot 10^{18}\, eV/J$, the speed of light $c = 299,792,458\, m/s$, and Planck constant $h = 4.135667 \cdot 10^{-15}\, eV \cdot s$. We next estimated the photoisomerization rate (R_{Iso}, in $[P^*/cone/s]$) from P_{Phi}:

$$R_{Iso}(\lambda) = P_{Phi}(\lambda) \cdot S_{Act}(\lambda) \cdot T(\lambda) \cdot R_{pup2ret} \cdot A_{Collect} \cdot 10^{-12} \tag{2}$$

where S_{Act} represents the activation of photoreceptors with the LEDs considering the mismatch between their spectral sensitivities, T represents the transmission of light through the mouse eye, $R_{pup2ret}$ corresponds to the ratio between pupil area and retinal surface area, and $A_{Collect}$ (in $[\mu m^2]$) corresponds to light collection area of photoreceptor outer segments (for details, see Franke et al., 2019).

Eye tracking system

To investigate how mice move their eyes in response to wide-field UV and green stimuli, we recorded the right eye of head-fixed mice wearing a head-mounted camera system (**Fig. 1b, right**). The head-mounted eye tracking system was built based on a previous design by Meyer et al. (2018), and consisted of a Raspberry PI camera, an infrared (IR) LED and an IR mirror. Eye tracking movies were recorded with a resolution of 640 × 480 pixels and a frame rate of 90 Hz onto the Raspberry Pi.

To allow capturing eye position and pupil size in darkness under IR illumination, we first removed the IR filter from the sensor of the Raspberry PI Spy camera (**Table 1**, part #7). The camera was then glued into a 3D printed frame, which was designed and rendered with Blender (`https://www.blender.org/`), prepared using Cura (Ultimaker; `https://ultimaker.com/`), and printed with polylactic acid (PLA) on an Ultimaker 3 Extended 3D printer. The frame consisted of a back plate covering $\sim 2/3$ of the length of the camera and two side clamps for sliding the camera into the frame. On the top left edge of the frame, a small cube (2 × 2 mm) with a hole was used to attach a needle holding the infrared mirror (**Fig. 1b, right**).

The infrared mirror (NIR-blocking filter CALFLEX X SP, Qioptiq, UK; **Table 1**, part #8) was cut with a glass cutter into small pieces, with edge lengths of around 5–7 mm. After gluing the piece of mirror onto a small (1 × 4 mm) 3D printed tube, it was mounted on a syringe needle

(Gauge 21). The needle was then bend 90° in the middle, and its tip was inserted into the hole of the cube attached to the camera frame. During implantation of the camera holder, the mirror could be moved along the needle and rotated around it to ensure optimal positioning. The final position of the mirror was determined in a session under head-fixation, which took place after recovery from surgery and habituation to the setup and head-fixation (2 weeks post surgery). After ensuring that the camera still captured a clear and centered image of the eye, the mirror was fixed with superglue to the needle. In this session, also the focus of the camera was adjusted, by moving the lens in its thread, before gluing it in its optimal position.

To illuminate the eye, an IR LED (Osram, SFH 4726S, Mouser Electronics, USA; **Table 1**, part #9) was glued to the bottom of the right clamp of the frame around the camera. The LED was angled towards the camera and downwards, to avoid direct reflection of the light on the mirror into the camera. The LED was powered by a Raspberry Pi single-board computer (Raspberry Pi 3 model B, Raspberry Pi Foundation, UK; **Table 1**, part #10).

The entire eye-tracking camera system was glued on an aluminum cap that tightly fitted the implanted camera holder, whose non-symmetrical pentagon shape allowed only one particular orientation of mounting the system on the animal's head (**Fig. 1b, left**). The cap was fixed to the implanted camera holder by sliding a groove over the screw at the posterior side and clamping the cap by the screw-head. Clamping the two aluminum pieces with the screw secured them in a stable position over recording sessions.

Visual stimulation

Visual stimuli were generated using custom written software in Matlab (Mathworks) within the Psychophysics Toolbox framework (Brainard, 1997; Kleiner et al., 2007). The timing of individual monitor frames was controlled by a DATAPixx input/output (I/O) hub (DATAPixx2, VPixx Technologies, Inc., Canada). This I/O hub also acquired the additional data streams and/or their timing, i.e. an analogue input representing the speed of the linear treadmill, and a TTL input signaling the acquisition time of each eye tracking camera frame. This TTL signal was sent by the Raspberry Pi that acquired the eye tracking camera frames, using the Python package `rpicamera` (Meyer et al., 2018).

Spatial undistortion

For spatial undistortion of the visual stimuli projected into the dome, we determined a warping mesh. To this end, we displayed a polar grid whose pole was positioned at the far center of the dome, in front of the animal. The polar grid consisted of movable points at the intersection of the concentric circles radiating out from the pole and the spokes of the grid. User interaction with these

points of the grid was provided by a modified version of the function `DisplayUndistortionBVL.m` (Brainard, 1997; Kleiner et al., 2007). To span 240° in the dome, we used a grid with 8 circles and 24 spokes, with a dot spacing of 15°.

To determine the expected coordinates of the polar grid on the dome surface, we developed a tool to precisely and reversibly indicate polar angles from the center of the sphere, i.e. the position of the mouse's head. This tool consisted of a laser pointer (**Table 1**, part #1) mounted in the center of the dome on three rotatable platforms (**Table 1**, parts #2 and #3), such that it could be rotated around three axes. Additionally, the device was attached to a rail system (**Table 1**, parts #4–#6), which made it possible to keep the vertical and horizontal position of the laser pointer constant despite the change in angles. We used a pendulum of 60 cm length, i.e., the radius of the dome, hanging from the zenith, to re-calibrate the vertical and horizontal position of the laser pointer after rotations. One dot at a time, we positioned the laser pointer to indicate the expected angular position on the surface of the dome, and then manually dragged the corresponding point of the polar grid (in user interaction) to its correct location (indicated by the laser spot on dome surface). Original and corrected pixel coordinates of the calibration points, and information about which dots were moved, were saved in a `.mat` file. This calibration file was subsequently called by a built-in function of Psychtoolbox, `CreateDisplayWarp.m`. The routine `GeometryCorrection` then applied the interpolated warping mesh to stimulus textures, thus producing stimuli with correct appearance.

Experiments

To measure the pupillary light reflex (PLR; **Fig. 2**), a full-screen uniform stimulus, either UV or green, was presented in 11 intensity steps between 0 and 100%. One trial consisted of one intensity presented for 30 s, which was repeated 3 to 5 times in pseudorandom order.

For eliciting the optokinetic reflex (OKR; **Fig. 4**), a full screen drifting square-wave grating was presented. Six different gratings (spatial frequency 0.0625, 0.125, 0.25 cyc/°; temporal frequency 0.75, 1.5, and 3 cyc/s) were presented in 90° (vertical) orientation, in either clockwise or counterclockwise directions. Gratings were shown in a pseudo-random order for 1 s with an inter-trial interval of 1.5 s. Each of the 12 different conditions were repeated 50 times.

Natural movies were taken from our published open-source dataset (Qiu et al., 2021). Briefly, movies (180° FOV) were acquired, with a hand-held UV- and green-sensitive camera mounted on a gimbal, at a resolution of 437x437 pixels and with a frame rate of 25 frames/s. When moving the camera during the recordings, an azimuth angle of $\sim 60°$ between the optical axis of the fisheye lens and the movement direction was maintained, mimicking the position of the mouse eye (Stabio et al., 2018; Oommen and Stahl, 2008). In addition, the camera was held such that the horizon bisected the camera's visual field in elevation. From this dataset (Qiu et al., 2021), we randomly selected

166 movie snippets of 10 s duration, which had been acquired during daytime and which had a mean pixel intensity across colors between 30 and 100 (out of a maximal intensity of 255). In experiments assessing eye position and saccades during naturalistic stimulation, these 166 movie snippets were presented in two types of blocks (**Fig. 5a**). The blocks contained either the same 6 movie snippets, repeated twice per block ("Fixed block") or 20 random movie snippets ("Random block"). These two types of blocks occurred in an alternating fashion, with five fixed blocks and four random blocks in one session. Four experiments were conducted with three of the six movie snippets in the fixed blocks being shown upside down, to create an unnatural distribution of chromatic input. Before and after a session, the dome was illuminated for 10 min with the mean pixel intensity for UV (57) and green (61) of all individual movie snippets ("Blank block"). Mice typically performed two sessions per day. The movies were presented in the dome centered at 60° azimuth, i.e. mimicking the angle during acquisition, and with a frame rate of 60 Hz.

Data analysis

Pupil position and size, eye corners, and LED reflection position were extracted from each frame acquired by the eye tracking camera using the open-source software package DeepLabCut (Mathis et al., 2018). To train the deep convolutional network via transfer learning, we manually labeled $60 - 80$ frames per animal. Labeling entailed placing markers on the anterior and posterior eye corner, and on the edge of the pupil, using serrations as landmarks whenever possible (8 pupil markers in total). The network then assigned a likelihood value to each marker in each frame.

For all further analyses, custom code written in Python 3.6 was used. Frames in which one or more pupil markers had a likelihood < 0.99 were excluded and fitted values (see below) were linearly interpolated. For the experiments testing the PLR and the OKR, we additionally removed the ± 10 adjacent frames, as a conservative approach to reduce any artifacts in the estimation of pupil size and position. The markers around the pupil were fitted with a 2D ellipse using the scikit image class `EllipseModel`. The fit yielded parameters cx, cy, i.e. the coordinates of the ellipse center, a, b, i.e. the length of the major and minor axis, and θ, i.e. the orientation of the ellipse. We calculated pupil area in pixel as $area = \pi ab$.

We calculated the pupil position relative to the midpoint of eye corners (coordinate origin) (Meyer et al., 2020), and rotated the pixel coordinate system, such that the line connecting anterior and posterior eye corners was horizontal. For the right eye, we defined positive along the horizontal axis to point away from the nose (posterior), and positive along the vertical axis to point upwards (dorsal). For each session, we determined the median distance between the two eye corners and assumed it to equal 3.25 mm, i.e., the default distance between the eyes of the mouse (Schmucker and Schaeffel, 2004; Wisard et al., 2010). Using this conversion from pixels to millimeters, we could estimate the position of pupil in mm (P_{mm}) and the area of pupil in in mm^2. Furthermore,

we assumed the effective rotation radius of the mouse pupil (r_{mm}) to be 1.25 mm (Remtulla and Hallett, 1985; Sakatani and Isa, 2004), which allowed us to estimate the pupil position in rotation degrees (P_{deg}) using $P_{deg} = \arcsin(P_{mm}/r_{mm})$ (Sakatani and Isa, 2004). Limitations of this method to calculate eye position include: (1) As the camera sensor plane may not be perpendicular to the optical axis of mouse eye and the rotation center of eyeball, and the center of the cornea and the camera center may not be on the same line, the center of two eye corners may not be equivalent to the rotation center of eyeball on the camera image. (2) Also, the conversion from pixels to millimeters may differ for points on the image. Still, we deem these estimations reasonably accurate, as the size of eyeball is relatively small compared to the distance between the mouse eye and the camera.

For the analysis of pupil size during measurements of the PLR, the first 10 s of each trial were excluded, to focus on the steady-state part of the response to the luminance change. For each experiment, the mean pupil area per condition was fit with a sigmoidal fit as

$$f(x) = b + A \cdot \frac{1}{1 + e^{(-k \cdot (x - x_0))}} \tag{3}$$

where the parameters b capture the baseline and A the overall amplitude. x_0 denotes the center of the sigmoid function, and k represents the slope. For each session and color separately, we computed the amplitude of the sigmoid fit and the 63 decay.

For the analysis of the OKR, we followed methods originally proposed by Tabata et al. (2011). Specifically, for all trials, the horizontal velocity of the pupil was aligned to stimulus onset, after excluding all trials with a saccadic eye movement (acceleration $> 200°/s^2$) during the first 400 ms. The velocity traces were smoothed with a digital Butterworth filter (3rd order, sampling frequency = 90 Hz, lowpass, cut-off frequency = 5 Hz). To determine the latency of the OKR, for each trial, we computed eye velocities in windows of 25 ms and used a receiver operating characteristic (ROC) analysis, quantifying to which degree the distributions of eye velocities during counterclockwise and clockwise visual motion deviated (Tabata et al., 2011). For each time-point, AUROC (area under the ROC curve) values were computed and fit with a cumulative Weibull distribution:

$$f(x) = p - (p - q) \cdot e^{(-(\frac{x}{r})^s)} \tag{4}$$

The latency of the OKR was defined as the first time at which the Weibull fit first crossed $y = 0.75$ (Tabata et al., 2011).

For assessing the relationship between pupil size and frame intensity for natural movies, we calculated the mean intensity of each natural image frame by focusing on the pixels with y-coordinates $> -35°$ relative to the horizon, because lower elevations were not displayed on the dome surface. We used the Pearson's correlation coefficient to assess the relationship between mean intensity

across color channels of each frame and pupil size. To focus on the relationship between single color channels and pupil size, we used partial correlations to remove the effects of the other color channel. Here, the partial correlation ($r_{xy|z}$) of variables x and y given z is defined as:

$$r_{xy|z} = \frac{r_{xy} - r_{xz}r_{yz}}{\sqrt{(1 - r_{xz}^2)(1 - r_{yz}^2)}} \tag{5}$$

where r_{xy} represents the Pearson correlation between x and y. To test whether the two partial correlations (UV vs. green with pupil size) differed significantly, we subtracted the two partial correlation values in each session to get a pairwise difference. We then performed a two-sided, one sample permutation test for these differences against 0 (repeated 10,000 times) and calculated the resulting p value.

For the analysis of eye positions during movie experiments, we subtracted from each position the mean eye position across the two sessions recorded within a day for each animal. For all statistical tests related to eye positions, we performed two-sided one sample permutation tests against 0 with 10,000 repeats.

To analyze rapid eye position dynamics, we extracted saccades, which we defined as eye movements with absolute velocities (first derivative) $> 200°/s$ (Meyer et al., 2020; Zahler et al., 2021). We only selected one saccade with maximum peak velocity at each 50-ms time window (Meyer et al., 2020; Zahler et al., 2021). We defined the initial point and end point of each saccade as the first points, where the absolute velocity exceeded $30°/s$ and dropped below $20°/s$, respectively (Zahler et al., 2021). For all statistical tests related to saccades, we performed two-sided permutation tests for the medians of the distributions with 10,000 repeats.

Results

Hemispheric dome system with chromatic stimulation

To cover the majority of the visual field of the mouse and provide chromatic visual stimulation in relevant spectral bands, we built a hemispheric dome setup, which enables the presentation of wide-field stimuli in ecologically relevant colors (**Fig. 1**). In this setup, the mouse is head-fixed on a linear treadmill, such that its nose points to the front pole of the hemispheric screen and its head is positioned in the center of the sphere (**Fig. 1a**). A projector is placed behind and slightly below the screen and projects onto a quarter sphere acrylic mirror positioned centrally at the bottom of the dome (**Fig. 1a,c**). Eye position of the right eye of the head-fixed mouse is tracked by a head-mounted eye tracking system (**Fig. 1a,b**).

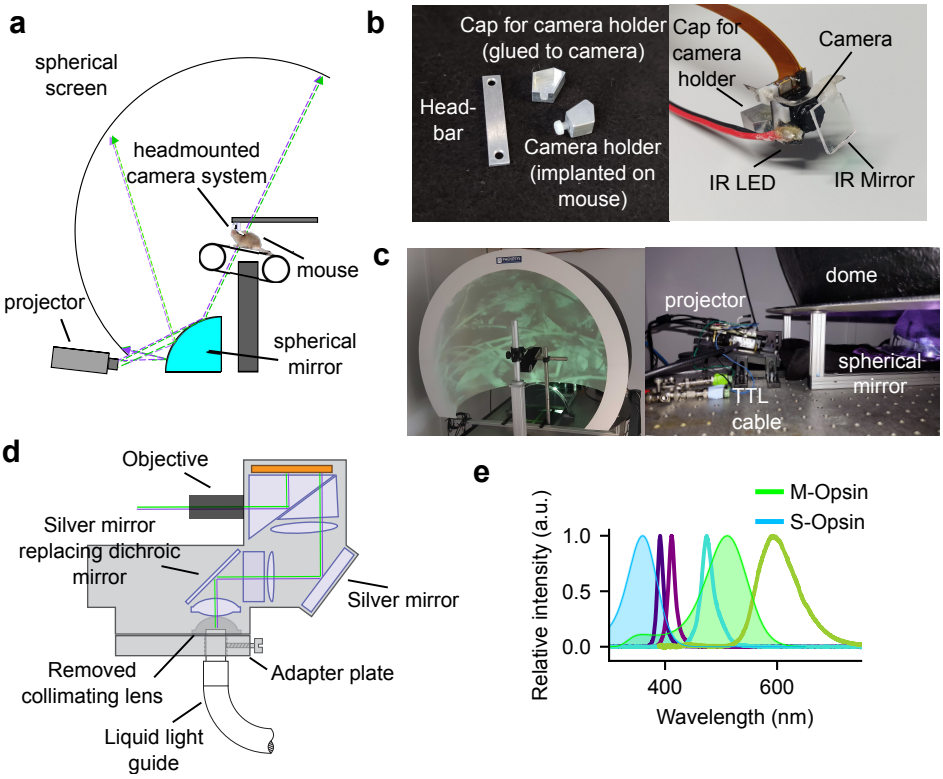

Figure 1 Hemispheric dome setup for visual stimulation and head-mounted camera system for eye tracking. (**a**) Schematic drawing of the dome setup with head-fixed mouse wearing the head-mounted camera system. (**b**) Implanted and removable parts of the eye tracking system. *Left*: The aluminum headbar next to the implanted pentagon-shaped aluminum camera holder (*bottom*) with a screw to clamp the cap holding the eye tracking system (*top*). *Right*: Front view of the head-mounted eye tracking system. (**c**) Dome and LC. *Left*: Back view of the dome setup with the LC projector, spherical mirror, and linear treadmill. *Right*: The LC connected to the liquid light guide and two output cables to trigger the UV and green LEDs of the light source and mounted on an angled platform. (**d**) Optical light path of the LC and custom modifications. (**e**) Spectra of LEDs used for UV and green stimulation from the 6-channel high intensity light source (Chrolis, Thorlabs; normalized intensities) and spectra of S- and M-opsin sensitivities of the mouse retina.

As stimulus projector, we used the light guide port version of the DLP LightCrafter 4500 (LC, Texas Instruments) (**Fig. 1c,d**). Because we found that this LC model only passes a fraction of the light guide's output (see also Franke et al., 2019), we took several measures to increase the light intensity available for illumination of our dome. We performed several custom-modifications of the LC (**Fig. 1d**): Firstly, we stabilized the connection of the liquid light guide (LLG) with an additional adapter plate, which allowed fixating the LLG in the optimal position with a screw. Secondly, we removed the first collimating lens to ensure brighter illumination of the mirror. Thirdly, we replaced the first dichroic mirror by a silver mirror that reflects all relevant wavelengths. In total, these modifications increased the transmission of light through the LC from 6% to 22% (measured at 520 nm). In addition, we chose a 6-channel high-intensity LED source (Chrolis, Thorlabs),

which allowed to combine two UV LEDs (385 nm and 405 nm) and two green LEDs (475 nm and 590 nm) with different peak wavelengths for the stimulation of the UV and green mouse cone opsins, respectively (**Fig. 1e**). Translating the measured power of UV and green as experienced from the center of the dome into photoisomerization rates, we found our illumination provided a virtual environment at photopic conditions, with the UV LEDs activating S-opsin up to 28,000 photons/s/cone and the green LEDs activating M-opsin up to 98,000 photons/s/cone .

To verify that the illumination intensity of the dome after modifications of the LC was sufficiently bright to evoke a physiological response from our mice, we measured the pupillary light reflex (PLR, **Fig. 2**). The PLR adjusts the size of the pupil based on light intensity and thus regulates the amount of light entering the eye, with brighter light causing pupil constriction and darker light causing pupil dilation (Pennesi et al., 1998). In mice, the PLR can be driven to the same extent by both UV and green light (Yao et al., 2006). We equipped a head-fixed mouse with the head-mounted eye tracking camera, and monitored the pupil size of the right eye in response to full screen green or UV stimuli of different intensities (**Fig. 2a**). For both green and UV stimulation, we observed pronounced decreases of pupil size with increasing light intensity (**Fig. 2b–c**). The robust negative relationship between pupil size and light intensity could be characterized by a sigmoidal relationship in all animals and sessions (**Fig. 2c**), where the pupil varied, on average, by 2.0 mm^2 for green and 1.4 mm^2 for UV across the entire range of light intensities. In addition, we found that the light intensity where pupil size was constricted to 63% of its fully dilated value, was 42% of the maximal intensity for green and 71% for UV. Notably, for the brightest intensity achieved, pupil size still seemed considerably larger for UV (1.6 mm^2) than for green (0.8 mm^2). Possible reasons for the reduced response of the PLR to UV could be the limited transmission of UV light through the projector, in combination with additional loss during reflection from the mirror and the dome surface (see Methods). Note, however, that such differences in overall light intensity are also present during natural daylight, where the light intensity in the UV range is lower than in green light (Warrant et al., 2020; Qiu et al., 2021). Together, these results show that the illumination of the dome with both green and UV was sufficient to consistently elicited the PLR across a range of intensities.

Spatial calibration for patterned visual stimulation

Besides achieving extensive coverage of the visual field at sufficient light intensity, a second major goal for the development of our dome setup was the ability to present arbitrary patterned visual stimuli (**Fig. 3**). In our system, the projection of a 2D stimulus onto the curved screen of the dome is accomplished through projection on a spherical mirror (Bourke, 2005), which can reflect light over the entire surface of the dome given its light-diverging properties (**Fig. 1a**). However, such projection also entails substantial, setup-specific distortions, such that for images on the dome surface to be displayed with correct appearance a transformation matrix is required (**Fig. 3a**)

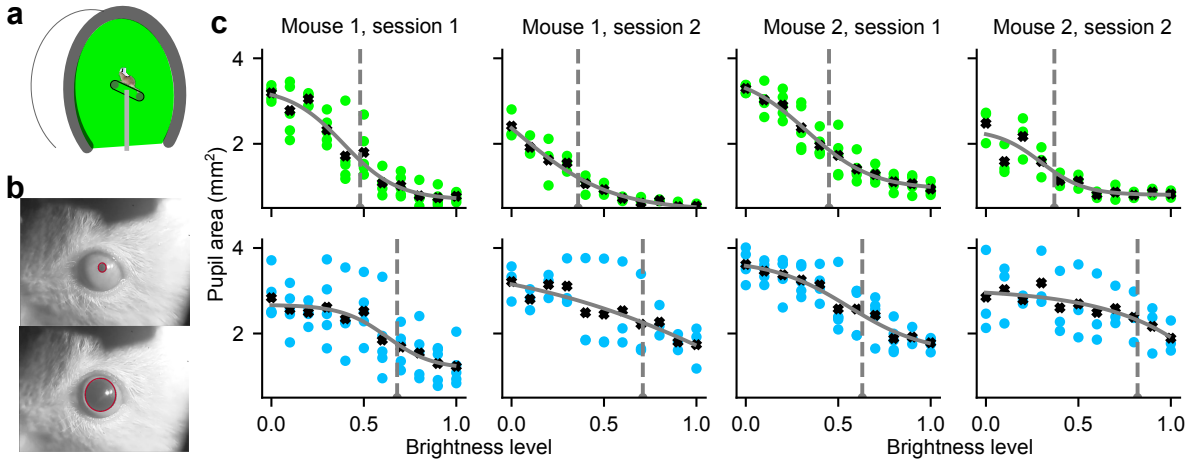

Figure 2 Confirmation of sufficient light intensity based on the pupillary light reflex. (**a**) Schematic drawing of the experiment: Pupil size was measured with a head-mounted eye tracking system in head-fixed mice in response to full-screen UV or green stimuli at different intensities. (**b**) Two representative video frames with fitted pupil outline (*red*) in response to 100% (*top*) and 0% (*bottom*) green light. (**c**) Pupil area as a function of light intensity for the green (*top*) and UV LEDs (*bottom*); 2 animals, 2 sessions each. *Colored dots*: single trials, *black crosses*: mean across trials; *gray line*: sigmoidal fit; *gray dashed line*: Light intensity where pupil area decayed to 63% of the fully dilated value.

(Bourke, 2005). Such transformation matrix specifies the relationship between any point on the 2D flat stimulus and any point on the dome, given the particular projector, mirror, and dome arrangement. Obtaining such a transformation matrix requires a calibration step which is commonly referred to as "mesh-mapping" (Bourke, 2005; Lopes et al., 2021; Shapcott et al., 2022).

To obtain a warping mesh specific to the distortions in our setup without prior assumptions of the underlying geometry or stimulus input, we developed an empirical calibration routine, which involved manually moving the texture coordinates (u, v) to the appropriate spherical coordinates (r, θ, ρ). A stimulus that is well-suited for this purpose is a polar grid (**Fig. 3b**), as its correct appearance in the hemispheric dome setup is known (Bourke, 2005). Projecting the pole of the grid to the far side of the dome in front of the animal, the horizontal spoke of the grid should encircle the equator of the dome, and all concentric circles of the grid should be spaced regularly around the front pole in the dome (Bourke, 2005). We used a grid with 24 spokes and 8 circles, to achieve 15° visual angles between the spokes and a coverage of 240° (**Fig. 3b and e**; for illustration purposes, only 12 spokes are shown). We displayed the intersections between the spokes and concentric circles in the polar grid as dots, which served as anchor coordinates for the calibration, because they can be easily expressed in spherical coordinates (r, θ, ρ) (see also Yu and Rosa, 2010) (**Fig. 3e**).

To precisely determine the location of the anchor coordinates in spherical coordinates on the dome without attaching permanent markers that might potentially interfere with the visual stimulus, we aimed a laser pointer, which was mounted on a platform allowing rotations along three

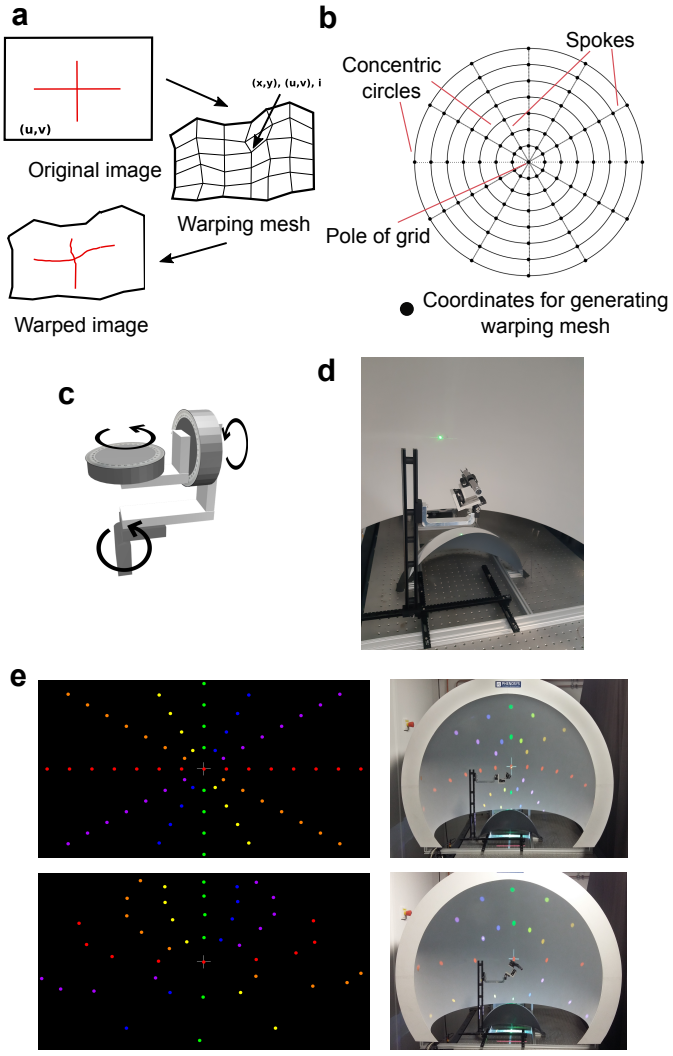

Figure 3 Spatial calibration of the hemispheric dome setup. (**a**) Principle of "mesh-mapping": an image texture with coordinates (u, v) (*top*) is applied to a warping mesh (*right*), where each node is defined by a position (x, y) and texture coordinate (u, v). The warping (*left*) ensures an undistorted appearance on an arbitrary surface (adapted from: http://paulbourke.net/dataformats/meshwarp/). (**b**) Polar grid used for calibration. The pole of the grid was projected to the front center of the dome, and dots at the intersection of the concentric circles and spokes radiating from the pole were used as coordinates for generating the warping mesh. (**c**) Calibration device with 3 axis of rotation. (**d**) Calibration device mounted on rails to change its position in the sphere, allowing to keep the laser pointer tip in the center of the dome during rotations. (**e**) Polar calibration grid prior to calibration (i.e. without "mesh-mapping") rendered on a flat screen (*top, left*) and in the dome (*top, right*). Polar calibration grid after "mesh-mapping" rendered on a flat screen (*bottom, left*) and in the dome (*bottom, right*); for illustration purposes only, the grid contained colored dots and had a 30° spacing.

axes, to specific polar coordinates on the dome's surface (**Fig. 3c,d**). We then dragged each of the colored dots at the anchor coordinates to their expected angular position, which resulted in a

set of corresponding points between the spherical coordinates (θ, ρ), the original image coordinates (u, v), and the new position of the node (x, y).

As expected, projecting our polar grid (**Fig. 3e, *top left***) prior to calibration onto the dome resulted in a distorted appearance (**Fig. 3e, *top right***). After the calibration procedure and application of the warping mesh to the grid's texture (**Fig. 3f, *bottom left***), the projected grid had the correct appearance in the dome (**Fig. 3f, *bottom right***), with straight lines and regularly-spaced circles.

Rotating stripes in the dome evoke the optokinetic reflex (OKR)

Having established methods for rendering patterned visual stimuli with correct appearance, we next sought to validate that visual stimulation in our setup can, in principle, evoke stimulus-related eye movements. To this end, we relied on measuring in head-fixed mice the optokinetic reflex (OKR), i.e. compensatory eye movements in response to large-scale retinal slip (Land, 2019).

We presented full screen, vertical gratings rotating either clockwise or counterclockwise and monitored eye position with our head-mounted, camera-based eye tracking system (**Fig. 4a**). As expected from earlier studies (Prusky et al., 2004; Stahl, 2004; Tabata et al., 2011), we observed that eye position varied systematically with the direction of rotation (**Fig. 4b**). Specifically, we found that eye movements to the sustained grating rotation consisted of alternating patterns of slow movements following the direction of the grating and fast, resetting movements (**Fig. 4c**). Focusing on those trials without a saccade in the first 400 ms after grating onset, we calculated eye velocity (**Fig. 4d**) and analyzed how the latency and size of the evoked eye movements depended on the temporal and spatial frequency of the rotating grating. To assess the consistency of the evoked eye motion, we combined all trials across all sessions and all animals (**Fig. 4d**) and performed a ROC analysis for each time point (Tabata et al., 2011), comparing the distributions of single trial velocities between clockwise and and counterclockwise grating rotations. We found that all three stimulus conditions reliably elicited the OKR, with latencies (first AUROC > 0.75) of 117 ms, 111 ms, and 122 ms for the three stimulus conditions, respectively (**Fig. 4e**). Together, these analyses of the OKR show that, in our dome setup, we can reliably observe stimulus-driven eye movements with the expected latency.

Naturalistic movies elicit systematic changes in pupil size and eye position

Having established that, in principle, we can elicit and track stimulus-evoked changes in pupil size and position, we next turned to more naturalistic visual stimulation (**Fig. 5**). More specifically, we displayed UV/green movies of outdoors scenes, which we had taken in presumed mouse habitats with a hand-held, custom camera mimicking some key aspects of the mouse visual system (Qiu et

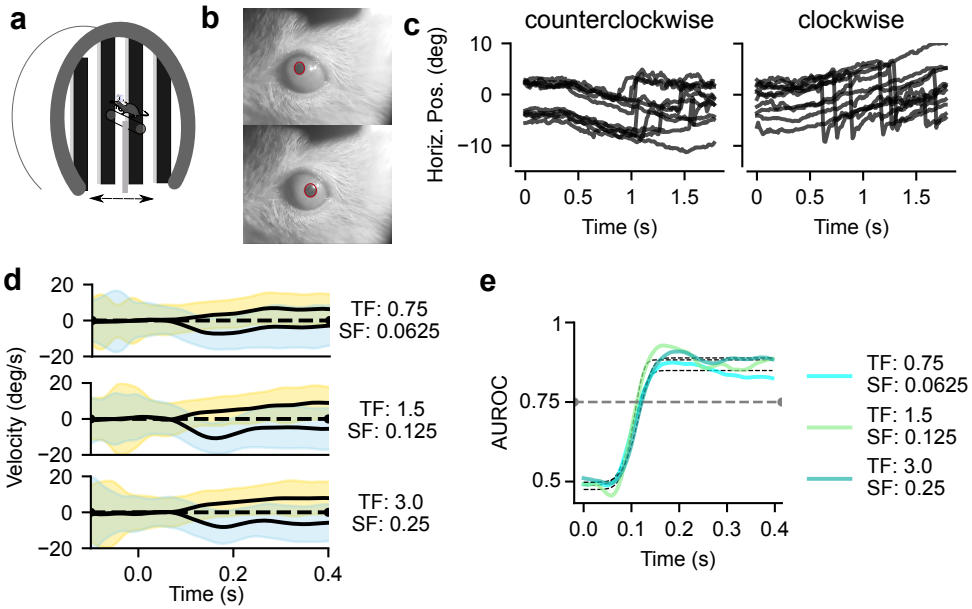

Figure 4 OKR measurements in the dome as a principled test for evoking eye movements in head-fixed mice. (**a**) Schematic illustration of the experiment. (**b**) Two representative video frames captured by the head-mounted eye tracking system. *Red*: fitted pupil outline. (**c**) Eye position relative to stimulus onset in one example condition (TF 1.5 cyc/s, SF: 0.125 cyc/deg). *Left*: counterclockwise grating rotation; *right*: clockwise grating rotation. (**d**) Eye velocity for all trials in all sessions (n = 7610 trials), separately for trials with clockwise (*blue*, standard deviation) and counterclockwise rotation (*yellow*). *Black trace*: trial-averaged means. (**e**) Timepoint-by-timepoint AUROC values for the three stimulus conditions (*colored lines*) with Weibull fit (*black dashed lines*) for the extraction of latency. *Gray line*: AUROC = 0.75.

al., 2021).

An experimental session consisted of several blocks of visual stimulation (**Fig. 5a**). It started and ended with a 10 min block, in which the dome was illuminated with the overall mean intensity across all individual movie frames ("Blank block"). In between, we presented blocks containing several 10 s movie snippets. These blocks consisted of either the same 6 movie snippets ("Fixed block") or 20 random snippets ("Random block"), and occurred in an alternating fashion.

We first analyzed pupil size (**Fig. 5b**), hypothesizing that the PLR should also be elicited by fluctuations of brightness in our naturalistic movies. To validate that pupil size tracked average brightness of the movie frames, we first concentrated on the blocks containing the six repeated movie snippets. Plotting pupil size aligned to the onset of the "Fixed block" in an example session indeed revealed a pattern of consistent fluctuations of pupil size, occurring between movie segments, e.g., around the transition between the first and second snippet, but also within movie segments, e.g., around the middle of the fourth snippet (**Fig. 5b**). We quantified the relationship of pupil size and average brightness by correlating the pupil size traces across pairs of trials, and found that for this session, the pair-wise average correlation was $r = 0.52 \pm 0.21$ (std). In contrast, performing

the same analysis for a randomly selected subset of 6 movie snippets from the "Random block" yielded a correlation of $r = 0.01 \pm 0.3$ (**Fig. 5c**). Repeating this analysis for all sessions (n = 22 sessions from 3 mice), we found an average correlation of $r = 0.37$, which was significantly different from the correlation obtained with random luminance input ($r < 0.001$) (two-sided one sample permutation test of the difference against 0, $p = 0.0009$; **Fig. 5d**).

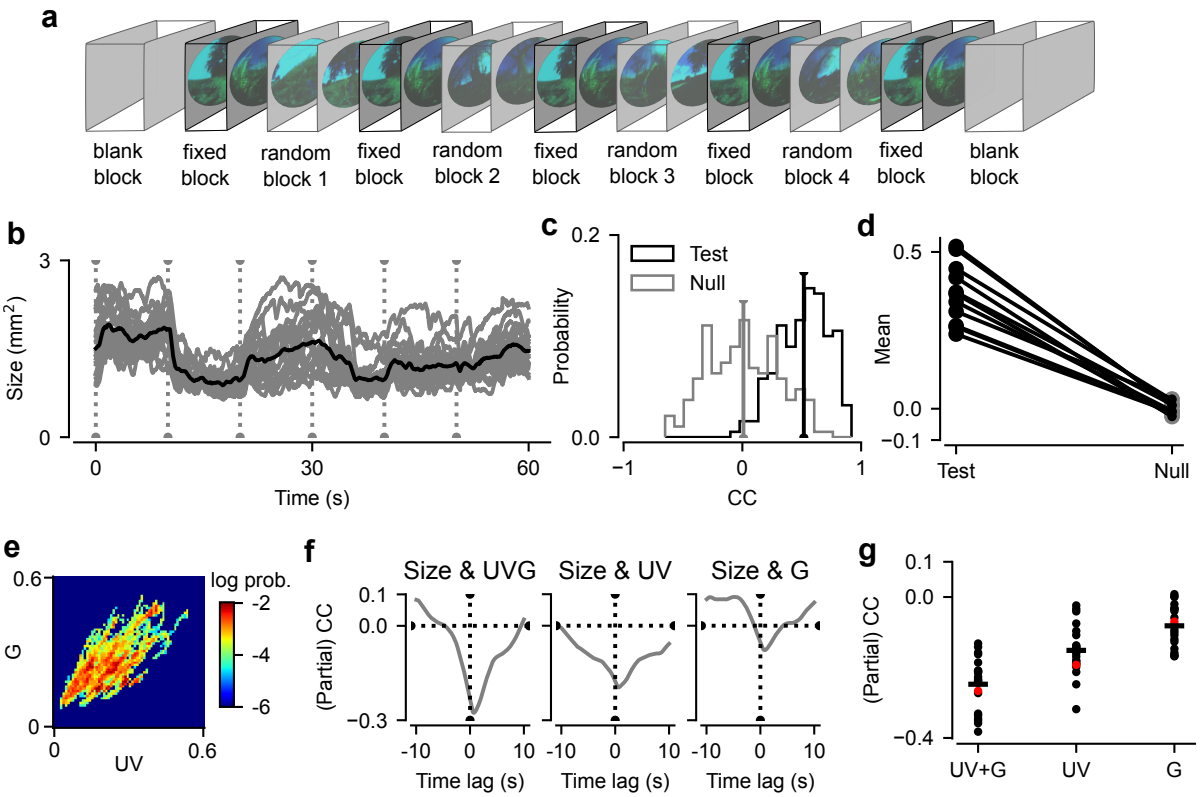

Figure 5 During viewing naturalistic UV/green movies, pupil size tracks average intensity of the movie frames. (**a**) Schematics of an experimental session. 4 blocks of 20 random movie snippets of 10 s duration ("random" block) were interleaved with a block of 6 repeated movie snippets ("fixed" block). Movies were flanked by a 10 min period of blank screen of average luminance ("blank" block). Mice performed two sessions per day. (**b**) *Gray*: Pupil size as a function of time during the "fixed" block; example animal in one day (2 × 5 repeats). *Black*: mean across repeats; *dashed vertical lines*: transitions between 10 s snippets. (**c**) Distribution of Pearson correlation coefficients for pairs of pupil size traces in (b) (test; *black*) and for randomly selected 60 s snippets from "random" blocks (null; *gray*). *Vertical lines*: means. (**d**) Mean test and null correlations (n = 22 sessions from 3 mice). (**e**) 2D histogram of mean UV and green intensities for all movie frames. (**f**) Cross-correlation between pupil size and intensity of movie frames for one example session, for both color channels combined (*left*), and partial correlation between pupil size and intensity in UV (*middle*) and green (*right*), given the intensity in the other color channel. (**g**) Correlation between pupil size and frame intensity at 0.4 s lag (Grozdanic et al., 2003; Lucas et al., 2001) across all sessions (*dots*). Like in (f), partial correlations were used for the relationship between pupil size UV and green. *Horizontal bars*: means, *red*: examples shown in (f).

Having naturalistic movies that contain intensity fluctuations in both UV and green, we next

asked whether the observed variations in pupil size were more strongly driven by one or the other color channel. To this end, we included all movie snippets and calculated the cross-correlation between pupil size and average intensity of each frame, either combined or separately for UV and green. Because UV and green intensity is correlated in natural scenes, including our own footage (**Fig. 5e**), we focused on partial correlations, i.e. correlations between pupil size and intensity, which could not be explained by the other color channel. For all three conditions (both colors, UV and green), we extracted the cross-correlation at a typical lag of the PLR of 0.4 s (Grozdanic et al., 2003; Lucas et al., 2001) (**Fig. 5f**), and found a negative cross-correlation between the mean intensity of our movie frames and pupil size (-0.27 [UV+green combined], -0.19 [UV] and -0.07 [green]), indicating that the pupil constricted shortly after an increase in intensity. We observed similar relationships for all sessions, and found a stronger correlation between pupil size and the UV light vs. the green light (average values -0.25, -0.15 and -0.08 for both colors, UV and green; UV vs. green, one sample permutation test of the difference against 0, $p = 0.0058$; **Fig. 5g**). Taken together, our results demonstrate that the head-mounted eye tracking system in our dome can capture consistent changes in pupil size in response to our naturalistic UV/green movies.

Beyond exhibiting changes in pupil size consistent with the pupillary light reflex, do head-fixed mice make specific adjustments of eye position in response to our naturalistic movies? It is well known that primates use saccadic eye movements to target salient visual information with the fovea, and thus explore visual scenes with predictable and repeatable paths of eye movements even during free exploration (Yarbus, 1967). Similar eye movements to target specific objects are not expected for mice or other animals with a more uniform distribution of spatial acuity (Land, 2015). We therefore first confirmed the absence of systematic eye movements to the repeated snippets of our movie stimulus (**Fig. 6a**). Aligning horizontal (**Fig. 6a, left**) and vertical eye position (**Fig. 6a, right**) to the onset of the "fixed" blocks in an example session suggested that there were indeed no consistent patterns of eye movements across repeats. While we could not observe consistent patterns of eye movements across repeats, we found that, similar to prior reports (e.g., Sakatani and Isa, 2007; Meyer et al., 2020), head-fixed mice generally made more horizontal than vertical eye movements (**Fig. 6a**). We quantified this by computing the distribution of horizontal and vertical eye positions during movie viewing, and indeed found a wider spread along the horizontal (std = 4.24) compared the vertical axis (std = 2.56; **Fig. 6b, *top* vs. *bottom*, red**). Similar findings were obtained across all sessions and animals (mean std for horizontal 3.96 vs. vertical 2.21; one sample permutation test, $p < 0.0001$).

Having confirmed that head-fixed mice do not make targeted eye movements under our stimulus conditions, we next asked whether viewing of our naturalistic movies affects general eye position. For instance, mice may adjust eye position, or the size and frequency of eye movements, to optimize visual processing of patterned, dynamic stimuli, such as movies, compared to conditions with uniform visual input (Samonds et al., 2019). To test this hypothesis, we computed distributions of eye position not only during stimulation with naturalistic movies, but also for the "blank blocks"

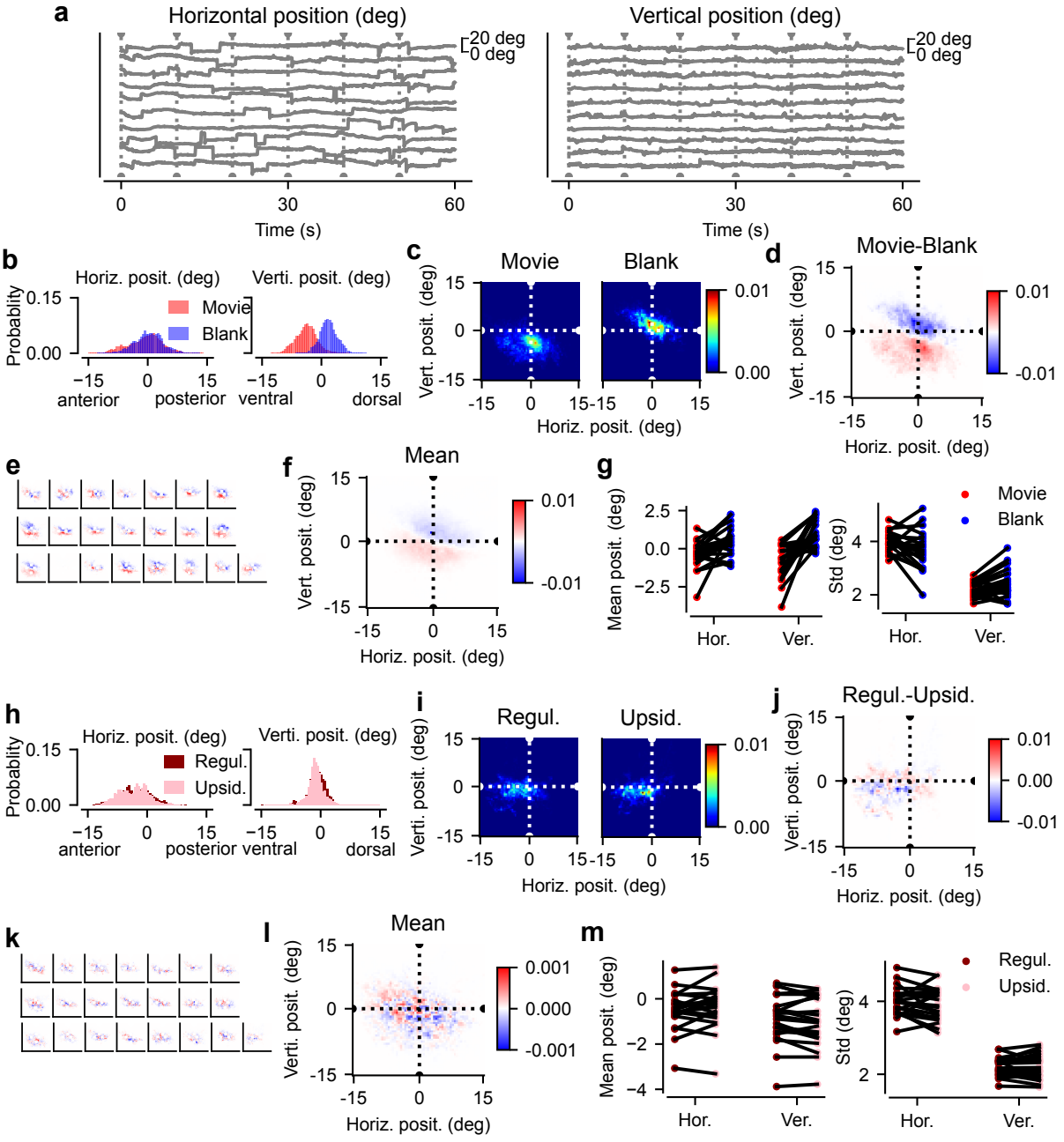

Figure 6 Eye position during naturalistic movie viewing. (**a**) Exemplary eye position traces for ten of the twenty repeats of the "fixed" movie blocks, separately for the horizontal (*left*) and vertical (*right*) axis. *Dotted lines*: start of individual movie snippets. Example session. (**b**) Distribution of horizontal (*top*) and vertical (*bottom*) eye positions during the same example session as shown in (a), separately for periods of movie viewing (*red*) and during presentation of an average gray screen during "blank" blocks (*blue*). (**c**) 2D representation of the distributions in (b). (**d**) Difference between of 2D distribution of pupil position from (c) during naturalistic movie viewing vs. gray screen ("blank"). [*Continued on next page*]

Figure 6 [*Continued*] (**e**) Same as (d), separately for all 22 sessions from 3 mice. (**f**) Same as (d,e), averaged across all sessions in (e). (**g**) Mean (*left*) and standard deviation (*right*) of horizontal and vertical eye position, separately for natural movie (*red)* and gray screen conditions (*blue*). Dots represent the 22 sessions from the 3 mice. (**h**) Distribution of horizontal (*top*) and vertical (*bottom*) eye position during the same example session as shown in (a), separately for periods with regularly oriented movies (*red*) and upside-down movies (*pink*). (**i**) 2D representation of the distributions in (h). (**j**) Difference between the 2D distribution of pupil position from (i) during regular and upside-down movies. (**k**) Difference of probability of pupil position of all 22 sessions from 3 mice. (**l**) Mean of difference of probability of pupil position between regular and upside down movies over all sessions. (**m**) Mean (*left*) and standard deviation (*right*) horizontal and vertical pupil position divided into regular and upside-down condition.

flanking at the beginning and end of the recording session (**Fig. 6b**). Analyzing the distributions of eye position in 2D, separately during naturalistic movies and "blank blocks" (**Fig. 6c**), we found that the average eye position during movies was more nasal and ventral ($(-0.64°;-3.83°)$, coordinates of center of mass), while for "blank blocks", the average eye position was more central and dorsal (0.25°;1.83°). Subtracting the 2D distributions of eye positions visualizes this separation (**Fig. 6d**).

We found a systematic shift in average eye position not only for the example session, but for each individual animal and session (**Fig. 6e**), and thus also for the mean difference across all sessions (**Fig. 6f**). Indeed, average eye position was $0.9 \pm 1.2°$ more nasal ($p < 0.0001$, two-sided one sample permutation test of the difference against 0) and $1.9 \pm 1.6°$ more ventral for movies compared to "blank blocks" ($p = 0.0006$; **Fig. 6g, left**). In addition, variability of eye position was slightly higher for "blank blocks" compared to movies, both along the horizontal (3.96 vs. 3.7 std, p = 0.075, one sample permutation test of difference against 0) and the vertical axis (2.21 vs. 2.41 std, p = 0.049; **Fig. 6g, right**). These differences in eye position and variability may be related to changes in overt behavioral state, as locomotion during movies was slightly more frequent compared to"blank blocks" (0.044 ± 0.017 m/s vs. 0.036 ± 0.010 m/s, $p = 0.0015$, one sample permutation test of difference against 0). Together, these results indicate that during viewing of our naturalistic movies, head-fixed mice adjust their average eye position to a more ventral and nasal position.

Finally, we asked whether overall eye position of mice also changed for more subtle differences in visual input. Specifically, we hypothesized that turning the movies upside down elicits specific changes in eye position as this manipulation reverses the vertical gradients of UV and green contrasts occurring in natural scenes (Qiu et al., 2021). To test this hypothesis, we presented the movies in half of the blocks upside-down and compared eye position between these blocks and blocks with "regular" movies. However, we did not find any systematic differences in horizontal or vertical eye position for upside-down compared to regular movies (**Fig. 6h-m**). Taken together, mice adjusted their eye position to more anterior and ventral positions when viewing our naturalistic movies compared to blank screens, but did not respond with eye position changes to more subtle

manipulations of the movies.

A special form of eye movements are saccades, i.e. rapid, conjugate eye movements, which in the mouse have amplitudes of $10 - 20^\circ$ and peak velocities reaching $1,000^\circ/s$ (Meyer et al., 2020; Sakatani and Isa, 2007). A previous study in head-fixed mice viewing natural scenes of different sizes suggested that saccade sizes could be predicted by stimulus statistics (Samonds et al., 2018). Encouraged by our stimulus-specific shifts in overall eye position, we next set out to test whether also saccadic eye movements differed between our visual stimulation blocks.

We detected the onsets of saccades separately for vertical and horizontal directions as eye velocities exceeding $200^\circ/s$ (**Fig. 7a, b**). In line with previous studies (Meyer et al., 2020; Samonds et al., 2018) and consistent with our analyses of general eye position, an inspection of the detected saccades revealed that they were more frequent along the horizontal axis (data not shown). Previously, it has been suggested that saccades in afoveate animals, like the mouse, might serve to refresh the visual input, and therefore it would be predicted that saccade rate and size should be increased for low-spatial frequency input (Samonds et al., 2018; Groner et al., 2008). Given the predominance of saccades along the horizontal axis, we first concentrated on horizontal saccades. We quantified the occurrances of saccades independent of differences in block duration by computing the intersaccadic interval (**Fig. 7c**, and found that the median intersaccadic intervals for movies (5.98 ± 13.42 s) and blank (6.78 ± 13.99 s) were overall somewhat larger than in the previous study by Samonds et al. (2018). In addition, our data suggests that intersaccadic intervals were slightly, but significantly shorter for movies than "blank" blocks ($p = 0.0089$, two-sided permutation test for the medians of the distributions; **Fig. 7c**). Furthermore, we found that while the median saccade size for movies ($8.33 \pm 5.03^\circ$ (std)) vs. "blank blocks ($8.09 \pm 3.51^\circ$) closely matched the previous study by Samonds et al. (2018), saccades during movies were slightly larger than those during "blank" blocks ($p = 0.024$; **Fig. 7d**). Taken together, under our visual stimulation conditions, saccade rate and size were largely similar in head-fixed mice viewing movies vs. uniform screens, with slightly more saccades of larger amplitude during movies.

To relate our analyses of saccadic eye movements to our previous results concerning general eye position, we last focused on the initial and end points of saccades and compared them between movie and "blank" blocks (**Fig. 7e-f**). Examining a single example session (**Fig. 7e**), and consistent with our results for overall eye position, we saw that the initial and end points for vertical saccades, in particular, were more ventral during movie vs. "blank" blocks (**Fig. 7e**). We could also recapitulate our results of general eye position differences in the analysis of saccadic initial and end points across sessions (**Fig. 7f**), where differences in the distributions were mostly consistent with a shift towards more frontal and ventral positions (**Table 2**).

Thus, saccadic eye movements bringing the eye to a more frontal and ventral position during movie than "blank" blocks might contribute to the overall shift of eye position towards more frontal and ventral areas for naturalistic movies.

Comparison	Movie	Blank	p-value
Initial points of horizontal posterior saccades	$-4.47 \pm 5.34°$	$-3.28 \pm 3.62°$	$p < 0.0001$
Initial points of vertical dorsal saccades	$-1.62 \pm 3.16°$	$0.43 \pm 2.91°$	$p < 0.0001$
End points of horizontal posterior saccades	$2.90 \pm 4.57°$	$3.65 \pm 3.70°$	$p = 0.003$
End points of horizontal anterior saccades	$-6.89 \pm 5.03°$	$-6.02 \pm 3.74°$	$p < 0.0001$
End points of vertical dorsal saccades	$3.56 \pm 3.81°$	$6.00 \pm 3.13°$	$p < 0.0001$
End points of vertical ventral saccades	$-0.80 \pm 7.45°$	$-3.16 \pm 5.64°$	$p < 0.0001$

Table 2 Comparisons for saccade initial and end points during movie vs. "blank" blocks

Discussion

In this work, we asked whether naturalistic visual stimulation can elicit systematic eye movements in mice, generally thought to perform eye movements mainly to stabilize the image on the retina rather than to scan the surroundings. To answer this question, we implemented a hemispheric dome setup capable of displaying visual stimuli in UV and green, the spectral bands relevant for the mouse, and covering most of the mouse's large field of view. We first provided proof-of-principle that our setup achieved sufficient light intensity in both spectral channels by demonstrating systematic decreases in pupil size with increasing light intensity, i.e the pupillary light reflex. In addition, we demonstrated that our setup is capable of eliciting systematic eye movements by assessing input-stabilization related responses to rotating gratings, i.e. the optokinetic reflex. We then turned to the presentation of naturalistic movies of outdoor scenes taken with a hand-held camera from the perspective of a ground dwelling animal. We found that head-fixed mice systematically change their eye position during viewing of the naturalistic movies compared to a mean luminance uniform gray stimulus towards more anterior and more ventral positions. While the occurrence and size of saccades was similar for both stimuli, saccades start and ended more anterior for movies, recapitulating the shift of general eye position. Together, this demonstrates that even under head-fixed conditions mice make specific adjustments of position according to the visual input. We suggest that these eye movements might serve to position certain aspects of the visual scene on specific parts of the retina, for instance to increase binocular coverage of the visual input in front of the animal.

To test whether eye movements and position in mice depends on the visual input, we built, inspired by previous work (e.g., Yu and Rosa, 2010; Lopes et al., 2021; Denman et al., 2017; Sibille et al., 2022; Shapcott et al., 2022; Gupta et al., 2022), a hemispheric dome setup, which covered large parts of the visual field of the mouse and allowed to present arbitrarily patterned UV- and green stimuli with sufficient intensity. In the future, to further improve the range of light intensity, in particular in the UV range, the acrylic mirror could be exchanged against a silver-coated mirror and the dome could be painted with UV-reflective paint (Denman et al., 2017; Sibille et al., 2022). Besides measuring behavioral and neuronal responses in head-fixed mice, a promising

further application could entail recordings in freely moving mice. This would require a modification of the dome interior to contain a platform, tracking of the animal's head, e.g. with an IMU (Meyer et al., 2020; Parker et al., 2022), and closed loop adjustments of the visual input based on the animal's position (Lopes et al., 2021).

Spontaneous saccadic eye movements in head-fixed mice are known to be rare (Niell and Stryker, 2010; Samonds et al., 2018; Meyer et al., 2020), occur mainly in the horizontal direction (Sakatani and Isa, 2007; Meyer et al., 2020), and seem to happen mostly during attempted head-movements (Meyer et al., 2020). Thus, instead of serving to scan the environment, eye movements in mice have so far mostly been attributed to stabilization mechanisms, compensating for body or head movements to keep the image on the retina fixed (Land, 2015; Meyer et al., 2020). Furthermore, in animals without a fovea, such as mice, another function of saccades could be that they de-correlate the input to the retina (Samonds et al., 2018). Consistent with this hypothesis, it has been found that the size and frequency of saccades in mice depend on the size of the visual input (Samonds et al., 2018). Under our visual stimulation conditions, comparing viewing of naturalistic movies and a gray screen, we did not find a difference in saccade size or frequency. However, the increased variability in general eye position observed in the gray screen condition would be consistent with the idea that, during viewing of a uniform stimulus, mice move the eyes more in an attempt to acquire novel inputs. Our finding of smaller variability in eye movements during movies compared to gray screen conditions is also reminiscent of studies in humans showing less frequent and smaller eye movements during viewing of dynamic than static visual scenes (Dorr et al., 2010). Arguably, a uniform gray screen and a dynamic naturalistic movie are at opposite ends of the spectrum in terms of several stimulus parameters. For future experiments it would thus be interesting to vary the visual stimulus in more fine-grained ways, e.g. by creating various types of noise, in order to test some of these interpretations and allow better comparison to the previous literature.

What could be the purpose of the systematic change in eye position that we observed during viewing of a naturalistic stimuli? While originally it was thought that the mouse retina contained topologically uniform functional feature selectivity, recent years have revealed several retinal specializations (reviewed in Sedigh-Sarvestani and Fitzpatrick, 2022). Arguably the best studied specialization in the mouse retina is the gradient of cone opsin expression, with a relatively uniform distribution of S-cones, and a dorso-ventral gradient of S-cone opsin co-expression in the M-cones (Szél et al., 1992; Baden et al., 2013; Nadal-Nicolás et al., 2020). This arrangement results in a strongly UV-sensitive ventral and a more green-sensitive dorsal retina, which closely mirrors the relative abundance of contrasts in natural scenes (Qiu et al., 2021), and thus seems to support the detection of dark contrasts in the sky, such as aerial predators (Qiu et al., 2021; Baden et al., 2013). While it is currently not known whether mice exploit specific visual cues to optimally align this gradient with respect to the visual scene, our observed stimulus-specific shift of eye position and the decrease in eye-position variance could potentially reflect such a visual input-based alignment process. Future experiments could test this idea more directly by systematically displacing the

naturalistic movies , and examining the consequences on the mouse's eye position.

In addition to the UV-green gradient, recent studies have shown that the mouse retina also contains regions of elevated density of specific ganglion cell subtypes (Bleckert et al., 2014; Warwick et al., 2018). For instance, alpha retinal ganglion cells seem to display a nasal-to-temporal gradient in cell density, size, and receptive fields, which might serve to enhance visual sampling of frontal space (Bleckert et al., 2014). In addition, in mouse visual cortex, neurons representing the lower visual field have been found to have greater sensitivity for binocular disparity (La Chioma et al., 2019, see also below) and to be more responsive to coherent motion (Sit and Goard, 2020). Thus, positioning the eyes in a more frontal and ventral position during viewing of naturalistic movies might direct higher-acuity processing resources to the field of view straight ahead, potentially to enhance responsiveness to optic flow in the lower visual field.

Besides alignment of the retina with specialized processing resources, another hypothesis for the observed shift of eye position to more anterior and ventral positions during movie viewing is related to the extent of the mouse's binocular visual field. Given the lateral placement of their eyes, mice have a large, panoramic field of view, and a much smaller binocular zone, which is sampled by both eyes. This binocular zone is relatively small in front of the animal, but widens to almost 90 deg in the upper visual field (Wallace et al., 2013; Samonds et al., 2019; Dräger and Olsen, 1980). Centering the eyes in a more forward and ventral position should increase the binocular overlap, in particular if such shift was performed by both eyes. Binocular vision, compared to monocular vision, has numerous advantages, ranging from improved sensitivity due to the duplication of inputs to the possibility of retrieving distance information from comparison of the image in the two eyes (Read, 2021). Accordingly, in mice contrast sensitivity is better for binocular compared to monocular stimuli (Speed et al., 2019), and neurons in binocular visual cortex are tuned to binocular disparities (La Chioma et al., 2019; Samonds et al., 2019; Scholl et al., 2013). To test more directly whether mice shift eye position during naturalistic movie viewing to increase binocular overlap, future versions of the experiment should monitor both eyes simultaneously.

Compared to head-fixed conditions, mice make much richer eye movements while freely moving (Meyer et al., 2020), and sample the visual environment with combined eye-, head- and body-movements (Meyer et al., 2020; Land, 2019). In particular, under freely moving conditions, when mice turn their head along the horizontal plane, the eyes move in a conjugate way, first in the opposite direction relative to the head to counteract the head turn, then rapidly following in the direction of the head turn, and finally compensating for the overshoot (Meyer et al., 2020, 2018). Together, these combined eye- and head-movements make the line of sight, or gaze, stable and then rapidly shift ("saccade and fixate pattern") (Land, 1999; Meyer et al., 2020; Michaiel et al., 2020). It has already been shown that mice execute such shifts of gaze during specific naturalistic behaviors, in particular prey capture: during approach phases in hunting, mice perform specific orienting movements to place the cricket prey into the binocular visual field just ahead (Hoy et al.,

2016; Michaiel et al., 2020; Holmgren et al., 2021). Whether such orienting movements also occur during free viewing of a visual scene akin to the stereotypical patterns of saccades and fixations observed in humans is an open question and could be tested with a modified version of our setup in the future.

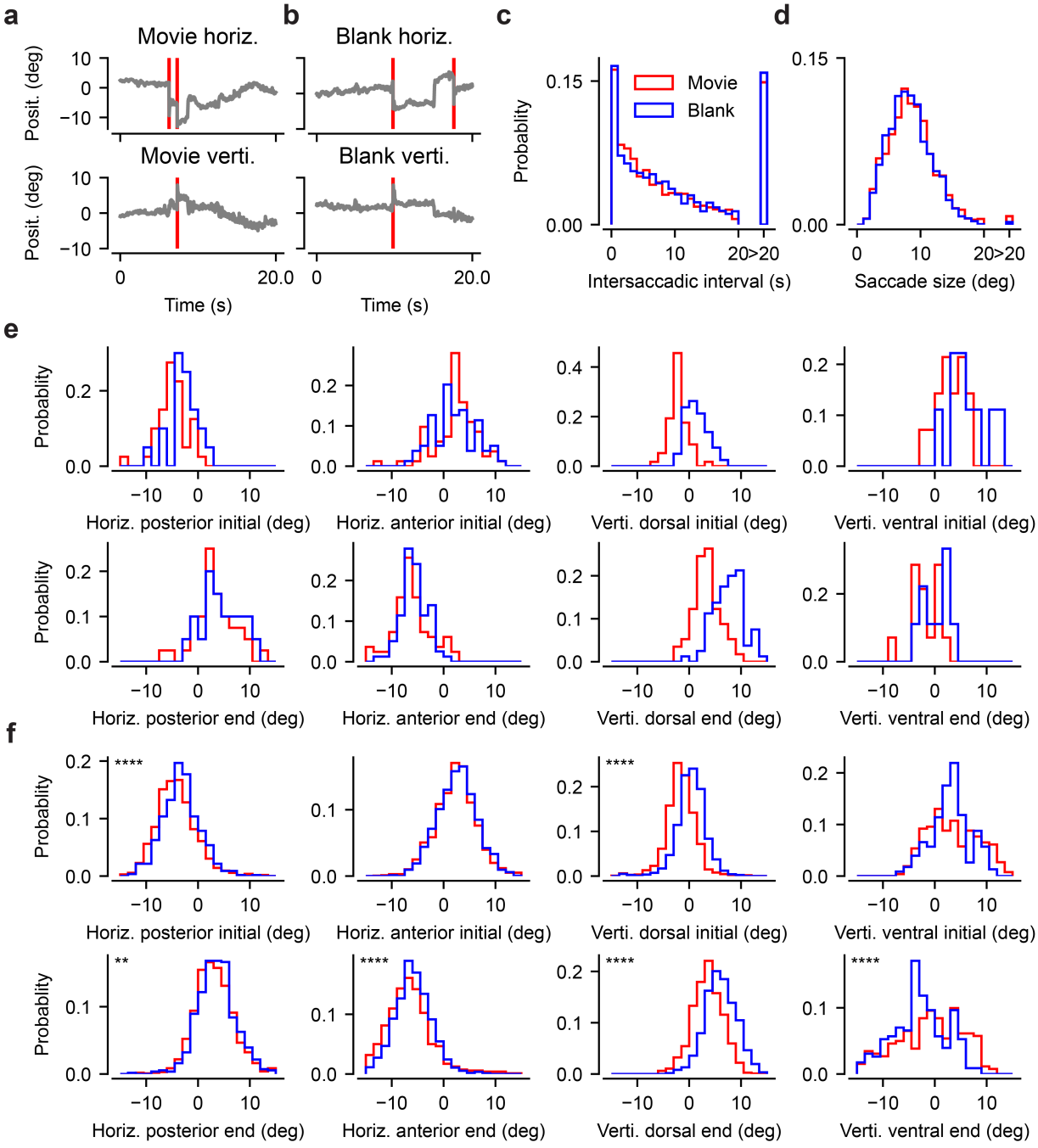

Figure 7 Saccades might contribute to the observed shift of eye position to more frontal and ventral positions during movie viewing. (**a**) Example eye position traces along the horizontal and vertical axis during a movie block. *Red*: detected saccades. (**b**) Same as (a), for an example trace during a "blank" block. (**c**) Distribution of intersaccadic intervals along the horizontal axis during movie (*red*) and blank (*blue*) blocks across sessions. (**d**) Same as (c), for saccade size. (**e**) Distribution of initial (*top*) and end (*bottom*) points for horizontal posterior, horizontal anterior, vertical dorsal and vertical ventral saccades, for an exemplary session. (**f**) Same as (e), across sessions.

References

Abballe L, Asari H (2022) Natural image statistics for mouse vision. *PLOS ONE* 17:e0262763.

Applebury M, Antoch M, Baxter L, Chun L, Falk J, Farhangfar F, Kage K, Krzystolik M, Lyass L, Robbins J (2000) The murine cone photoreceptor. *Neuron* 27:513–523.

Baden T, Euler T, Berens P (2020) Understanding the retinal basis of vision across species. *Nature Reviews Neuroscience* 21:5–20.

Baden T, Schubert T, Chang L, Wei T, Zaichuk M, Wissinger B, Euler T (2013) A tale of two retinal domains: Near-Optimal sampling of achromatic contrasts in natural scenes through asymmetric photoreceptor distribution. *Neuron* 80:1206–1217.

Bell AJ, Sejnowski TJ (1997) The "independent components" of natural scenes are edge filters. *Vision Research* 37:3327–3338.

Betsch BY, Einhäuser W, Körding KP, König P (2004) The world from a cat's perspective – statistics of natural videos. *Biological Cybernetics* 90:41–50.

Bleckert A, Schwartz GW, Turner MH, Rieke F, Wong ROL (2014) Visual Space Is Represented by Nonmatching Topographies of Distinct Mouse Retinal Ganglion Cell Types. *Current Biology* 24:310–315.

Bourke P (2005) Spherical mirror: a new approach to hemispherical dome projection. *Proceedings of the 3rd international conference on Computer graphics and interactive techniques in Australasia and South East Asia* pp. 6–9.

Brainard DH (1997) The psychophysics toolbox. *Spatial Vision* 10:433 – 436.

Coppola DM, White LE, Fitzpatrick D, Purves D (1998) Unequal representation of cardinal and oblique contours in ferret visual cortex. *Proceedings of the National Academy of Sciences* 95:2621–3.

Denman DJ, Siegle JH, Koch C, Reid RC, Blanche TJ (2017) Spatial Organization of Chromatic Pathways in the Mouse Dorsal Lateral Geniculate Nucleus. *The Journal of Neuroscience* 37:1102–1116.

Dorr M, Martinetz T, Gegenfurtner KR, Barth E (2010) Variability of eye movements when viewing dynamic natural scenes. *Journal of Vision* 10:28–28.

Dräger UC, Olsen JF (1980) Origins of crossed and uncrossed retinal projections in pigmented and albino mice: MOUSE RETINAL GANGLION CELLS. *Journal of Comparative Neurology* 191:383–412.

772 Franke K, Chagas AM, Zhao Z, Zimmermann MJY, Qiu Y, Szatko K, Baden T, Euler T (2019)
773 An arbitrary-spectrum spatial visual stimulator for vision research. *bioRxiv* p. 649566.

774 Froudarakis E, Berens P, Ecker AS, Cotton RJ, Sinz FH, Yatsenko D, Saggau P, Bethge M, Tolias
775 AS (2014) Population code in mouse V1 facilitates readout of natural scenes through increased
776 sparseness. *Nature Neuroscience* 17:851.

777 Ganguli D, Simoncelli EP (2010) Implicit encoding of prior probabilities in optimal neural popu-
778 lations. *Adv Neural Inf Process Syst* 2010:658–666.

779 Geisler WS (2007) Visual Perception and the Statistical Properties of Natural Scenes. *Annual*
780 *Review of Psychology* 59:167–192.

781 Girshick AR, Landy MS, Simoncelli EP (2011) Cardinal rules: Visual orientation perception reflects
782 knowledge of environmental statistics. *Nature Neuroscience* 14:926–32.

783 Groner MT, Groner R, von Mühlenen A (2008) The effect of spatial frequency content on parameters
784 of eye movements. *Psychological Research* 72:601–608.

785 Grozdanic S, Betts DM, Allbaugh RA, Sakaguchi DS, Kwon YH, Kardon RH, Sonea IM (2003)
786 Characterization of the pupil light reflex, electroretinogram and tonometric parameters in healthy
787 mouse eyes. *Current Eye Research* 26:371–378.

788 Gupta D, M**y**narski W, Sumser A, Symonova O, Svatoň J, Joesch M (2022) Panoramic visual
789 statistics shape retina-wide organization of receptive fields preprint, Neuroscience.

790 Haverkamp S (2005) The primordial, blue-cone color system of the mouse retina. *Journal of*
791 *Neuroscience* 25:5438–5445.

792 Hofer SB, Ko H, Pichler B, Vogelstein J, Ros H, Zeng H, Lein E, Lesica NA, Mrsic-Flogel TD
793 (2011) Differential connectivity and response dynamics of excitatory and inhibitory neurons in
794 visual cortex. *Nature Neuroscience* 14:1045–52.

795 Holmgren CD, Stahr P, Wallace DJ, Voit KM, Matheson EJ, Sawinski J, Bassetto G, Kerr JN
796 (2021) Visual pursuit behavior in mice maintains the pursued prey on the retinal region with
797 least optic flow. *eLife* 10:e70838.

798 Hoy JL, Yavorska I, Wehr M, Niell CM (2016) Vision Drives Accurate Approach Behavior during
799 Prey Capture in Laboratory Mice. *Current Biology* 26:3046–3052.

800 Jacobs GH, Williams GA, Fenwick JA (2004) Influence of cone pigment coexpression on spectral
801 sensitivity and color vision in the mouse. *Vision research* 44:1615–1622.

802 Kleiner M, Brainard D, Pelli D, Ingling A, Murray R, Broussard C (2007) What's new in
803 psychtoolbox-3. *Perception* 36:1–16.

804 Kreile AK, Bonhoeffer T, Hubener M (2011) Altered visual experience induces instructive changes
805 of orientation preference in mouse visual cortex. *Journal of Neuroscience* 31:13911–13920.

806 La Chioma A, Bonhoeffer T, Hübener M (2019) Area-Specific Mapping of Binocular Disparity
807 across Mouse Visual Cortex. *Current Biology* 29:2954–2960.e5.

808 Land MF (1999) Motion and vision: Why animals move their eyes. *Journal of Comparative*
809 *Physiology A: Sensory, Neural, and Behavioral Physiology* 185:341–352.

810 Land M (2019) Eye movements in man and other animals. *Vision Research* 162:1–7.

811 Land MF (2015) Eye movements of vertebrates and their relation to eye form and function. *Journal*
812 *of Comparative Physiology A* 201:195–214.

813 Li B, Peterson MR, Freeman RD (2003) Oblique effect: A neural basis in the visual cortex. *Journal*
814 *of Neurophysiology* 90:204–217.

815 Lopes G, Farrell K, Horrocks EA, Lee CY, Morimoto MM, Muzzu T, Papanikolaou A, Rodrigues
816 FR, Wheatcroft T, Zucca S, Solomon SG, Saleem AB (2021) Creating and controlling visual
817 environments using BonVision. *eLife* 10:e65541.

818 Lucas RJ, Douglas RH, Foster RG (2001) Characterization of an ocular photopigment capable of
819 driving pupillary constriction in mice. *Nature Neuroscience* 4:621–626.

820 Mathis A, Mamidanna P, Cury KM, Abe T, Murthy VN, Mathis MW, Bethge M (2018) DeepLab-
821 Cut: Markerless pose estimation of user-defined body parts with deep learning. *Nature Neuro-*
822 *science* 21:1281–1289.

823 Meyer AF, O'Keefe J, Poort J (2020) Two distinct types of eye-head coupling in freely moving
824 mice. *Current Biology* 30:2116–2130.

825 Meyer AF, Poort J, O'Keefe J, Sahani M, Linden JF (2018) A head-mounted camera system
826 integrates detailed behavioral monitoring with multichannel electrophysiology in freely moving
827 mice. *Neuron* 100:46–60.

828 Michaiel AM, Abe ET, Niell CM (2020) Dynamics of gaze control during prey capture in freely
829 moving mice. *Elife* 9:e57458.

830 Nadal-Nicolás FM, Kunze VP, Ball JM, Peng BT, Krishnan A, Zhou G, Dong L, Li W (2020) True
831 S-cones are concentrated in the ventral mouse retina and wired for color detection in the upper
832 visual field. *eLife* 9:e56840.

833 Nasr S, Tootell RBH (2012) A cardinal orientation bias in scene-selective visual cortex. *The Journal*
834 *of Neuroscience: The Official Journal of the Society for Neuroscience* 32:14921–14926.

835 Niell CM, Stryker MP (2010) Modulation of Visual Responses by Behavioral State in Mouse Visual
836 Cortex. *Neuron* 65:472–479.

Olshausen BA, Field DJ (1996) Emergence of simple-cell receptive field properties by learning a sparse code for natural images. *Nature* 381:607–609.

Oommen BS, Stahl JS (2008) Eye orientation during static tilts and its relationship to spontaneous head pitch in the laboratory mouse. *Brain Research* 1193:57–66.

Parker PR, Abe ET, Leonard ES, Martins DM, Niell CM (2022) Joint coding of visual input and eye/head position in V1 of freely moving mice. *Neuron* p. S0896627322008042.

Pennesi ME, Lyubarsky AL, Pugh EN J (1998) Extreme responsiveness of the pupil of the dark-adapted mouse to steady retinal illumination. *Investigative Ophthalmology and Visual Science* 39:2148–2156.

Prusky GT, Alam NM, Beekman S, Douglas RM (2004) Rapid Quantification of Adult and Developing Mouse Spatial Vision Using a Virtual Optomotor System. *Investigative Ophthalmology Visual Science* 45:4611–4616.

Qiu Y, Zhao Z, Klindt D, Kautzky M, Szatko KP, Schaeffel F, Rifai K, Franke K, Busse L, Euler T (2021) Natural environment statistics in the upper and lower visual field are reflected in mouse retinal specializations. *Current Biology* .

Read JCA (2021) Binocular Vision and Stereopsis Across the Animal Kingdom. *Annual Review of Vision Science* 7:389–415.

Remtulla S, Hallett P (1985) A schematic eye for the mouse, and comparisons with the rat. *Vision research* 25:21–31.

Rhim I, Coello-Reyes G, Ko Hk, Nauhaus I (2017) Maps of cone opsin input to mouse V1 and higher visual areas. *Journal of Neurophysiology* p. jn.00849.2016.

Röhlich P, van Veen T, Szél Á (1994) Two different visual pigments in one retinal cone cell. *Neuron* 13:1159–1166.

Sakatani T, Isa T (2004) Pc-based high-speed video-oculography for measuring rapid eye movements in mice. *Neuroscience research* 49:123–131.

Sakatani T, Isa T (2007) Quantitative analysis of spontaneous saccade-like rapid eye movements in C57BL/6 mice. *Neuroscience Research* 58:324–31.

Samonds JM, Choi V, Priebe NJ (2019) Mice Discriminate Stereoscopic Surfaces Without Fixating in Depth. *Journal of Neuroscience* 39:8024–8037.

Samonds JM, Geisler WS, Priebe NJ (2018) Natural image and receptive field statistics predict saccade sizes. *Nature Neuroscience* 21:1591.

Sattler NJ, Wehr M (2021) A head-mounted multi-camera system for electrophysiology and behavior in freely-moving mice. *Frontiers in neuroscience* 14:1418.

Schmucker C, Schaeffel F (2004) A paraxial schematic eye model for the growing c57bl/6 mouse. *Vision research* 44:1857–1867.

Scholl B, Burge J, Priebe NJ (2013) Binocular integration and disparity selectivity in mouse primary visual cortex. *Journal of Neurophysiology* 109:3013–3024.

Seabrook TA, Burbridge TJ, Crair MC, Huberman AD (2017) Architecture, Function, and Assembly of the Mouse Visual System. *Annual Review of Neuroscience* 40:499–538.

Sedigh-Sarvestani M, Fitzpatrick D (2022) What and Where: Location-Dependent Feature Sensitivity as a Canonical Organizing Principle of the Visual System. *Frontiers in Neural Circuits* 16:834876.

Shapcott KA, Weigand M, Glukhova I, Havenith MN, Schölvinck ML (2022) DomeVR: A setup for experimental control of an immersive dome virtual environment created with Unreal Engine 4 preprint, Neuroscience.

Shen G, Tao X, Zhang B, Smith EL, Chino YM (2014) Oblique effect in visual area 2 of macaque monkeys. *Journal of Vision* 14:3–3.

Sibille J, Gehr C, Benichov JI, Balasubramanian H, Teh KL, Lupashina T, Vallentin D, Kremkow J (2022) High-density electrode recordings reveal strong and specific connections between retinal ganglion cells and midbrain neurons. *Nature Communications* 13:5218.

Sit KK, Goard MJ (2020) Distributed and retinotopically asymmetric processing of coherent motion in mouse visual cortex. *Nature Communications* 11:3565.

Speed A, Del Rosario J, Burgess CP, Haider B (2019) Cortical State Fluctuations across Layers of V1 during Visual Spatial Perception. *Cell Reports* 26:2868–2874.e3.

Stabio ME, Sondereker KB, Haghgou SD, Day BL, Chidsey B, Sabbah S, Renna JM (2018) A novel map of the mouse eye for orienting retinal topography in anatomical space. *Journal of Comparative Neurology* 526:1749–1759.

Stahl JS (2004) Using eye movements to assess brain function in mice. *Vision Research* 44:3401–3410.

Switkes E, Mayer MJ, Sloan JA (1978) Spatial frequency analysis of the visual environment: Anisotropy and the carpentered environment hypothesis. *Vision Research* 18:1393–1399.

Szél A, Röhlich P, Caffé AR, Juliusson B, Aguirre G, Van Veen T (1992) Unique topographic separation of two spectral classes of cones in the mouse retina. *The Journal of Comparative Neurology* 325:327–342.

Tabata H, Shimizu N, Wada Y, Miura K, Kawano K (2011) Initiation of the optokinetic response (OKR) in mice. *Journal of Vision* 10:13–13.

Tan Z, Sun W, Chen TW, Kim D, Ji N (2015) Neuronal Representation of Ultraviolet Visual Stimuli in Mouse Primary Visual Cortex. *Scientific Reports* 5:12597.

van der Schaaf A, van Hateren J (1996) Modelling the Power Spectra of Natural Images: Statistics and Information. *Vision Research* 36:2759–2770.

Wallace DJ, Greenberg DS, Sawinski J, Rulla S, Notaro G, Kerr JND (2013) Rats maintain an overhead binocular field at the expense of constant fusion. *Nature* 498:65–69.

Warrant E, Johnsen S, Nilsson DE (2020) Light and visual environments .

Warwick RA, Kaushansky N, Sarid N, Golan A, Rivlin-Etzion M (2018) Inhomogeneous Encoding of the Visual Field in the Mouse Retina. *Current Biology* 28:655–665.e3.

Wisard J, Chrenek MA, Wright C, Dalal N, Pardue MT, Boatright JH, Nickerson JM (2010) Non-contact measurement of linear external dimensions of the mouse eye. *Journal of neuroscience methods* 187:156–166.

Yacoub E, Harel N, Uğurbil K (2008) High-field fMRI unveils orientation columns in humans. *Proc Natl Acad Sci USA* 105:10607–10612.

Yao G, Zhang K, Bellassai M, Chang B, Lei B (2006) Ultraviolet Light–Induced and Green Light–Induced Transient Pupillary Light Reflex in Mice. *Current Eye Research* 31:925–933.

Yarbus AL (1967) *Eye Movements and Vision*. Springer US.

Yu HH, Rosa MGP (2010) A simple method for creating wide-field visual stimulus for electrophysiology: Mapping and analyzing receptive fields using a hemispheric display. *Journal of Vision* 10:15–15.

Zahler SH, Taylor DE, Wong JY, Adams JM, Feinberg EH (2021) Superior colliculus drives stimulus-evoked directionally biased saccades and attempted head movements in head-fixed mice. *Elife* 10:e73081.

5

DISCUSSION

As Simoncelli and Olshausen (2001) stated, system neuroscience aims to understand the function of individual neurons, as well as neural systems. A neural system's evolution, and on a different timeline, its development are driven by three main factors: behavioral demands for survival and procreation, constraints on the brain, such as metabolic limits, and lastly the environmental niche a species inhabits.
In this thesis, I first focused on the third point that Simoncelli and Olshausen (2001) made, by recording and statistically analyzing naturalistic movies of mouse habitats (Qiu et al., 2021). The open-source camera system we developed is capable of recording green and UV light in the bands a mouse can sense. Subsequently, we analyzed the statistical properties of this footage and found a chromatic separation between the field above and below the horizon. Moreover, there was more chromatic contrast in the upper visual field, which spans the sky region above the horizon (Qiu et al., 2021). Training a convolutional autoencoder model with crops from the naturalistic footage prompted color opponent filters to emerge, however only when crops above the horizon were used. As the retina is more UV- and contrast-sensitive in the ventral part, and mice can discriminate color almost exclusively in the upper visual field (Denman et al., 2018), this part of my thesis supports the idea that natural scene statistics formed the early visual system.
In the second part of this thesis, I zoomed in on the behavioral needs and strategies of mice, to optimize survival in their visual world. First, I reported about eye movement patterns, described by Meyer et al. (2020). Their study shows that mice move their eyes in two different modes, closely coupled to head motion, when freely moving (Meyer et al., 2020; discussed in Manuscript 2 - Kautzky and Busse, 2020). In the first mode, the visual scene is kept stable with respect to the horizontal plane or the horizon, by counteracting head motion relative to the horizontal plane. With a second mode of head-eye motion, mice shift their gaze in the visual scene. It is

initiated by head yaw rotation, turning of the head in the horizontal plane, and the eyes follow with a fast, conjugate movement, before again stabilizing the gaze in the visual scene. This results in a 'saccade and fixate' gaze shift pattern, which can be found in a large fractions of vertebrate species (Land, 2015).
As a last part, we aimed to connect two facets of the mouse visual system, eye movements and naturalistic scenes, by constructing a setup capable of presenting naturalistic stimuli in the ecologically correct colors and over the extent of the FOV of a mouse (Kautzky et al., 2022). By showing the movies, recorded in our previous work (Qiu et al., 2021) to the FOV of one eye we discovered a shift of mean pupil position of the eye viewing the naturalistic scene. In later paragraphs I will speculate what prompted this shift.

5.1 RECORDING NATURALISTIC STIMULI

The most natural stimulus for a mouse would be its natural habitat, but mice are small and often active in the night, which imposes serious technical constraints onto observation, let alone any sort of brain activity measurement (Lipp & Wolfer, 2013). So far, many fundamental insights into mouse brain circuits and their function have been achieved by delivering reduced and often highly artificial sensory stimuli to isolate a specific computation or behavioral output, which can be repeated plenty of times to yield good statistical power (Dennis et al., 2021). Other advantages of a tightly controlled experiment in the lab are independent manipulation of all variables involved, standardized settings, and measurements that are not necessarily dependent on subject conditions (Blanchard & Blanchard, 2003). Nevertheless, some studies investigated different behaviors and the underlying brain structures of the mouse in natural environments (Jensen et al., 2003; Lipp & Wolfer, 2013). These studies were driven by the assumption that understanding how behavior emerges from ecologically relevant cues of the environment would help to comprehend the neural circuits, which evolved to ensure survival in those same environments (Dennis et al., 2021). Therefor, there has been a shift towards putting behaviors into context of natural circumstances (Gomez-Marin & Ghazanfar, 2019; Krakauer et al., 2017; McCullough & Goodhill, 2021; Parker et al., 2020).
To better understand what 'natural' means for the mouse's visual system

and to be able to deliver more naturalistic stimuli without loosing experimental control, we developed and built a camera to capture natural visual surroundings of the mouse (Qiu et al., 2021). In the camera design, we attempted to mimic different aspects of the mouse's visual system: First, we matched the FOV of one mouse eye (Seabrook et al., 2017) with a 180° fish eye lens. Second, we recorded color channels that correspond to the sensitivity ranges of mouse cones (Baden et al., 2013), by chromatically filtering the incoming light with a UV band-pass and a green band-pass spectral filter before it reaches the sensors. Our camera was mounted on a gimbal and we tried to keep the horizon in the center of the scene. With this camera positioning, we aimed to mimic compensatory eye movements, that stabilize the visual scenery on the retina and probably roughly keep the upper and lower visual field on the dorsal and ventral retina, respectively (Meyer et al., 2020; Qiu et al., 2021).

Since our goal was to produce an open source dataset of natural scenes, we created a public repository for the movies (link to repository: https://doi.org/10.5281/zenodo.4812404). Further, the hardware should be reproducible and low cost, which is why we used Raspberry Pi image sensors (Raspberry Pi Foundation, UK). Raspberry Pi single-board computers are available in many different countries, not expensive and easy to use, also thanks to a large online community. We hope that this system proves useful to the neuroscience community, and, as a group effort, we can increase the knowledge about visual environments for mice and also add to the dataset of naturalistic stimuli.

However, there are also some limitations to the camera system and consequently to the 'naturalness' of the resulting stimuli. First, as most off-the-shelf cameras, the Raspberry Pi camera sensor is equipped with a filter to capture light best matched to human cone sensitivity (Bull, 2014). Therefor, the sensor designated for UV recordings was treated as described by Wilkes et al. (2016) to improve the sensor's UV sensitivity. But even after this treatment, the sensitivity was not ideal to record during all times of the day. On one hand, during day time on sunny days, some pixels in the sky region were over-saturated. To avoid that, a larger dynamic range might be beneficial, given the different intensity distributions of both color channels over the visual field. On the other hand, recording during twilight was only possible after adjusting exposure time and ISO of both camera sensors. However, mice are often active during twilight or night times (Ripperger et al., 2011), and therefor it would be intriguing to also analyze recordings with higher frame rates from that time of day. As another consequence of

the light sensitivity difficulties, we recorded movies with a low frame rate of 25 Hz, even though, in theory, Raspberry Pi image sensors would be capable to record movies with a frame rate of 90 Hz. The low frame rate allowed for enough time to collect light on the sensor. This made it difficult to capture fast temporal dynamics of natural environments. Additionally, low frame rate introduces image blurring during movement of the camera above a certain speed threshold, consequently quick shifts of perspective were avoided in the recordings. But fast movements in the horizontal plane would be beneficial to include in the footage, as mice turn their head and thereby change their gaze direction rapidly (more than 100°/s, Meyer et al., 2020).
In summary, our camera delivers footage, despite having clear limitations, that presents a next step towards natural stimulation.

5.2 PRESENTING NATURALISTIC STIMULI

To use the naturalistic movies from our hand-held camera system (Qiu et al., 2021) as stimuli in the lab, we developed a hemispheric dome setup. Our dome spans 160° in latitude and 250° in longitude, which largely covers the mouse's visual field (Seabrook et al., 2017). A setup like this has been implemented by an increasing number of labs in the last years (Denman et al., 2017; Muzzu & Saleem, 2022; Sibille et al., 2022). The projection onto this spherical surface can be achieved via a spherical mirror, which introduces spatial distortions in the resulting image. Many labs use a commercial software to achieve an un-distorted projection ('meshmapper', Paul Bourke, http://paulbourke.net/dome/meshmapper; Denman et al., 2017; Shapcott et al., 2022; Sibille et al., 2022), which relies on visual judgment of the experimenter positioned in front of the dome. To avoid depending on subjective perception and judgments, we developed a method, which involves a laser pointer indicating the expected visual angle from the perspective of the mouse and dots projected as a radial grid, which can be moved by the experimenter to the indicated position (Kautzky et al., 2022). Like the camera design and the mouse cam movies, we will make this method and instructions for necessary hardware freely available.
One challenge we were facing, was to achieve strong UV and green stimulation on the whole dome surface (dome used in Kautzky et al. (2022):

approximately 4 m²). There are several points in the light path, were light could be lost. First, light was lost within the optical path of the projector, which receives input from a high intensity LED light source (Franke et al., 2019; Kautzky et al., 2022). Next, the reflection properties of the spherical mirror and the dome surface were not perfectly adjusted to green and especially UV light, and probably contributed to decreased luminance. Also luminance was not equal across the dome surface, due to imperfections of the mirror and the light path. Due to these uncertainties in the light path, we employed an indirect approach to confirm sufficient brightness. We took advantage of the the pupillary light reflex in mice (Pennesi et al., 1998) as response to steps of light intensities. We confirmed a clear negative relationship between light power and pupil size, which indicates good visibility for mice of both color channels. However, the dynamic range of pupil sizes was wider for the green channel and also the minimal pupil size was smaller for green light stimulation. The relative contribution of UV light to the spectrum of sunlight (Hut et al., 2000) is smaller compared to longer wavelengths, which we also found in image crops from our movies (Qiu et al., 2021). Thus we can mimic what is found in natural scenes. Additionally, it would be beneficial to be able to match intensities in the color channels in case we want to present artificial stimuli or manipulate the color distributions, therefor we have to find a way to improve UV projection.
UV light is not visible for humans and many experiments with mice are still conducted with display technology adapted to our vision (Froudarakis et al., 2014, e.g.), which makes it difficult to find suitable technology optimized for UV presentation. Denman et al. (2017) improved their setup by coating the projection surface with UV-reflective paint and used a silver-coated aluminum mirror with evenly distributed reflection properties starting from 200 nm. With these modification a luminance of 3 cd/m² was achieved, which corresponds to mesopic light levels (Billmeyer Jr., 1983). In contrast, a LCD display can achieve a mean luminance of 120 cd/m² (Sibille et al., 2022). We think, that with our high power light source, we should be able to accurately present recordings of all times of the day. Additionally it would still be beneficial to apply the enhancements described by Denman et al. (2017) to equalize green and UV reflection properties.
In summary, our setup is suitable to present naturalistic movies in spectrally relevant colors and wide field of view to head fixed mice, to further explore the function of the mouse visual system.

5.3 SCENE STATISTICS POSSIBLY SHAPED SPECIALIZATIONS OF THE MOUSE RETINA

Towards understanding natural vision in mice, we analyzed scene statistics of the naturalistic movies acquired by our hand-held camera. We focused on spatial statistics, as the motion dynamics were human made, introduced by the person holding the camera (see 2).
We analyzed contrast distributions as a function of elevation of the scene and could show, overall natural scenes are biased to dark contrast, which aligns very well with previous studies (Cooper & Norcia, 2015; Ratliff et al., 2010). This dark contrast bias is reflected in the mouse's visual system by an over-representation of Off information, e.g. in a stronger response of ventral RGCs to dark contrast stimuli (Kremkow et al., 2016; Mazade et al., 2019; Qiu et al., 2021). More specifically, the contrast distribution of the UV channel in the upper visual field is tilted towards dark contrast. Considering chromatic contrast in our images, we found that it was higher in the upper visual field. In accordance with this, the convolutional autoencoder we trained on natural image crops of our movies produced color-opponent filters for upper visual field crops, but not for lower field scenes. Moreover, color-opponent RGCs are known to be more prominent in the ventral retina (Szatko et al., 2020) and mice can discriminate color in the upper part of their field of view (Denman et al., 2018).
A recent study on high quality naturalistic 'mouse view' images, discovered similar contrast distributions (Abballe & Asari, 2022). Spatial autocorrelation of pixel intensities in the natural images was highest in the UV channel in the upper visual field, while the green channel intensities were more correlated in the lower visual field. Overall, the spatial autocorrelation was narrow in the lower visual field images and the power spectra for the lower visual field were larger than those for the upper visual field. Both of these findings suggest more fine-grained textures in the ground area of the mouse's habitat. Abballe and Asari (2022) posed an interesting question about the optimality of the functional organization of mouse retina with regards to the efficient coding (EC) theory. This theory postulates that to operate as energy efficient as possible, sensory systems evolved to adapt their neuronal representations and thus exploit redundancies in the statistics of the respective input stimulus (Barlow & Rosenblith, 1961). One prime example for this theory is the distribution of orientation preferring visual neurons, which reflects the over-represented cardinal orientations in

natural scenes (Girshick et al., 2011). But, for the mouse retina, would it not be more energy efficient and simultaneously most informative, if more sensitive S-cones sampled the lower visual field, and high contrast in the upper field could be retrieved by less-sensitive M-cones? Additionally, the higher the spatial autocorrelation or the lower the power spectrum, less fine structures are present, consequently less cones would be needed to encode information. To achieve an optimal sampling of this environment from an information-theoretic point of view, the mouse retina's cone distribution should be reversed.

Simoncelli and Olshausen (2001) pointed out a serious weakness of the pure EC approach: Not taking into account the 'task' of an animal. Not every statistical detail of an environment might be crucial for the animal's survival, and therefor the sensory system might assign different priorities. For example, reliably detecting threats from the sky surely is a selective pressure for mice, accordingly the distribution of contrast might have driven evolution of the generally more contrast- and UV-sensitive ventral retina of the mouse eye (Baden et al., 2013).

The EC theory is usually combined with constraints in the sensory system, like space restrictions, sparse activation or transmission capacity (Simoncelli & Olshausen, 2001). Many EC models have been employed with constraints to understand natural scene processing in the visual system and filters have emerged, resembling properties of RFs along the visual pathway (Bell & Sejnowski, 1997; Graham et al., 2006; Ocko et al., 2018; Qiu et al., 2022; Qiu et al., 2021).

One important factor in the image analysis of Abballe and Asari (2022) is that all images were taken during daylight. Mice are usually crepuscular or nocturnal (Turner, 2014), i.e. active during twilight periods and night. During twilight, the relative contribution of short wavelength light increases in the visual scene (Hut et al., 2000), and during dim light conditions, UV light might still be detected by rod photoreceptors, which have a second sensitivity peak around 350 nm (Govardovskii et al., 2000). Therefor, it would be intriguing to acquire high quality footage under low-light conditions, either images or, even more so, movies with our camera system, to capture more dynamic representations. Possibly, these scenes might reveal more about the function of the different specializations apparent in the mouse retina.

One could also tackle the question, why chromatic circuitry in the mouse's retina is located mainly in the ventral part, limiting mice to using color vision in the upper field. This constraint is rather unexpected, if one considers

the finding of Abballe and Asari (2022) that the spatial autocorrelation was lower in the visual field below the horizon in UV images, meaning that more fine structures should be detectable in the lower area. Additionally, chromatic and absolute contrast can be found in the lower visual field as well. Interestingly, some features of the environment, which are possibly located in the lower areas, have a distinct appearance under UV light. For example urine marks, used for social communication between mice, like marking territories, reflect UV in a specific pattern (Chávez et al., 2003; Joesch & Meister, 2016). Also fruit and some seeds stand out in the UV channel, which could support successful foraging for mice (Altshuler, 2001; Joesch & Meister, 2016).
Overall, the functional specializations of the retina reflect the abundance of chromatic contrast in the visual scene, typical for mouse habitats, and are likely to be tuned to behaviorally relevant visual information for mice.

5.4 Eye movements facilitate retinal processing of natural environments

Eye movements within vertebrates serve mainly two purposes: to shift the gaze within the visual field and to stabilize the image on the retina, to avoid motion blur (Land, 2015). Investigating eye movements under unrestricted conditions in mice, Meyer et al. (2018) mounted a light-weight eye tracking camera on the head of a mouse. Eye motion in mice predominately keeps the visual field stable with respect to the ground (Kautzky & Busse, 2020; Meyer et al., 2020), compensating for head movements, more precisely head tilt. Therefor, it is likely that the temporo-nasal retinal axis is approximately aligned with the horizon of the visual scene, ensuring that the upper, UV-dominated field is sensed by the ventral retina, and the more green, lower visual field would fall on the dorsal, more green-sensitive retina (Meyer et al., 2020; Qiu et al., 2021).
This mechanism would make sure that visual perception of natural scenes happened as efficiently as biologically possible. The evolution or development of the gaze stabilization behavior might be explained by a generalization of the original EC theory posed by Barlow and Rosenblith (1961). The so-called 'active EC hypothesis' acknowledges that the statistics of the visual environment are also a function of behavior (Lonini et al., 2013). Both

sensory processing and behavior optimize perceptual representations under sparsity constraints (Eckmann et al., 2020; Klimmasch et al., 2018; Teulière et al., 2015; Zhao et al., 2012). Zhu et al. (2022) proposed an active EC model explaining development of torsional eye movements in human subjects, which learns sensory representation and behavior without external interference, just by applying active EC principles. Another fully self-calibrating model delivered an explanatory approach for the development of the optokinetic response (OKR) in humans, including both sensory processing and motor action (Zhang et al., 2016). Since the compensatory eye movements of mice are tightly coupled to vestibular reflexes, such as the OKR and VOR, it would be interesting to further explore mice' early visual processing with models applying the active EC theory.

5.5 Eye movements in the context of natural scene statistics

The second type of eye movements, also linked to head movements, which Meyer et al. (2020) described in freely moving mice, shifts their gaze through the environment. The connected head movements are unanimously yaw rotations, i.e. reorienting in the horizontal plane. Generally, the head movements initiate the gaze shifts, whereas the conjugate fast eye motion follows. Between those shifts, mice keep the gaze fixed with the help of compensatory eye movements, which results in the so called 'saccade and fixate' pattern (Land, 2015). This pattern persists during different behavioral demands on the animal, e.g. freely exploring, a simple visually guided tracking task (Meyer et al., 2020) or during prey capture (Michaiel et al., 2020).
Michaiel et al. (2020) examined eye movements in freely moving mice in the context of a natural behavior, but concerning the visual scene, the cricket was the only natural feature in their lab arena. Also other studies with unrestricted mice, did not provide a naturalistic visual setting, but rather a lab environment (Holmgren et al., 2021; Meyer et al., 2018; Sattler & Wehr, 2021). As discussed earlier (see section 5.1), control of experimental parameters is important and implementing a setup for freely roaming mice and naturalistic visual stimulation is difficult.
Thus, we decided to take a step back into more controlled settings and record eye motion of head fixed mice as response to naturalistic movies in

our dome setup (Kautzky et al., 2022). We did not find repeated eye movement pattern over repeated movie snippets, which supports the idea that mice do not move their eyes to target specific features in their environment. This also matches our finding that saccadic eye movements during gray screen presentation occur at a similar frequency and size as during naturalistic movies. Interestingly, variability of pupil position was less while mice viewed movies, than when there was no movie stimulus. Maybe changes in variability can be explained by the mouse trying to decorrelate input on the retina, to provide individual neurons, which might have receptive fields with different properties, new information (Samonds et al., 2018). According to this interpretation, the range of pupil position distribution was larger during gray screen compared to movies, since there was almost no variability of the visual information during gray screen stimulation, whereas during movies novel visual content can be received by only changing pupil position slightly. Samonds et al. (2018) further showed, that saccade-size distributions could be predicted by distances in natural scenes that are necessary to provide RFs in V1 with novel information. Therefor, if presenting a smaller image, which holds more information in a specific region, than the same image in original size, saccade sizes were smaller. It would be intriguing to see if this effect will hold true for dynamic scenes, like our movies, where new visual information can be experienced not only by moving the eyes, but also passively by optic flow. To validate this theory, we could show movies in different sizes on the dome and compare saccade size distributions.
Not only the distribution of positions was less variable, the mean pupil position during passive viewing of naturalistic movies was also systematically more nasal ($0.9 \pm 1.2°$) and ventral ($1.9 \pm 1.6°$) compared to gray screen viewing. As described before, the horizon of the scene is probably centered onto the retina, and the horizon of the stimulus movie is at the largest extent of the dome, as is the head of the mouse. But the mouse eye axes point up around 30° (Sakatani & Isa, 2007), hence the horizon might be too low. Our setup is well suited to test this theory, by just simply shifting the naturalistic movie along the vertical axis on the dome, which would change the horizon's position relative to the mouse. To further test if the particular chromatic distributions in the naturalistic scenes trigger the mouse to center the gaze on the horizon, one could stimulate with iso-luminant movies and observe the mouse's reaction.
To adjust the line of sight to the horizon, movement on the vertical axis would be enough, but the mean pupil position is also shifted towards the nose. Speculating about the overall shift of gaze in our data is difficult, since

we only monitored the right eye of the mouse. Thus, we do not know, if the mouse moved the left eye non-conjugately, which would mean, moving it also anterior and ventral, or in a conjugate manner, i.e. both eyes move in the same direction. Since these different movements would yield different gaze directions and therefor probably serve different purposes in the behavioral output of the mouse, we will from now on monitor both eyes. Still, I will try to discuss possible implications of the shift of eye position in the next paragraphs, starting with the assumption that the left eye moved non-conjugately.

By moving both eyes front and down, the maximal extent of the binocular field of the mouse would move more frontal and down (Dräger & Olsen, 1980; Meyer et al., 2018; Wallace et al., 2013). In front of the mouse the binocular field is only around 40° wide (Samonds et al., 2019; Seabrook et al., 2017), nevertheless, this small area of the visual world seems to have high relevance in visual processing and the information from both eyes is integrated in the early visual system (Scholl et al., 2013). Specific neurons in mouse visual cortex are tuned to binocular disparities (La Chioma et al., 2019). Contrasting right and left eye information could be used to derive depth information about the visual scene, i.e. stereoscopic vision (Samonds et al., 2019). Also the '*focea*', a retinotopically matched region of the visual cortex, which provides higher spatial resolution, is located in the binocular zone of the visual field (van Beest et al., 2021). What might be the purpose of enhancing vision within the '*focea*'? One specific goal of retinal specialization seems to be detecting airborne predators (Qiu et al., 2021), however, moving the binocular field more ventral would not support this purpose. On the other hand, mice heavily rely on binocular vision for hunting small insects and keep their prey as centered as possible in the binocular zone ahead of them (Hoy et al., 2016; Johnson et al., 2021). Interestingly, the center of the zone, where the cricket is stabilized in, is also the area of least optic flow, which coincides with the heading direction during locomotion, and provides a representation of the prey with smallest possible motion-induced disturbance (Holmgren et al., 2021; Sabbah et al., 2017; van Beest et al., 2021). Neurons in V1 and higher visual areas representing the lower visual space, where prey would be found, are more responsive to coherent motion then for the upper visual field (Sit & Goard, 2020). But mice in our setup were viewing movies passively and never encountered a cricket, implicating the shift of pupil position likely has nothing to do with hunting behavior.

One could easily test the importance of optic flow for the change of mean pupil position, assuming non-conjugate eye movements, by, e.g. rotating the

movies 90°, to introduce motion on the vertical axis, or 180°, to simulate rather unnatural backwards movement and monitor the eye movements.
Binocular optic flow information is processed in higher visual areas, rostrolateral (RL) and anterior (A) visual cortex, where also tactile sensory input from the whiskers is integrated (Olcese et al., 2013). Both sensory modalities are highly valuable for mice during spatial navigation, and the posterior parietal cortex, to which both areas RL and area A presumably belong to, is known for decision making during spatial navigation (Gold & Shadlen, 2007). Therefor, it would be very intriguing to let mice actively navigate through a virtual reality rendered from naturalistic movies. If the change in pupil position is evoked by visual flow, we would also find the shift in a more active setting.
Another reason for a closed loop experiment, coupling running speed of the animal to the motion speed of the naturalistic scene, is that passive viewing can introduce visuomotor mismatches (Fiser et al., 2016; Keller et al., 2012). These mismatches are encoded by V1 neurons and might serve to detect objects moving relative to the self-motion induced visual flow. These objects might carry ecological relevance for the mouse, e.g. the animal has to flee or can pursue the object.
A conjugate eye movement would shift the line of sight lower and slightly left of the movie stimulus, which was centered on the eye axis of the right eye. The purpose of this change in gaze direction, could be generated due to the fact, that the center of optical flow in the movies, which should represent the heading direction of the animal (Holmgren et al., 2021; Sabbah et al., 2017), was possibly not positioned exactly in front of the animal. Consequently, shifting the stimulus along the horizontal axis might yield such a shift in pupil position.
In conclusion, at this point in time, we can not say with certainty what triggered the shift of pupil position in one eye. But I am confident, that we can claim that our dome setup, combined with naturalistic movies, provides great potential to investigate eye movements in mice, that enable them to optimally navigate their environment and enhance chances of survival.

5.6 OUTLOOK

The best way to capture the spatial-temporal dynamics of an animal's head movements in a video, is to record it with a camera, mounted on the animal's head, as several groups did with various animal species (cats: Betsch et al., 2004, birds: Rutz and Troscianko, 2013, mice: Froudarakis et al., 2014). In general, due to the low body weight of mice, a light-weight head mounted camera system is quite challenging to engineer, but has been done in several ways (Froudarakis et al., 2014; Meyer et al., 2018; Michaiel et al., 2020; Sattler & Wehr, 2021).

So far, employing a head mounted camera, which records movies that are chromatically matched to the needs of mice, has not been done. Our future goal would be to design a camera that can record UV and green light, with a FOV of around 180° and can be mounted on the mouse's head. Of course, the resulting video would be very unsteady caused by the mouse's body motion, e.g. during running. To post-hoc stabilize the scene movies, we plan on utilizing the accompanying compensatory eye movements. Therefor, another camera, on top of the mouse's head should acquire eye motion of at least one eye. To extract gaze direction in space, one would need one more addition to the head-mounted system: A gyroscope to measure head position relative to the ground.

We developed an approximation of this ideal system, similar to Sattler and Wehr (2021), by combining a light-weight, analogue RGB camera with one eye-tracking camera and a gyroscope (Figure 5.1 a, left: Camera system from above, right: Camera system from below).

The gyroscope is built from a 9-axis IMU on a custom made circuit board and delivers orientation data, relative to the sensor (for details see https://www.bosch-sensortec.com/products/smart-sensors/bno055/#description). The eye tracking camera is designed as described in Meyer et al. (2018), recording eye movements via an IR mirror which does not constrict the animal's FOV. A 160 ° fish eye lens is used for the scene camera, since small, light weight, but still high quality lenses are hard to find off-the-shelf, we settled on a smaller FOV lens for higher quality. Both, the scene and the eye tracking camera are analogue cameras, with the maximal frame rate of 30 Hz, which is rather slow for head movements of mice can reach more than 100 °/s and saccadic eye movements more than 600 °/s (Kautzky et al., 2022; Meyer et al., 2020; Sakatani & Isa, 2007). Nevertheless, at the moment the advantages of these cameras prevail. For example, the small weight of one

camera (around 0.15 g) is extremely valuable for our purpose, but also that all cables can be easily re-soldered and therefor adjusted to one's demands is very useful. The flexibility of the cables and the position on top to the mouse strongly influences natural movements of the mouse. At the moment, the experimenter has to hold the cables central over the mouse in the platform, which restricts the recording time significantly and occasionally hinders comfortable motion of the animal. Due to another advantage of these cameras, which, compared to digital camera sensors, have relatively low transmission rates, the video information could be transmitted via an electrical rotary joint. This would keep the cables stable centered above the platform, increasing recording time, and rotate with the animal, facilitating unrestricted movement of the mouse. Thus, we plan to install a commutator, equipped with a sensor, e.g. a hall sensor, and a motor to support rotations the mouse makes (Liberti et al., 2017).

To estimate gaze direction in space, one has to know exact spatial properties of the environment. This can be done by creating a 3D mesh model from a digital laser scan of the whole room, which was done by a external company for the study of Holmgren et al. (2021). Because a highly specialized company like this is presumably not easy to find, and, after the scan, nothing can be changed, we sought an easier, maybe more preliminary solution. Since our dome setup is spatially calibrated to present movies in visual angle coordinates from the position of a head fixed mouse in the center, we can connect pupil position with the help of an anatomical model of the eye in the head to the dome surface.

We now install a small arena, from UV-permeable material, in the center of the dome and track the animals position with an IR camera from below (5.1 b, c). After a short calibration phase, where the animal is head-fixed in the center of the arena, we can extract mouse body, head and pupil position relative to the center of the dome and therefor obtain the intersection between gaze direction and dome surface.

Our future objective with this setup is to present naturalistic images on the dome, while monitoring all the behavioral parameters described above, and we believe that this can further our understanding of eye movements in freely behaving mice.

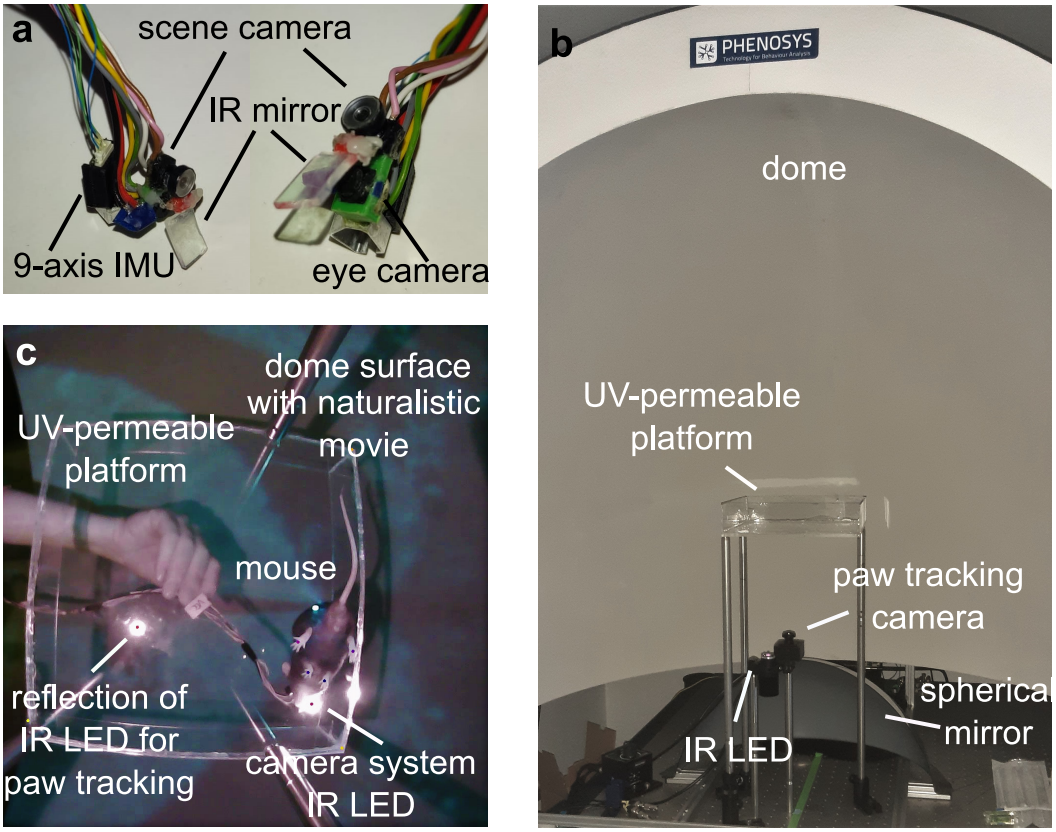

Figure 5.1: Setup for freely moving eye tracking. (a) Head mounted camera system from two perspectives. The analogue scene camera with a 160° lens is mounted on top of the analogue eye tracking camera, designed as described in Meyer et al. (2018), and the 9-axis IMU in a 3D printed holder is glued to the aluminum camera holder. **(b)** Dome setup with freely moving modifications. Instead of a treadmill, a UV-permeable Plexiglas platform is in the center of the dome, with the paw tracking IR sensitive camera and an IR LED below. **(c)** Exemplary frame of paw tracking camera.

Abballe, L. & Asari, H. (2022). Natural image statistics for mouse vision. *PLOS One*, *17*(1). https://doi.org/10.1371/journal.pone.0262763

Almada, R., Genewsky, A., Heinz, D., Kaplick, P., Coimbra, N. & Wotjak, C. (2018). Stimulation of the nigrotectal pathway at the level of the superior colliculus reduces threat recognition and causes a shift from avoidance to approach behavior. *Frontiers in Neural Circuits*, *12*. https://doi.org/10.3389/fncir.2018.00036

Altshuler, D. (2001). Ultraviolet reflectance in fruits, ambient light composition and fruit removal in a tropical forest. *Evolutionary Ecology Research*, *3*.

Baden, T. & Osorio, D. (2019). The retinal basis of vertebrate color vision. *Annual Review of Vision Science*, *5*(1). https://doi.org/10.1146/annurev-vision-091718-014926

Baden, T., Berens, P., Franke, K., Rosón, M. R., Bethge, M. & Euler, T. (2016). The functional diversity of retinal ganglion cells in the mouse. *Nature*, *529*(7586). https://doi.org/10.1038/nature16468

Baden, T., Schubert, T., Chang, L., Wei, T., Zaichuk, M., Wissinger, B. & Euler, T. (2013). A tale of two retinal domains: Near-Optimal sampling of achromatic contrasts in natural scenes through asymmetric photoreceptor distribution. *Neuron*, *80*(5). https://doi.org/10.1016/j.neuron.2013.09.030

Barlow, H. B. & Rosenblith, W. A. (1961). Possible principles underlying the transformations of sensory messages. MIT Press.

Barlow, H. B. & Hill, R. M. (1963). Selective sensitivity to direction of movement in ganglion cells of the rabbit retina. *Science*, *139*(3553). https://doi.org/10.1126/science.139.3553.412

Bauer, J., Weiler, S., Fernholz, M. H., Laubender, D., Scheuss, V., Hübener, M., Bonhoeffer, T. & Rose, T. (2021). Limited functional convergence

of eye-specific inputs in the retinogeniculate pathway of the mouse. *Neuron*, *109*(15). https://doi.org/10.1016/j.neuron.2021.05.036

Baylor, D. A., Lamb, T. D. & Yau, K. W. (1979). Responses of retinal rods to single photons. *The Journal of Physiology*, *288*(1). https://doi.org/10.1113/jphysiol.1979.sp012716

Bedell, H., Tong, J. & Aydin, M. (2010). The perception of motion smear during eye and head movements. *Vision research*, *50*(24). https://doi.org/10.1016/j.visres.2010.09.025

Bell, A. J. & Sejnowski, T. J. (1997). The "independent components" of natural scenes are edge filters. *Vision Research*, *37*(23). https://doi.org/10.1016/S0042-6989(97)00121-1

Bergmann, R., Sehara, K., Dominiak, S. E., Kremkow, J., Larkum, M. E. & Sachdev, R. N. S. (2022). Coordination between eye movement and whisking in head-fixed mice navigating a plus maze. *eNeuro*, *9*(4). https://doi.org/10.1523/ENEURO.0089-22.2022

Betsch, B. Y., Einhäuser, W., Körding, K. P. & König, P. (2004). The world from a cat's perspective – statistics of natural videos. *Biological Cybernetics*, *90*(1). https://doi.org/10.1007/s00422-003-0434-6

Bex, P. J. & Makous, W. (2002). Spatial frequency, phase, and the contrast of natural images. *Journal of the Optical Society of America*, *19*(6). https://doi.org/10.1364/JOSAA.19.001096

Billmeyer Jr., F. W. (1983). *Color science: Concepts and methods, quantitative data and formulae, 2nd ed., by gunter wyszecki and w. s. stiles, john wiley and sons, new york, 1982, 950 pp. price: $75.00* (Vol. 8). https://doi.org/10.1002/col.5080080421

Blanchard, R. & Blanchard, D. (2003). Bringing natural behaviors into the laboratory: A tribute to paul maclean. *Physiology & Behavior*, *79*(3). https://doi.org/10.1016/S0031-9384(03)00157-4

Bleckert, A., Schwartz, G., Turner, M., Rieke, F. & Wong, R. (2014). Visual space is represented by nonmatching topographies of distinct mouse retinal ganglion cell types. *Current Biology*, *24*(3). https://doi.org/10.1016/j.cub.2013.12.020

Bolaños, F., Orlandi, J., Aoki, R., Jagadeesh, A., Gardner, J. & Benucci, A. (2022). Efficient coding of natural images in the mouse visual cortex. *preprint on bioRxiv*. https://doi.org/10.1101/2022.09.14.507893

Bourke, P. (2005). Spherical mirror: A new approach to hemispherical dome projection. *Proceedings of the 3rd international conference on Computer graphics and interactive techniques in Australasia and South East Asia*. https://doi.org/10.1145/1101389.1101445

Bringmann, A., Syrbe, S., Görner, K., Kacza, J., Francke, M., Wiedemann, P. & Reichenbach, A. (2018). The primate fovea: Structure, function and development. *Progress in Retinal and Eye Research*, *66*. https://doi.org/10.1016/j.preteyeres.2018.03.006

Brunswik, E. & Kamiya, J. (1953). Ecological cue-validity of proximity and of other gestalt factors. *The American Journal of Psychology*, *66*(1). https://doi.org/10.2307/1417965

Bull, D. R. (2014). Digital picture formats and representations. *Communicating pictures*. Academic Press. https://doi.org/10.1016/B978-0-12-405906-1.00004-0

Cahill, H. & Nathans, J. (2008). The optokinetic reflex as a tool for quantitative analyses of nervous system function in mice: Application to genetic and drug-induced variation. *PLOS One*, *3*(4). https://doi.org/10.1371/journal.pone.0002055

Cao, D., Zele, A. J. & Pokorny, J. (2007). Linking impulse response functions to reaction time: Rod and cone reaction time data and a computational model. *Vision Research*, *47*(8). https://doi.org/10.1016/j.visres.2006.11.027

Carandini, M., Demb, J. B., Mante, V., Tolhurst, D. J., Dan, Y., Olshausen, B. A., Gallant, J. L. & Rust, N. C. (2005). Do we know what the early visual system does? *Journal of Neuroscience*, *25*(46). https://doi.org/10.1523/JNEUROSCI.3726-05.2005

Cepko, C. L., Austin, C. P., Yang, X., Alexiades, M. & Ezzeddine, D. (1996). Cell fate determination in the vertebrate retina. *Proceedings of the National Academy of Sciences*, *93*(2). https://doi.org/10.1073/pnas.93.2.589

Chávez, A. E., Bozinovic, F., Peichl, L. & Palacios, A. G. (2003). Retinal Spectral Sensitivity, Fur Coloration, and Urine Reflectance in the Genus Octodon (Rodentia): Implications for Visual Ecology. *Investigative Ophthalmology & Visual Science*, *44*(5). https://doi.org/10.1167/iovs.02-0670

Cleland, B. G. & Levick, W. R. (1974). Properties of rarely encountered types of ganglion cells in the cat's retina and on overall classification. *The Journal of Physiology*, *240*(2). https://doi.org/10.1113/jphysiol.1974.sp010618

Coleman, J., Law, K. & Bear, M. (2009). Anatomical origins of ocular dominance in mouse primary visual cortex. *Neuroscience*, *161*(2). https://doi.org/10.1016/j.neuroscience.2009.03.045

Collewijn, H. (1977). Eye- and head movements in freely moving rabbits. *The Journal of Physiology*, *266*(2). https://doi.org/10.1113/jphysiol.1977.sp011778

Cooper, E. A. & Norcia, A. M. (2015). Predicting cortical dark/bright asymmetries from natural image statistics and early visual transforms. *PLOS Computational Biology*, *11*(5). https://doi.org/10.1371/journal.pcbi.1004268

Coppola, D. M., White, L. E., Fitzpatrick, D. & Purves, D. (1998). Unequal representation of cardinal and oblique contours in ferret visual cortex. *Proceedings of the National Academy of Sciences*, *95*(5). https://doi.org/10.1073/pnas.95.5.2621

Cruz-Martín, A., El-Danaf, R. N., Osakada, F., Sriram, B., Dhande, O. S., Nguyen, P. L., Callaway, E. M., Ghosh, A. & Huberman, A. D. (2014). A dedicated circuit links direction-selective retinal ganglion cells to the primary visual cortex. *Nature*, *507*(7492). https://doi.org/10.1038/nature12989

Curcio, C. A. & Allen, K. A. (1990). Topography of ganglion cells in human retina. *Journal of Comparative Neurology*, *300*(1). https://doi.org/10.1002/cne.903000103

Curcio, C. A., Sloan, K. R., Packer, O., Hendrickson, A. E. & Kalina, R. E. (1987). Distribution of cones in human and monkey retina: Individual variability and radial asymmetry. *Science*, *236*(4801). https://doi.org/10.1126/science.3576186

Denman, D. J., Luviano, J. A., Ollerenshaw, D. R., Cross, S., Williams, D., Buice, M. A., Olsen, S. R. & Reid, R. C. (2018). Mouse color and wavelength-specific luminance contrast sensitivity are non-uniform across visual space. *eLife*, *7*. https://doi.org/10.7554/eLife.31209

Denman, D. J., Siegle, J. H., Koch, C., Reid, R. C. & Blanche, T. J. (2017). Spatial Organization of Chromatic Pathways in the Mouse Dorsal Lateral Geniculate Nucleus. *The Journal of Neuroscience*, *37*(5). https://doi.org/10.1523/JNEUROSCI.1742-16.2016

Dennis, E. J., El Hady, A., Michaiel, A., Clemens, A., Tervo, D. R. G., Voigts, J. & Datta, S. R. (2021). Systems neuroscience of natural behaviors in rodents. *Journal of Neuroscience*, *41*(5). https://doi.org/10.1523/JNEUROSCI.1877-20.2020

Dickman, C. R., Predavec, M. & Lynam, A. J. (1991). Differential predation of size and sex classes of mice by the barn owl, tyto alba. *Oikos*, *62*(1). https://doi.org/10.2307/3545447

Do, M. T. H. & Yau, K.-W. (2010). Intrinsically photosensitive retinal ganglion cells. *Physiological Reviews*, *90*(4). https://doi.org/10.1152/physrev.00013.2010

Doi, E. & Lewicki, M. S. (2007). A theory of retinal population coding. *Advances in Neural Information Processing Systems*, *19*.

Dräger, U. C. & Olsen, J. F. (1980). Origins of crossed and uncrossed retinal projections in pigmented and albino mice. *Journal of Comparative Neurology*, *191*(3). https://doi.org/10.1002/cne.901910306

Dräger, U. C. & Olsen, J. F. (1981). Ganglion-cell distribution in the retina of the mouse. *Investigative ophthalmology & visual science*, *20*(3).

Eckmann, S., Klimmasch, L., Shi, B. E. & Triesch, J. (2020). Active efficient coding explains the development of binocular vision and its failure in amblyopia. *Proceedings of the National Academy of Sciences*, *117*(11). https://doi.org/10.1073/pnas.1908100117

Eichhorn, J., Sinz, F. & Bethge, M. (2009). Natural image coding in v1: How much use is orientation selectivity? *PLOS computational Biology*, *5*(4). https://doi.org/10.1371/journal.pcbi.1000336

Einhäuser, W., Moeller, G. U., Schumann, F., Conradt, J., Vockeroth, J., Bartl, K., Schneider, E. & König, P. (2009). Eye–head coordination during

free exploration in human and cat. *Annals of the New York Academy of Sciences*, *1164*(1). https://doi.org/10.1111/j.1749-6632.2008.03709.x

Ellis, E. M., Gauvain, G., Sivyer, B. & Murphy, G. J. (2016). Shared and distinct retinal input to the mouse superior colliculus and dorsal lateral geniculate nucleus. *Journal of Neurophysiology*, *116*(2). https://doi.org/10.1152/jn.00227.2016

Erskine, L. & Herrera, E. (2014). Connecting the retina to the brain basic anatomy of the mammalian visual system: From the eye to the cortex. *ASN Neuro*, *6*(6). https://doi.org/10.1177/1759091414562107

Essen, D. V., Olshausen, B. A., Anderson, C. H. & Gallant, J. T. (1991). Pattern recognition, attention, and information bottlenecks in the primate visual system. In B. P. Mathur & C. Koch (Eds.), *Visual information processing: From neurons to chips*. https://doi.org/10.1117/12.45537

Field, D. J. (1987). Relations between the statistics of natural images and the response properties of cortical cells. *Journal of the Optical Society of America*, *4*(12). https://doi.org/10.1364/JOSAA.4.002379

Field, D. J. (1994). What is the goal of sensory coding? *Neural Computation*, *6*(4). https://doi.org/10.1162/neco.1994.6.4.559

Fiser, A., Mahringer, D., Oyibo, H. K., Petersen, A. V., Leinweber, M. & Keller, G. B. (2016). Experience-dependent spatial expectations in mouse visual cortex. *Nature Neuroscience*, *19*(12). https://doi.org/10.1038/nn.4385

Franke, K., Chagas, A. M., Zhao, Z., Zimmermann, M. J., Bartel, P., Qiu, Y., Szatko, K. P., Baden, T. & Euler, T. (2019). An arbitrary-spectrum spatial visual stimulator for vision research. *eLife*, *8*. https://doi.org/10.7554/eLife.48779

Freedman, E. G. (2008). Coordination of the eyes and head during visual orienting. *Experimental Brain Research*, *190*(4). https://doi.org/10.1007/s00221-008-1504-8

Friedburg, C., Allen, C. P., Mason, P. J. & Lamb, T. D. (2004). Contribution of cone photoreceptors and post-receptoral mechanisms to the human photopic electroretinogram. *The Journal of Physiology*, *556*(3). https://doi.org/10.1113/jphysiol.2004.061523

Froudarakis, E., Berens, P., Ecker, A. S., Cotton, R. J., Sinz, F. H., Yatsenko, D., Saggau, P., Bethge, M. & Tolias, A. S. (2014). Population code in mouse v1 facilitates readout of natural scenes through increased sparseness. *Nature Neuroscience*, *17*(6). https://doi.org/10.1038/nn.3707

Fu, Y. & Yau, K. (2007). Phototransduction in mouse rods and cones. *Pflügers Archiv - European Journal of Physiology*, *454*(5). https://doi.org/10.1007/s00424-006-0194-y

Fukushima, K. & Miyake, S. (1982). Neocognitron: A self-organizing neural network model for a mechanism of visual pattern recognition. In S.-i. Amari & M. A. Arbib (Eds.), *Competition and cooperation in neural nets*. Springer Berlin Heidelberg. https://doi.org/10.1007/978-3-642-46466-9_18

Geisler, W. S. (2008). Visual perception and the statistical properties of natural scenes. *Annual Review of Psychology*, *59*. https://doi.org/10.1146/annurev.psych.58.110405.085632

Gerhard, H. E., Wichmann, F. A. & Bethge, M. (2013). How sensitive is the human visual system to the local statistics of natural images? *PLOS Computational Biology*, *9*(1). https://doi.org/10.1371/journal.pcbi.1002873

Girshick, A. R., Landy, M. S. & Simoncelli, E. P. (2011). Cardinal rules: Visual orientation perception reflects knowledge of environmental statistics. *Nature neuroscience*, *14*(7). https://doi.org/10.1038/nn.2831

Gold, J. I. & Shadlen, M. N. (2007). The neural basis of decision making. *Annual Review of Neuroscience*, *30*(1). https://doi.org/10.1146/annurev.neuro.29.051605.113038

Gomez-Marin, A. & Ghazanfar, A. A. (2019). The life of behavior. *Neuron*, *104*(1). https://doi.org/10.1016/j.neuron.2019.09.017

Govardovskii, V., Fyhrquist, N., Reuter, T., Kuzmin, D. & K, D. (2000). In search of the visual pigment template. *Visual Neuroscience*, *17*(4). https://doi.org/10.1017/S0952523800174036

Graf, W. (1947). Mouse populations in relation to predation by foxes and hawks. *The Murrelet*, *28*(2). https://doi.org/10.2307/3534119

Graham, D. J., Chandler, D. M. & Field, D. J. (2006). Can the theory of "whitening" explain the center-surround properties of retinal gan-

glion cell receptive fields? *Vision research*, *46*(18). https://doi.org/10.1016/j.visres.2006.03.008

Hammer, S., Monavarfeshani, A., Lemon, T., Su, J. & Fox, M. A. (2015). Multiple retinal axons converge onto relay cells in the adult mouse thalamus. *Cell Reports*, *12*(10). https://doi.org/10.1016/j.celrep.2015.08.003

Harmening, W. & Wagner, H. (2011). From optics to attention: Visual perception in barn owls. *Journal of Comparative Physiology.*, *197*. https://doi.org/10.1007/s00359-011-0664-3

Hauzman, E., Bonci, D. M. & Ventura, D. F. (2018). Retinal topographic maps: A glimpse into the animals' visual world. In T. Heinbockel (Ed.), *Sensory nervous system*. IntechOpen. https://doi.org/10.5772/intechopen.74645

Hendrickson, A. (2005). Organization of the adult primate fovea. In P. L. Penfold & J. M. Provis (Eds.), *Macular degeneration*. Springer Berlin Heidelberg. https://doi.org/10.1007/3-540-26977-0_1

Holmgren, C. D., Stahr, P., Wallace, D. J., Voit, K.-M., Matheson, E. J., Sawinski, J., Bassetto, G. & Kerr, J. N. (2021). Visual pursuit behavior in mice maintains the pursued prey on the retinal region with least optic flow. *eLife*, *10*. https://doi.org/10.7554/eLife.70838

Hoy, J. L., Bishop, H. I. & Niell, C. M. (2019). Defined cell types in superior colliculus make distinct contributions to prey capture behavior in the mouse. *Current Biology*, *29*(23). https://doi.org/10.1016/j.cub.2019.10.017

Hoy, J. L., Yavorska, I., Wehr, M. & Niell, C. M. (2016). Vision drives accurate approach behavior during prey capture in laboratory mice. *Current Biology*, *26*(22). https://doi.org/10.1016/j.cub.2016.09.009

Hubel, D. H. & Wiesel, T. N. (1959). Receptive fields of single neurones in the cat's striate cortex. *The Journal of physiology*, *148*(3). https://doi.org/10.1113/jphysiol.1959.sp006308

Hubel, D. H. & Wiesel, T. N. (1962). Receptive fields, binocular interaction and functional architecture in the cat's visual cortex. *The Journal of Physiology*, *160*(1). https://doi.org/10.1113/jphysiol.1962.sp006837

Hubel, D. H. & Wiesel, T. N. (1969). Anatomical demonstration of columns in the monkey striate cortex. *Nature*, *221*(5182). https://doi.org/10.1038/221747a0

Hubel, D. H. & Wiesel, T. N. (1974). Uniformity of monkey striate cortex: A parallel relationship between field size, scatter, and magnification factor. *Journal of Comparative Neurology*, *158*(3). https://doi.org/10.1002/cne.901580305

Hut, R., Scheper, A. & Daan, S. (2000). Can the circadian system of a diurnal and a nocturnal rodent entrain to ultraviolet light? *Journal of Comparative Physiology A*, (186). https://doi.org/10.1007/s003590000124

Iwashita, M., Kanai, R., Funabiki, K., Matsuda, K. & Hirano, T. (2001). Dynamic properties, interactions and adaptive modifications of vestibulo-ocular reflex and optokinetic response in mice. *Neuroscience Research*, *39*(3). https://doi.org/10.1016/S0168-0102(00)00228-5

Jensen, S. P., Gray, S. J. & Hurst, J. L. (2003). How does habitat structure affect activity and use of space among house mice? *Animal Behaviour*, *66*(2). https://doi.org/10.1006/anbe.2003.2184

Jeon, C.-J., Strettoi, E. & Masland, R. H. (1998). The major cell populations of the mouse retina. *Journal of Neuroscience*, *18*(21). https://doi.org/10.1523/JNEUROSCI.18-21-08936.1998

Ji, X.-y., Zingg, B., Mesik, L., Xiao, Z., Zhang, L. I. & Tao, H. W. (2015). Thalamocortical Innervation Pattern in Mouse Auditory and Visual Cortex: Laminar and Cell-Type Specificity. *Cerebral Cortex*, *26*(6). https://doi.org/10.1093/cercor/bhv099

Joesch, M. & Meister, M. (2016). A neuronal circuit for colour vision based on rod–cone opponency. *Nature*, *532*. https://doi.org/10.1038/nature17158

Johnson, K. P., Fitzpatrick, M. J., Zhao, L., Wang, B., McCracken, S., Williams, P. R. & Kerschensteiner, D. (2021). Cell-type-specific binocular vision guides predation in mice. *Neuron*, *109*(9). https://doi.org/10.1016/j.neuron.2021.03.010

Kalatsky, V. A. & Stryker, M. P. (2003). New paradigm for optical imaging: Temporally encoded maps of intrinsic signal. *Neuron*, *38*(4). https://doi.org/10.1016/S0896-6273(03)00286-1

Katoh, A., Kitazawa, H., Itohara, S. & Nagao, S. (1998). Dynamic characteristics and adaptability of mouse vestibulo-ocular and optokinetic response eye movements and the role of the flocculo-olivary system revealed by chemical lesions. *Proceedings of the National Academy of Sciences*, *95*(13). https://doi.org/10.1073/pnas.95.13.7705

Kautzky, M., Qiu, Y., Zhao, Z., Euler, T. & Busse, L. (2022). Mice adjust eye position during viewing of naturalistic movies. *In preparation*.

Kautzky, M. & Busse, L. (2020). Vision: How mice control their view. *Current Biology*, *30*(11). https://doi.org/10.1016/j.cub.2020.04.063

Keeler, C. E. (1928). Blind mice. *Journal of Experimental Zoology*, *51*(4). https://doi.org/10.1002/jez.1400510404

Keller, G. B., Bonhoeffer, T. & Hübener, M. (2012). Sensorimotor mismatch signals in primary visual cortex of the behaving mouse. *Neuron*, *74*(5). https://doi.org/10.1016/j.neuron.2012.03.040

Khan, S. & Chang, R. (2013). Anatomy of the vestibular system: A review. *Neuro Rehabilitation*, *32*(3). https://doi.org/10.3233/NRE-130866

Khan, S. I., Della Santina, C. C. & Migliaccio, A. A. (2019). Angular vestibuloocular reflex responses in otop1 mice. i. otolith sensor input is essential for gravity context-specific adaptation. *Journal of Neurophysiology*, *121*(6). https://doi.org/10.1152/jn.00811.2018

Kim, U., Mahroo, O., Mollon, J. & Yu Wai Man, P. (2021). Retinal ganglion cells—diversity of cell types and clinical relevance. *Frontiers in Neurology*, *12*. https://doi.org/10.3389/fneur.2021.661938

Klimmasch, L., Schneider, J., Lelais, A., Shi, B. E. & Triesch, J. (2018). An active efficient coding model of binocular vision development under normal and abnormal rearing conditions. In P. Manoonpong, J. C. Larsen, X. Xiong, J. Hallam & J. Triesch (Eds.), *From animals to animats 15*. Springer International Publishing. https://doi.org/10.1007/978-3-319-97628-0_6

Krakauer, J. W., Ghazanfar, A. A., Gomez-Marin, A., MacIver, M. A. & Poeppel, D. (2017). Neuroscience needs behavior: Correcting a reductionist bias. *Neuron*, *93*(3). https://doi.org/10.1016/j.neuron.2016.12.041

Kramer, M. A. (1991). Nonlinear principal component analysis using autoassociative neural networks. *American Institute of Chemical Engineers journal*, *37*(2). https://doi.org/10.1002/aic.690370209

Kreile, A. K., Bonhoeffer, T. & Hubener, M. (2011). Altered visual experience induces instructive changes of orientation preference in mouse visual cortex. *Journal of Neuroscience*, *31*(39). https://doi.org/10.1523/jneurosci.2143-11.2011

Kremkow, J., Jin, J., Wang, Y. & Alonso, J.-M. (2016). Principles underlying sensory map topography in primary visual cortex. *Nature*, *533*. https://doi.org/10.1038/nature17936

La Chioma, A., Bonhoeffer, T. & Hübener, M. (2019). Area-Specific Mapping of Binocular Disparity across Mouse Visual Cortex. *Current Biology*, *29*(17). https://doi.org/10.1016/j.cub.2019.07.037

Land, M. F. (2015). Eye movements of vertebrates and their relation to eye form and function. *Journal of Comparative Physiology A*, *201*(2). https://doi.org/10.1007/s00359-014-0964-5

Land, M. F. (2019). The evolution of gaze shifting eye movements. In T. Hodgson (Ed.), *Processes of visuospatial attention and working memory*. Springer International Publishing. https://doi.org/10.1007/7854_2018_60

Land, M. F. & Nilsson, D.-E. (2012). *Animal Eyes*. Oxford University Press. https://doi.org/10.1093/acprof:oso/9780199581139.001.0001

Laughlin, S. (1981). A simple coding procedure enhances a neuron's information capacity. *Zeitschrift für Naturforschung C*, *36*(9-10). https://doi.org/10.1515/znc-1981-9-1040

Lee, T.-s. & Potetz, B. (2005). Scaling laws in natural scenes and the inference of 3d shape. In Y. Weiss, B. Schölkopf & J. Platt (Eds.), *Advances in neural information processing systems*. MIT Press.

Li, B., Peterson, M. R. & Freeman, R. D. (2003). Oblique effect: A neural basis in the visual cortex. *Journal of Neurophysiology*, *90*(1). https://doi.org/10.1152/jn.00954.2002

Liberti, W., Perkins, L., Leman, D. & Gardner, T. (2017). An open source, wireless capable miniature microscope system. *Journal of neural engineering*, *14*. https://doi.org/10.1088/1741-2552/aa6806

Lindsey, J., Ocko, S. A., Ganguli, S. & Deny, S. (2019). A unified theory of early visual representations from retina to cortex through anatomically constrained deep cnns. *arXiv preprint*.

Lipp, H.-P. & Wolfer, D. P. (2013). Natural neurobiology and behavior of the mouse: Relevance for behavioral studies in the laboratory. In W. E. Crusio, F. Sluyter, R. T. Gerlai & S. Pietropaolo (Eds.), *Behavioral genetics of the mouse*. Cambridge University Press. https://doi.org/10.1017/CBO9781139541022.003

Lockley, S. W., Brainard, G. C. & Czeisler, C. A. (2003). High sensitivity of the human circadian melatonin rhythm to resetting by short wavelength light. *The Journal of clinical Endocrinology & Metabolism*, *88*(9). https://doi.org/10.1210/jc.2003-030570

Lonini, L., Forestier, S., Teulière, C., Zhao, Y., Shi, B. & Triesch, J. (2013). Robust active binocular vision through intrinsically motivated learning. *Frontiers in Neurorobotics*, *7*. https://doi.org/10.3389/fnbot.2013.00020

Mante, V., Frazor, R. A., Bonin, V., Geisler, W. S. & Carandini, M. (2005). Independence of luminance and contrast in natural scenes and in the early visual system. *Nature Neuroscience*, *8*(12). https://doi.org/10.1038/nn1556

Martersteck, E. M., Hirokawa, K. E., Evarts, M., Bernard, A., Duan, X., Li, Y., Ng, L., Oh, S. W., Ouellette, B., Royall, J. J., Stoecklin, M., Wang, Q., Zeng, H., Sanes, J. R. & Harris, J. A. (2017). Diverse central projection patterns of retinal ganglion cells. *Cell Reports*, *18*(8). https://doi.org/10.1016/j.celrep.2017.01.075

Mazade, R., Jin, J., Pons, C. & Alonso, J.-M. (2019). Functional specialization of on and off cortical pathways for global-slow and local-fast vision. *Cell Reports*, *27*(10). https://doi.org/10.1016/j.celrep.2019.05.007

McCullough, M. H. & Goodhill, G. J. (2021). Unsupervised quantification of naturalistic animal behaviors for gaining insight into the brain. *Current Opinion in Neurobiology*, *70*. https://doi.org/10.1016/j.conb.2021.07.014

Merbs, S. L. & Nathans, J. (1992). Absorption spectra of human cone pigments. *Nature*, *356*(6368). https://doi.org/10.1038/356433a0

Meyer, A. F., O'Keefe, J. & Poort, J. (2020). Two distinct types of eye-head coupling in freely moving mice. *Current Biology*, *30*(11). https://doi.org/10.1016/j.cub.2020.04.042

Meyer, A. F., Poort, J., O'Keefe, J., Sahani, M. & Linden, J. F. (2018). A head-mounted camera system integrates detailed behavioral monitoring with multichannel electrophysiology in freely moving mice. *Neuron*, *100*(1). https://doi.org/10.1016/j.neuron.2018.09.020

Michaiel, A. M., Abe, E. T. & Niell, C. M. (2020). Dynamics of gaze control during prey capture in freely moving mice. *eLife*, *9*. https://doi.org/10.7554/eLife.57458

Migliaccio, A. A., Meierhofer, R. & Della Santina, C. C. (2010). Characterization of the 3d angular vestibulo-ocular reflex in c57bl6 mice. *Experimental Brain Research*, *210*(3-4). https://doi.org/10.1007/s00221-010-2521-y

Mills, S. L., Tian, L.-M., Hoshi, H., Whitaker, C. M. & Massey, S. C. (2014). Three distinct blue-green color pathways in a mammalian retina. *Journal of Neuroscience*, *34*(5). https://doi.org/10.1523/JNEUROSCI.3901-13.2014

Morsli, H., Choo, D., Ryan, A., Johnson, R. & Wu, D. K. (1998). Development of the mouse inner ear and origin of its sensory organs. *Journal of Neuroscience*, *18*(9). https://doi.org/10.1523/JNEUROSCI.18-09-03327.1998

Muzzu, T. & Saleem, A. (2022). Feature selectivity can explain mismatch signals in mouse visual cortex. *Cell Reports*, *38*(1). https://doi.org/10.1016/j.celrep.2022.110413

Nasr, S. & Tootell, R. B. H. (2012). A cardinal orientation bias in scene-selective visual cortex. *Journal of Neuroscience*, *32*(43). https://doi.org/10.1523/JNEUROSCI.2036-12.2012

Nityananda, V. & Read, J. C. A. (2017). Stereopsis in animals: evolution, function and mechanisms. *Journal of Experimental Biology*, *220*(14). https://doi.org/10.1242/jeb.143883

Ocko, S., Lindsey, J., Ganguli, S. & Deny, S. (2018). The emergence of multiple retinal cell types through efficient coding of natural movies. In S. Bengio, H. Wallach, H. Larochelle, K. Grauman, N. Cesa-Bianchi &

R. Garnett (Eds.), *Advances in neural information processing systems*. Curran Associates, Inc. https://doi.org/10.1101/458737

Olcese, U., Iurilli, G. & Medini, P. (2013). Cellular and synaptic architecture of multisensory integration in the mouse neocortex. *Neuron*, *79*(3). https://doi.org/10.1016/j.neuron.2013.06.010

Olshausen, B. A. & Field, D. J. (1996). Emergence of simple-cell receptive field properties by learning a sparse code for natural images. *Nature*, *381*(6583). https://doi.org/10.1038/381607a0

Oommen, B. S. & Stahl, J. S. (2008). Eye orientation during static tilts and its relationship to spontaneous head pitch in the laboratory mouse. *Brain Research*, *1193*. https://doi.org/10.1016/j.brainres.2007.11.053

Paiton, D. M., Frye, C. G., Lundquist, S. Y., Bowen, J. D., Zarcone, R. & Olshausen, B. A. (2020). Selectivity and robustness of sparse coding networks. *Journal of Vision*, *20*(12). https://doi.org/10.1167/jov.20.12.10

Parker, P. R. L., Martins, D. M., Leonard, E. S. P., Casey, N. M., Sharp, S. L., Abe, E. T. T., Smear, M. C., Yates, J. L., Mitchell, J. F. & Niell, C. M. (2022). A dynamic sequence of visual processing initiated by gaze shifts. *preprint on bioRxiv*. https://doi.org/10.1101/2022.08.23.504847

Parker, P. R., Brown, M. A., Smear, M. C. & Niell, C. M. (2020). Movement-related signals in sensory areas: Roles in natural behavior. *Trends in Neurosciences*, *43*(8). https://doi.org/10.1016/j.tins.2020.05.005

Payne, H. L. & Raymond, J. L. (2017). Magnetic eye tracking in mice. *eLife*, *6*. https://doi.org/10.7554/eLife.29222

Peichl, L. (2005). Diversity of mammalian photoreceptor properties: Adaptations to habitat and lifestyle? *The Anatomical Record Part A: Discoveries in Molecular, Cellular, and Evolutionary Biology*, *287A*(1). https://doi.org/10.1002/ar.a.20262

Peli, E. (1990). Contrast in complex images. *Journal of the Optical Society of America A*, *7*(10). https://doi.org/10.1364/josaa.7.002032

Pennesi, M. E., Lyubarsky, A. L. & Pugh, E. N. (1998). Extreme responsiveness of the pupil of the dark-adapted mouse to steady retinal illumination. *Investigative Ophthalmology & Visual Science*, *39*(11).

Perry, V. & Cowey, A. (1984). Retinal ganglion cells that project to the superior colliculus and pretectum in the macaque monkey. *Neuroscience*, *12*(4). https://doi.org/10.1016/0306-4522(84)90007-1

Pettigrew, J. D., Sanderson, K. J. & Levick, W. R. (1986). Evolution of binocular vision. *Visual neuroscience*. CUP Archive.

Phifer-Rixey, M. & Nachman, M. W. (2015). The natural history of model organisms: Insights into mammalian biology from the wild house mouse *Mus musculus*. *eLife*, *4*. https://doi.org/10.7554/eLife.05959

Piscopo, D. M., El-Danaf, R. N., Huberman, A. D. & Niell, C. M. (2013). Diverse visual features encoded in mouse lateral geniculate nucleus. *Journal of Neuroscience*, *33*(11). https://doi.org/10.1523/JNEUROSCI.5187-12.2013

Prusky, G. T. & Douglas, R. M. (2003). Developmental plasticity of mouse visual acuity. *European Journal of Neuroscience*, *17*(1). https://doi.org/10.1046/j.1460-9568.2003.02420.x

Qiu, Y., Klindt, D. A., Szatko, K. P., Gonschorek, D., Hoefling, L., Schubert, T., Busse, L., Bethge, M. & Euler, T. (2022). Efficient coding of natural scenes improves neural system identification. *preprint on bioRxiv*. https://doi.org/10.1101/2022.01.10.475663

Qiu, Y., Zhao, Z., Klindt, D., Kautzky, M., Szatko, K. P., Schaeffel, F., Rifai, K., Franke, K., Busse, L. & Euler, T. (2021). Natural environment statistics in the upper and lower visual field are reflected in mouse retinal specializations. *Current Biology*. https://doi.org/10.1016/j.cub.2021.05.017

Ratliff, C. P., Borghuis, B. G., Kao, Y.-H., Sterling, P. & Balasubramanian, V. (2010). Retina is structured to process an excess of darkness in natural scenes. *Proceedings of the National Academy of Sciences*, *107*(40). https://doi.org/10.1073/pnas.1005846107

Ripperger, J. A., Jud, C. & Albrecht, U. (2011). The daily rhythm of mice. *FEBS Letters*, *585*(10). https://doi.org/10.1016/j.febslet.2011.02.027

Rompani, S. B., Müllner, F. E., Wanner, A., Zhang, C., Roth, C. N., Yonehara, K. & Roska, B. (2017). Different modes of visual integration in the lateral geniculate nucleus revealed by single-cell-initiated transsynaptic tracing. *Neuron*, *93*(4). https://doi.org/0.1016/j.neuron.2017.01.028

Roucoux, A. & Crommelinck, M. (1976). Eye movements evoked by superior colliculus stimulation in the alert cat. *Brain Research*, *106*(2). https://doi.org/10.1016/0006-8993(76)91030-1

Roy, S., Jun, N. Y., Davis, E. L., Pearson, J. & Field, G. D. (2021). Intermosaic coordination of retinal receptive fields. *Nature*, *592*(7854). https://doi.org/10.1038/s41586-021-03317-5

Ruderman, D. L. & Bialek, W. (1994). Statistics of natural images: Scaling in the woods. *Physical Review Letters*, *73*. https://doi.org/10.1103/PhysRevLett.73.814

Rutz, C. & Troscianko, J. (2013). Programmable, miniature video-loggers for deployment on wild birds and other wildlife. *Methods in Ecology and Evolution*, *4*(2). https://doi.org/10.1111/2041-210x.12003

Sabbah, S., Gemmer, J., Bhatia-Lin, A., Manof, G., Gabriel, C., Siegel, J., Jeffery, N. & Berson, D. (2017). A retinal code for motion along the gravitational and body axes. *Nature*, *546*. https://doi.org/10.1038/nature22818

Sakatani, T. & Isa, T. (2004). Pc-based high-speed video-oculography for measuring rapid eye movements in mice. *Neuroscience Research*, *49*(1). https://doi.org/10.1016/j.neures.2004.02.002

Sakatani, T. & Isa, T. (2007). Quantitative analysis of spontaneous saccade-like rapid eye movements in C57BL/6 mice. *Neuroscience Research*, *58*(3). https://doi.org/10.1016/j.neures.2007.04.003

Samonds, J. M., Choi, V. & Priebe, N. J. (2019). Mice Discriminate Stereoscopic Surfaces Without Fixating in Depth. *Journal of Neuroscience*, *39*(41). https://doi.org/10.1523/JNEUROSCI.0895-19.2019

Samonds, J. M., Geisler, W. S. & Priebe, N. J. (2018). Natural image and receptive field statistics predict saccade sizes. *Nature Neuroscience*, *21*. https://doi.org/10.1038/s41593-018-0255-5

Samonds, J. M., Potetz, B. R. & Lee, T. S. (2012). Relative luminance and binocular disparity preferences are correlated in macaque primary visual cortex, matching natural scene statistics. *Proceedings of the National Academy of Sciences*, *109*(16). https://doi.org/10.1073/pnas.1200125109

Sanes, J. R. & Masland, R. H. (2015). The types of retinal ganglion cells: Current status and implications for neuronal classification. *Annual Review of Neuroscience*, *38*(1). https://doi.org/10.1146/annurev-neuro-071714-034120

Sattler, N. J. & Wehr, M. (2021). A head-mounted multi-camera system for electrophysiology and behavior in freely-moving mice. *Frontiers in Neuroscience*, *14*. https://doi.org/10.3389/fnins.2020.592417

Scholl, B., Burge, J. & Priebe, N. J. (2013). Binocular integration and disparity selectivity in mouse primary visual cortex. *Journal of Neurophysiology*, *109*(12). https://doi.org/10.1152/jn.01021.2012

Seabrook, T. A., Burbridge, T. J., Crair, M. C. & Huberman, A. D. (2017). Architecture, Function, and Assembly of the Mouse Visual System. *Annual Review of Neuroscience*, *40*(1). https://doi.org/10.1146/annurev-neuro-071714-033842

Shapcott, K. A., Weigand, M., Glukhova, I., Havenith, M. N. & Schölvinck, M. L. (2022). Domevr: A setup for experimental control of an immersive dome virtual environment created with unreal engine 4. *preprint on bioRxiv*. https://doi.org/10.1101/2022.04.04.486889

Shen, G., Tao, X., Zhang, B., Smith, E. L. & Chino, Y. M. (2014). Oblique effect in visual area 2 of macaque monkeys. *Journal of Vision*, *14*(2). https://doi.org/10.1167/14.2.3

Shi, R., Ji, J., Zhang, C. & Miao, Q. (2019). Boosting sparsity-induced autoencoder: A novel sparse feature ensemble learning for image classification. *International Journal of Advanced Robotic Systems*, *16*(3). https://doi.org/10.1177/1729881419853471

Sibille, J., Gehr, C., Teh, K. L. & Kremkow, J. (2022). Tangential high-density electrode insertions allow to simultaneously measure neuronal activity across an extended region of the visual field in mouse superior colliculus. *Journal of Neuroscience Methods*, *376*. https://doi.org/10.1016/j.jneumeth.2022.109622

Simoncelli, E. P. & Olshausen, B. A. (2001). Natural image statistics and neural representation. *Annual review of neuroscience*, *24*(1). https://doi.org/10.1146/annurev.neuro.24.1.1193

Sit, K. K. & Goard, M. J. (2020). Distributed and retinotopically asymmetric processing of coherent motion in mouse visual cortex. *Nature Communications*, *11*(1). https://doi.org/10.1038/s41467-020-17283-5

Speed, A., Del Rosario, J., Burgess, C. P. & Haider, B. (2019). Cortical State Fluctuations across Layers of V1 during Visual Spatial Perception. *Cell Reports*, *26*(11). https://doi.org/10.1016/j.celrep.2019.02.045

Stabio, M. E., Sondereker, K. B., Haghgou, S. D., Day, B. L., Chidsey, B., Sabbah, S. & Renna, J. M. (2018). A novel map of the mouse eye for orienting retinal topography in anatomical space. *The Journal of Comparative Neurology*, *526*(11). https://doi.org/10.1002/cne.24446

Stenkamp, D. L. (2015). Chapter twenty-three - development of the vertebrate eye and retina. In J. F. Hejtmancik & J. M. Nickerson (Eds.), *Molecular biology of eye disease*. Academic Press. https://doi.org/10.1016/bs.pmbts.2015.06.006

Sterratt, D. C., Lyngholm, D., Willshaw, D. J. & Thompson, I. D. (2013). Standard anatomical and visual space for the mouse retina: Computational reconstruction and transformation of flattened retinae with the retistruct package. *Public Library of Science Computational Biology*, *9*(2). https://doi.org/10.1371/journal.pcbi.1002921

Stowers, J., Hofbauer, M., Bastien, R., Griessner, J., Higgins, P., Farooqui, S., Fischer, R., Nowikovsky, K., Haubensak, W., Couzin, I., Tessmar-Raible, K. & Straw, A. (2017). Virtual reality for freely moving animals. *Nature Methods*, *14*. https://doi.org/10.1038/nmeth.4399

Stroud, A. C., LeDue, E. E. & Crowder, N. A. (2012). Orientation specificity of contrast adaptation in mouse primary visual cortex [PMID: 22696541]. *Journal of Neurophysiology*, *108*(5). https://doi.org/10.1152/jn.01148.2011

Switkes, E., Mayer, M. J. & Sloan, J. A. (1978). Spatial frequency analysis of the visual environment: Anisotropy and the carpentered environment hypothesis. *Vision Research*, *18*(10). https://doi.org/10.1016/0042-6989(78)90232-8

Szatko, K. P., Korympidou, M. M., Ran, Y., Berens, P., Dalkara, D., Schubert, T., Euler, T. & Franke, K. (2020). Neural circuits in the mouse retina support color vision in the upper visual field. *Nature Communications*, *11*(1). https://doi.org/10.1038/s41467-020-17113-8

Teulière, C., Forestier, S., Lonini, L., Zhang, C., Zhao, Y., Shi, B. & Triesch, J. (2015). Self-calibrating smooth pursuit through active efficient coding. *Robotics and Autonomous Systems*, *71*. https://doi.org/10.1016/j.robot.2014.11.006

Tolhurst, D., Tadmor, Y. & Chao, T. (1992). Amplitude spectra of natural images. *Ophthalmic and Physiological Optics*, *12*(2). https://doi.org/10.1111/j.1475-1313.1992.tb00296.x

Turner, P. V. (2014). Chapter 12 - rodent and rabbit welfare in the research environment. In K. Bayne & P. V. Turner (Eds.), *Laboratory animal welfare*. Academic Press. https://doi.org/10.1016/B978-0-12-385103-1.00012-9

van Alphen, A., Stahl, J. & De Zeeuw, C. (2001). The dynamic characteristics of the mouse horizontal vestibulo-ocular and optokinetic response. *Brain Research*, *890*(2). https://doi.org/10.1016/S0006-8993(00)03180-2

van Beest, E., Mukherjee, S., Kirchberger, L., Schnabel, U., Van der Togt, C., Teeuwen, R., Barsegyan, A., Meyer, A., Poort, J., Roelfsema, P. & Self, M. (2021). Mouse visual cortex contains a region of enhanced spatial resolution. *Nature Communications*, *12*. https://doi.org/10.1038/s41467-021-24311-5

van Rossum, M. C., O'Brien, B. J. & Smith, R. G. (2003). Effects of noise on the spike timing precision of retinal ganglion cells. *Journal of Neurophysiology*, *89*(5). https://doi.org/10.1152/jn.01106.2002

Veilleux, C. & Kirk, E. (2014). Visual acuity in mammals: Effects of eye size and ecology. *Brain, Behavior and Evolution*, *83*(1). https://doi.org/10.1159/000357830

Vincent, B. T. & Baddeley, R. J. (2003). Synaptic energy efficiency in retinal processing. *Vision Research*, *43*(11). https://doi.org/10.1016/S0042-6989(03)00096-8

Wallace, D. J., Greenberg, D. S., Sawinski, J., Rulla, S., Notaro, G. & Kerr, J. N. (2013). Rats maintain an overhead binocular field at the expense of constant fusion. *Nature*, *498*(7452). https://doi.org/10.1038/nature12153

Walls, G. (1962). The evolutionary history of eye movements. *Vision Research*, *2*(1). https://doi.org/10.1016/0042-6989(62)90064-0

Wilkes, T., McGonigle, A., Pering, T., Taggart, A., White, B., Bryant, R. & Willmott, J. (2016). Ultraviolet imaging with low cost smartphone sensors: Development and application of a raspberry pi-based uv camera. *Sensors*, *16*(10). https://doi.org/10.3390/s16101649

Yacoub, E., Harel, N. & Uğurbil, K. (2008). High-field fMRI unveils orientation columns in humans. *Proceedings of the National Academy of Sciences of the United States of America*, *105*(30). https://doi.org/10.1073/pnas.0804110105

Yilmaz, M. & Meister, M. (2013). Rapid innate defensive responses of mice to looming visual stimuli. *Current Biology*, *23*(20). https://doi.org/10.1016/j.cub.2013.08.015.Rapid

Yonehara, K., Ishikane, H., Sakuta, H., Shintani, T., Nakamura-Yonehara, K., Kamiji, N. L., Usui, S. & Noda, M. (2009). Identification of retinal ganglion cells and their projections involved in central transmission of information about upward and downward image motion. *Public Library of Science one*, *4*(1). https://doi.org/10.1371/journal.pone.0004320

Zahler, S. H., Taylor, D. E., Wong, J. Y., Adams, J. M. & Feinberg, E. H. (2021). Superior colliculus drives stimulus-evoked directionally biased saccades and attempted head movements in head-fixed mice. *eLife*, *10*. https://doi.org/10.7554/eLife.73081

Zaidi, F. H., Hull, J. T., Peirson, S. N., Wulff, K., Aeschbach, D., Gooley, J. J., Brainard, G. C., Gregory-Evans, K., Rizzo III, J. F., Czeisler, C. A. et al. (2007). Short-wavelength light sensitivity of circadian, pupillary, and visual awareness in humans lacking an outer retina. *Current Biology*, *17*(24). https://doi.org/10.1016/j.cub.2007.11.034

Zhang, C., Triesch, J. & Shi, B. E. (2016). An active-efficient-coding model of optokinetic nystagmus. *Journal of Vision*, *16*(14). https://doi.org/10.1167/16.14.10

Zhao, Y., Rothkopf, C. A., Triesch, J. & Shi, B. E. (2012). A unified model of the joint development of disparity selectivity and vergence control. *2012 IEEE International Conference on Development and Learning and*

Epigenetic Robotics (ICDL). https://doi.org/10.1109/DevLrn.2012.6400876

Zhaoping, L. (2006). Theoretical understanding of the early visual processes by data compression and data selection. *Network: Computation in Neural Systems*, *17*(4). https://doi.org/10.1080/09548980600931995

Zhu, Q., Zhang, C., Triesch, J. & Shi, B. E. (2022). Learning torsional eye movements through active efficient coding. *Neuromorphic Computing and Engineering*, *2*(3). https://doi.org/10.1088/2634-4386/ac84fd

Zylberberg, J. & DeWeese, M. R. (2013). Sparse coding models can exhibit decreasing sparseness while learning sparse codes for natural images. *Public Library of Science Computational Biology*, *9*(8). https://doi.org/10.1371/journal.pcbi.1003182

ACKNOWLEDGEMENTS

First and foremost, I would like to thank my supervisors Prof. Dr. Laura Busse and Prof. Dr. Thomas Euler for hosting me in the lab and for providing me with wide ranging scientific and technical guidance, support, and instructions throughout my PhD.
I am extremely grateful to Yongrong Qiu, who, as my partner student on this project, supported me with highly valuable discussions or also hands-on at the setup.
The atmosphere in the Busse lab was very enjoyable and productive and I want to thank all members for their support over the years, many inspiring coffee break discussions and invaluable time spent together in and outside the lab. In particular, I am deeply grateful to Shreya Khanal, Melanie Sotgia and Ann Kotkat, who made this experience so much fun and precious with their help, moral support and friendship.
Also, I want to thank my thesis advisory committee, Prof. Dr. Thomas Wachtler and Prof. Dr. Mark Hübener, who were very helpful in discussing my work, problems and future direction of my project.
I would like to give special thanks to the Graduate School of Systemic Neurosciences for providing a fruitful academic framework. Financially, I was kindly supported by the Sonderforschungsbereich "Robustheit des Sehens – Prinzipien der Inferenz und der neuronalen Mechanismen" (SFB 1233).
Finally, I want to express my deep gratitude to my family and friends, for their belief in me and encouragement, that has kept my spirits and motivation high during this process.
Thank you!

PUBLICATION LIST

Kautzky, M.[1] and Busse, L. (2020) Vision: How Mice Control Their View. *Current Biology* 30, R635–R662, https://doi.org/10.1016/j.cub.2020.04.063.

Qiu, Y., Zhao, Z., Klindt, D., **Kautzky, M.**[1], Szatko, KP., Schaeffel, F., Rifai, K., Franke, K., Busse, L., Euler, T. (2021) Natural environment statistics in the upper and lower visual field are reflected in mouse retinal specializations. *Current Biology* 9; 31(15):3233-3247.e6, 10.1016/j.cub.2021.05.017.

Kautzky, M.*[1], Qiu, Y.*, Zhao, Z., Euler, T., Busse, L. (2022) Mice adjust eye position during viewing of naturalistic movies. *in preparation*
*shared first authorship between M.K. and Y.Q.

[1] affiliated to Graduate School of Systemic Neuroscience (GSN), LMU Munich, 82151 Planegg-Martinsried, Germany

AUTHOR CONTRIBUTIONS

The contributions of the authors to the studies conducted during my PhD are as follows:

1. **Publication 1:**
   Kautzky, M. and Busse, L. (2020) Vision: How Mice Control Their View. *Current Biology* 30, R635–R662, https://doi.org/10.1016/j.cub.2020.04.063.:

   Writing - Original Draft: Laura Busse, Magdalena Kautzky; **Writing - Review and Editing**: Laura Busse, Magdalena Kautzky;

   My contribution:
   I wrote the original draft of the dispatch, and contributed to the review and preparation of the published version. I also conceptualized the illustration and contributed to its implementation.

2. **Publication 2:**
   Qiu, Y., Zhao, Z., Klindt, D., **Kautzky, M.**, Szatko, KP., Schaeffel, F., Rifai, K., Franke, K., Busse, L., Euler, T. (2021) Natural environment statistics in the upper and lower visual field are reflected in mouse retinal specializations. *Current Biology* 9; 31(15):3233-3247.e6, 10.1016/j.cub.2021.05.017.:

   Conceptualization of ideas: Frank Schäffel, Katharina Rifai, Laura Busse and Thomas Euler;
   Methodology: Yongrong Qiu, Zhijian Zhao, Laura Busse and Thomas Euler, with input from David Klindt and Magdalena Kautzky;
   Formal analysis: Yongrong Qiu, with input from David Klindt, Laura Busse, and Thomas Euler;
   Investigation: Yongrong Qiu, Zhijian Zhao, and Klaudia P Szatko, with input from Katrin Franke, Laura Busse, and Thomas Euler;

Writing – original draft: Yongrong Qiu, Laura Busse, and Thomas Euler;
Writing – review and editing and preparation: Yongrong Qiu, Zhijian Zhao, David Klindt, Klaudia P Szatko, Magdalena Kautzky, Katrin Franke, Laura Busse, and Thomas Euler;
Visualization: Yongrong Qiu and Thomas Euler;
Supervision: Laura Busse and Thomas Euler;
Funding acquisition: Laura Busse, Frank Schaeffel, Katharina Rifai, Katrin Franke, and Thomas Euler

My contribution:
I contributed with suggestions and discussions to the design of the hand-held camera and the analysis of recorded movies. Together with the other authors, I reviewed and edited the manuscript, both for the initial submission and the revision.

3. **Manuscript:**
Kautzky, M.*, Qiu, Y.*, Zhao, Z., Euler, T., Busse, L. (2022) Mice adjust eye position during viewing of naturalistic movies. *in preparation*
*shared first authorship between M.K. and Y.Q.

Conceptualization: Laura Busse, Thomas Euler;
Methodology: Laura Busse, Thomas Euler, Magdalena Kautzky, Yongrong Qiu, Zhijian Zhao;
Software: Magdalena Kautzky, Yongrong Qiu;
Formal Analysis: Yongrong Qiu;
Investigation: Magdalena Kautzky;
Resources: Laura Busse, Thomas Euler;
Data Curation: Laura Busse, Magdalena Kautzky, Yongrong Qiu;
Writing - Original Draft: Laura Busse, Magdalena Kautzky;
Writing - Review and Editing: all authors;
Visualization: Magdalena Kautzky, Yongrong Qiu;
Supervision: Laura Busse, Thomas Euler;
Project Administration: Laura Busse, Thomas Euler;
Funding Acquisition: Laura Busse, Thomas Euler

My contribution:
I developed the method for calibration of the dome setup, designed and built the device to hold the laser pointer and carried out the calibration. I also built the head-mounted camera system, did the implantation surgery and conducted all experiments. I designed the experiments with input from the rest of the team and implemented the visual stimuli. Eye movement movies were preprocessed by me by fitting pupil position with DLC and I developed the code for the analysis of eye movements for Figures 2 and 4 and contributed to code for further analysis. I created Figures 1-4 and provided input to figures 5, 6, 7. Lastly, I wrote the original draft of the manuscript together with Laura Busse, and performed the first sets of revisions and edits, before the other authors also joined the editing process.

We assert that aforementioned author contributions are correct and accurate:

Dr. Yongrong Qiu	Prof. Dr. Laura Busse	Magdalena Kautzky
Place, date	Place, date	Place, date